



# ALMA Fragmented Source Catalog in Orion (FraSCO). I. Outflow Interaction within an Embedded Cluster in OMC-2/FIR 3, FIR 4, and FIR 5

Asako Sato<sup>1</sup> , Satoko Takahashi<sup>2,3</sup> , Shun Ishii<sup>2,3</sup> , Paul T. P. Ho<sup>4,5</sup> , Masahiro N. Machida<sup>6</sup> , John Carpenter<sup>7</sup> ,  
Luis A. Zapata<sup>8</sup> , Paula Stella Teixeira<sup>9</sup> , and Sümeyye Suri<sup>10</sup>

<sup>1</sup> Department of Earth and Planetary Sciences, Graduate School of Science, Kyushu University, Fukuoka 819-0395, Japan; [sato.asako.322@s.kyushu-u.ac.jp](mailto:sato.asako.322@s.kyushu-u.ac.jp)

<sup>2</sup> National Astronomical Observatory of Japan, 2-21-1 Osawa, Mitaka, Tokyo 181-8588, Japan

<sup>3</sup> Department of Astronomical Science, School of Physical Sciences, The Graduate University for Advanced Studies (SOKENDAI), 2-21-1 Osawa, Mitaka, Tokyo 181-8588, Japan

<sup>4</sup> Academia Sinica Institute of Astronomy and Astrophysics, 11F of AS/NTU Astronomy-Mathematics Building, No.1, Section 4, Roosevelt Road, Taipei 10617, Taiwan, R.O.C.

<sup>5</sup> East Asian Observatory, Hilo, HI 96720, USA

<sup>6</sup> Department of Earth and Planetary Sciences, Faculty of Science, Kyushu University, Fukuoka 819-0395, Japan

<sup>7</sup> Joint ALMA Observatory, Alonso de Córdova 3107, Vitacura, Santiago 763-0355, Chile

<sup>8</sup> Instituto de Radioastronomía y Astrofísica, Universidad Nacional Autónoma de México, Antigua Carretera a Pátzcuaro #8701, Ex-Hda. San José de la Huerta, Morelia, Michoacán, C.P. 58089, México

<sup>9</sup> SUPA, School of Physics & Astronomy, University of St Andrews, North Haugh, St Andrews KY16 9SS, UK

<sup>10</sup> University of Vienna, Department of Astrophysics, Türkenschanzstrasse 17, A-1180 Vienna, Austria

Received 2022 August 18; revised 2022 November 21; accepted 2022 November 21; published 2023 February 14

## Abstract

We present a high-angular resolution ( $\sim 1''$ ) and wide-field ( $2.9 \times 1.9$ ) image of the 1.3 mm continuum, CO( $J = 2-1$ ) and SiO( $J = 5-4$ ) line emissions toward an embedded protocluster, FIR 3, FIR 4, and FIR 5, in the Orion Molecular Cloud 2 obtained from the Atacama Large Millimeter/submillimeter Array. We identify 51 continuum sources, 36 of which are newly identified in this study. Their dust masses, projected sizes, and H<sub>2</sub> gas number densities are estimated to be  $3.8 \times 10^{-5}$ – $1.1 \times 10^{-2} M_{\odot}$ , 290–2000 au, and  $6.4 \times 10^6$ – $3.3 \times 10^8 \text{ cm}^{-3}$ , respectively. The results of a Jeans analysis show that  $\sim 80\%$  of the protostellar sources and  $\sim 15\%$  of the prestellar sources are gravitationally bound. We identify 12 molecular outflows traced in the CO( $J = 2-1$ ) emission, six of which are newly detected. We spatially resolve shocked gas structures traced by the SiO( $J = 5-4$ ) emission in this region for the first time. We identify shocked gas originating from outflows and other shocked regions. These results provide direct evidence of an interaction between dust condensation, FIR 4, and an energetic outflow driven by HOPS-370 located within FIR 3. A comparison of the outflow dynamical timescales, fragmentation timescales, and protostellar ages shows that the previously proposed triggered star formation scenario in FIR 4 is not strongly supported. We also discuss the spatial distribution of filaments identified in our continuum image by comparing it with a previously identified hub-fiber system in the N<sub>2</sub>H<sup>+</sup> line.

*Unified Astronomy Thesaurus concepts:* [Protoclusters \(1297\)](#); [Protostars \(1302\)](#); [Giant molecular clouds \(653\)](#); [Millimeter astronomy \(1061\)](#)

*Supporting material:* animations, figure sets, machine-readable table

## 1. Introduction

Most stars are formed within cluster environments (Lada & Lada 2003), and thus, to understand the formation of stars, it is vital to study young protoclusters. Protoclusters are formed within filamentary molecular clouds extending to parsec scale sizes (Schneider & Elmegreen 1979; Evans 1999; Motte et al. 2010; André et al. 2014). Recent observational studies suggest that filamentary molecular clouds have rather complex structures such as hub-filament systems where the filaments intersect around the hub (Myers 2009). In a hub-filament system, a mass accumulation process (i.e., gas inflow) through the filaments onto the hub plays an essential role in determining the final mass of stars within the protocluster (McLaughlin & Pudritz 1996; Bonnell et al. 2001; McKee & Tan 2003; Wang et al. 2010; Smith et al. 2011; Krumholz et al. 2012; Ohashi et al. 2016; Cheng et al. 2018; Sanhueza et al. 2019).

Filamentary molecular clouds are also resolved into fibers defined as velocity-coherent structures by Hacar et al. (2013). These fibers also exhibit complex structures such as hub-fiber systems, and dense cores and clumps seem to form at the hub (e.g., Clarke et al. 2020; Zhang et al. 2020). In this paper, we use the term *filaments* based on the filamentary morphological structures, while we use the term *fibers* when the filamentary structures show velocity coherence. The feedback within protoclusters, such as through outflows and stellar radiation, is another important factor in the star-forming cluster environment (Wang et al. 2010; Nakamura & Li 2011; Hansen et al. 2012; Offner & Chaban 2017). To understand the star formation processes within a protocluster, it is important to observe nearby embedded clusters (within 1 kpc), identify individual sources and associated outflows, and reveal how each source interacts within the protocluster.

The closest known giant molecular cloud is the integral-shaped filament (ISF; Bally et al. 1987) located within the northern part of the Orion A giant molecular cloud (at a distance  $d = 400$  pc; Großschedl et al. 2018) (Maddalena & Thaddeus 1985; Bally et al. 1987; Tatematsu et al. 1993;

Sakamoto et al. 1994; Nagahama et al. 1998; Wilson et al. 2005; Ikeda et al. 2007; O’Dell et al. 2008; Buckle et al. 2012; Kong et al. 2018; Ishii et al. 2019). The ISF extends  $\sim 7$  pc in length and consists of remarkable filamentary molecular clouds hosting hundreds of protostars (Chini et al. 1997; Lis et al. 1998; Johnstone & Bally 1999; Nielbock et al. 2003; Nutter & Ward-Thompson 2007; Takahashi et al. 2013; Sadavoy et al. 2016; Teixeira et al. 2016). Due to its proximity, the ISF is a well-studied region across a wide range of wavelengths (Bally et al. 1987; Chini et al. 1997; Lis et al. 1998; Johnstone & Bally 1999; Megeath et al. 2012; Stutz et al. 2013).

The Orion Molecular Cloud 2 region (the OMC-2 region) is located within the ISF and is classified as an embedded protocluster containing a large number of infrared sources ( $\sim 400$  pc $^{-2}$ ; Lada & Lada 2003). A dozen bright millimeter sources were identified in the OMC-2 region by 1.3 mm single-dish observations (Chini et al. 1997). In this study, we focus on the brightest regions identified by the 1.3 mm single-dish observations, named FIR 3, FIR 4, and FIR 5. Fifteen individual sources have been identified within FIR 3, FIR 4, and FIR 5 by multiwavelength higher angular resolution observations, consisting of one Class 0, three Class I, three Class II, three flat spectra, and five nonclassified millimeter/submillimeter sources (Reipurth et al. 1999; Nielbock et al. 2003; Allen et al. 2007; Megeath et al. 2012; Stutz et al. 2013; Furlan et al. 2016; Osorio et al. 2017; van Terwisga et al. 2019). FIR 4 has the largest luminosity of  $L_{\text{bol}} \sim 1000 L_{\odot}$  in total (Crimier et al. 2009) among FIR 3, FIR 4, and FIR 5. FIR 4 was identified as a single-peak source first from the 1.3 mm continuum observations (Chini et al. 1997), then the interferometric observations spatially resolved the internal structure consisting of several millimeter sources (Shimajiri et al. 2008). Furlan et al. (2016) reported that two protostellar candidates, HOPS-108 (Class 0) and HOPS-64 (Class I), are associated with FIR 4. Due to the large luminosity and complexity of the structure, the origin of the star formation environment in FIR 4 has been discussed in previous studies. Shimajiri et al. (2008) proposed that an energetic outflow driven by HOPS-370, which is a Class I protostellar source located at the peak position of FIR 3 (Furlan et al. 2016; Tobin et al. 2020), has collided with the dust condensation, FIR 4. HOPS-370 has a bolometric luminosity of  $360 L_{\odot}$ , a stellar mass of  $2.5 M_{\odot}$ , and a disk radius of 94 au (Furlan et al. 2016; Tobin et al. 2020). The energetic outflow has been observed at various wavelengths (Yu et al. 1997; Aso et al. 2000; Stanke et al. 2002; Williams et al. 2003; Shimajiri et al. 2008; Takahashi et al. 2008; Stutz et al. 2013; González-García et al. 2016; Osorio et al. 2017; Nakamura et al. 2019; Tanabe et al. 2019; Feddersen et al. 2020; Tobin et al. 2020). Shimajiri et al. (2008) suggested that the outflow interaction has impacted the star formation process within FIR 4. Osorio et al. (2017) and Nakamura et al. (2019) also supported the outflow interaction scenario with their independent observing data sets. On the other hand, López-Sepulcre et al. (2013) suggested the presence of a B-type star within FIR 4 in order to explain the large bolometric luminosity. In contrast, Fontani et al. (2017) and Favre et al. (2018) proposed another scenario using foreground radiation to explain the large bolometric luminosity. It is crucial to obtain high-angular resolution and wide-field imaging to disentangle the proposed scenarios. In addition, other groups have suggested the presence of strong UV radiation, possibly emitted from the interior of FIR 4

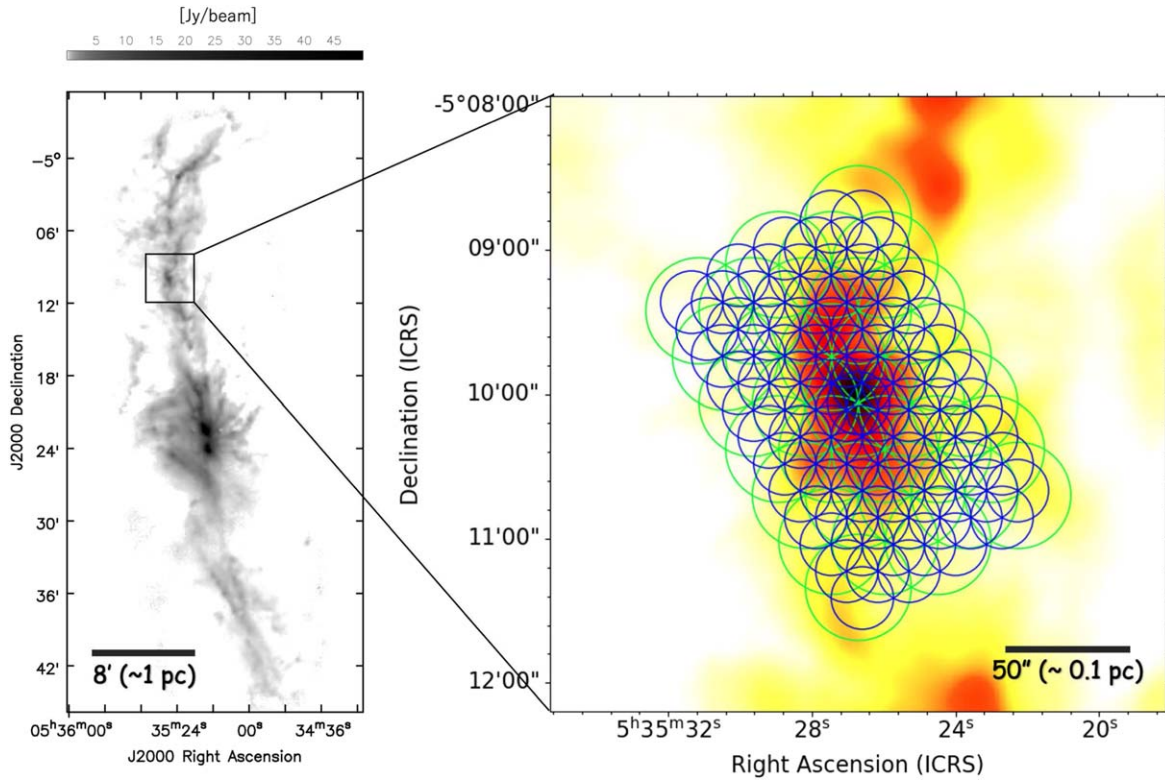
(López-Sepulcre et al. 2013) or radiated by the foreground region (Fontani et al. 2017; Favre et al. 2018). This radiation may be important for explaining the origin and environment of FIR 4.

We report Atacama Large Millimeter/submillimeter Array (ALMA) 12 m array and ACA 7 m array observations toward FIR 3, 4, and 5 within the OMC-2 region. In this paper, we define FIR 3, FIR 4, and FIR 5 as the FIR 3 region, FIR 4 region, and FIR 5 region, respectively, as we discuss substructures spatially resolved both within and around the sources. Our primary goals are to identify protocluster members and to study their physical properties. We observed the 1.3 mm continuum emission and CO( $J = 2-1$ ) emission to identify dust sources and molecular outflows, respectively. We simultaneously observed SiO( $J = 5-4$ ) emission tracing gas originating from outflows and other shocked regions.

We describe the observations, data reduction, and imaging methods in Section 2. In Section 3, we present synthesized images of the 1.3 mm continuum, CO( $J = 2-1$ ), and SiO( $J = 5-4$ ) emissions to identify individual fragmented sources, molecular outflows, and shocked regions, respectively. In Section 4, we discuss the possibility of outflow interactions within the protocluster and how this possibly affects star formation within the embedded protocluster. Based on the continuum data, we also discuss a hub-filament system whose center is located within the FIR 4 region. Finally, we summarize this study in Section 5.

## 2. Observations

ALMA observations of the 1.3 mm continuum, CO( $J = 2-1$ ; 230.53797 GHz) emission, and SiO( $J = 5-4$ ; 217.10498 GHz) emission were carried out with the ALMA 12 m array on 2018 April 19 and with the ACA 7 m array (Morita array) on 2018 April 19, 20, and 23 (project code: 2017.1.01353.S; PI: S. Takahashi). In order to cover the OMC-2/FIR 3, 4, and 5 regions, we mapped a  $3'.08 \times 2'.23$  area (32 fields) with the ACA 7 m array and a  $2'.92 \times 1'.92$  (92 fields) area with the 12 m array with Nyquist sampling (see Figure 1). The field center of the map was set to R.A. =  $05^{\text{h}}35^{\text{m}}26^{\text{s}}.7140$ , decl. =  $-05^{\circ}10'03''.800$ . The on-source times per field of the ACA 7 m array and 12 m array were 540 and 40 s, respectively. A 937.5 MHz wide dual polarization spectral window (244.14 kHz resolution), centered at the frequency of the CO( $J = 2-1$ ) and SiO( $J = 5-4$ ) lines, was placed in two of the four basebands. The velocity resolution in these windows is  $0.32$  km s $^{-1}$  for CO( $J = 2-1$ ) and  $0.34$  km s $^{-1}$  for SiO( $J = 5-4$ ). The other two basebands (two spectral windows), 1875 MHz wide, were allocated to the continuum observations. In addition to the two basebands allocated for the continuum emission, the channels that detected no molecular line emissions from the basebands allocated for CO and SiO were used to produce the continuum image. After subtracting the line emissions, the line-free emission channels provided a total effective continuum bandwidth of 3.4 GHz for the data sets of both arrays. The data sets cover the projected baseline ranges between 7 and 47 m for the ACA 7 m array and between 12 and 423 m for the ALMA 12 m array, and are hence insensitive to structures extending to more than  $23''.0$  for the ACA 7 m array and  $13''.4$  for the ALMA 12 m array at the 10% level of the total flux density. Here,  $\theta_{\text{MRS}} \approx 0.6\lambda/L_{\text{min}}$  was used for the estimation (ALMA Technical handbook), where  $\theta_{\text{MRS}}$  is the



**Figure 1.** Left: 850  $\mu\text{m}$  continuum image of the northern end of the ISF taken with the JCMT/SCUBA (Johnstone & Bally 1999). Right: observing fields of the ALMA 12 m array (blue circles: 92 pointings) and the ACA 7 m array (green circles: 32 pointings).

**Table 1**  
Observing Parameters

| Parameters                               | ACA 7 m Array   | ALMA 12 m Array |
|--|---|-----------------|
| Observation date (YYYY-MM-DD)            | 2018-4-19, 2018-4-20, 2018-4-23                                       | 2018-4-19       |
| Number of antennas                       | 12  | 44              |
| Mapping center (ICRS)                    | 05 <sup>h</sup> 35 <sup>m</sup> 26 <sup>s</sup> .7140, -05°10'03".800 |                 |
| Mapping area                             | 3'.1 × 2'.2   | 2'.9 × 1'.9     |
| Number of pointings                      | 32  | 92              |
| Primary beam size at 230.53 GHz (arcsec) | 44  | 26              |
| Continuum representative frequency (GHz) | 231   |                 |
| Continuum effective bandwidth (GHz)      | 3.4   |                 |
| PWV (mm)                                 | 1.4–3.0   | 1.9–2.3         |
| Phase rms <sup>a</sup> (deg)             | 8.4–17.5  | 8.6–21.6        |
| Projected baseline coverage (m)          | 7–47  | 12–493          |
| Maximum recoverable size (arcsec)        | 23  | 13              |
| On-source time per field (second)        | 540   | 40              |
| System temperature (K)                   | 80–120  | 70–170          |
| Flux calibrator                          | J0522-3627  | J0522-3627      |
| Bandpass calibrator                      | J0522-3627  | J0522-3627      |
| Phase calibrator                         | J0542-0913, J0607-0834  | J0541-0541      |

**Note.**

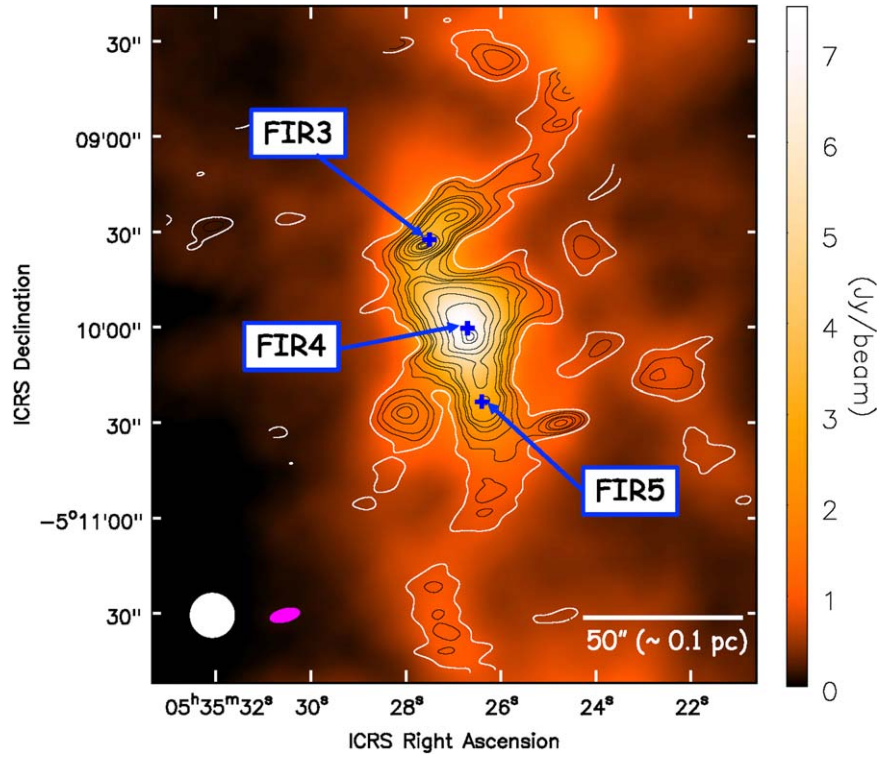
<sup>a</sup> Antenna-based phase differences on phase calibrator at the baseline of Q4 (phase rms values measured in the fourth quartile of the baseline length).

maximum recoverable size in radians,  $\lambda$  is the observing wavelength in meters, and  $L_{\min}$  is the shortest baseline in meters. Details of the observation parameters including further information such as the calibrators and observing conditions are summarized in Table 1.

The data were calibrated using the Common Astronomy Software Application (CASA; CASA Team et al. 2022) version 5.4.0 with the ALMA pipeline. The data were imaged with

CASA versions 5.6.1 and 5.6.2. The final 1.3 mm continuum image and the data cubes for the molecular line observations were produced using a CASA task “*tclean*.” Robust weighting with a Briggs parameter of 0.5 was used for both the continuum and molecular line images. The synthesized beams and noise levels ( $1\sigma$ ) obtained for the continuum images were  $1''.13 \times 0''.65$  (P.A. =  $-68^\circ$ ) and  $\sim 0.22 \text{ mJy beam}^{-1}$  for the ALMA 12 m array, and  $9''.63 \times 4''.19$  (P.A. =  $-76^\circ$ ) and





**Figure 2.** ACA 7 m array 1.3 mm continuum image (white and black contours, magenta beam ellipse) overlaid with JCMT/SCUBA 850  $\mu\text{m}$  continuum image (color scale and white beam ellipse, Johnstone & Bally 1999). The white contour level is  $10\sigma$  and the black contour levels are  $[20, 30, 50, 60, 80, 130, 180, 230, 300, 320, 340] \times 1\sigma$  ( $1\sigma = 0.78 \text{ mJy beam}^{-1}$ ). The crosses denote the locations of FIR 3, 4, and 5 (Chini et al. 1997).

**Table 2**  
Summary of the Imaging Parameters

| Data Set                  | Array | Briggs Weight | Synthesized Beam, P.A. (arcsec $\times$ arcsec, deg) | Noise Level ( $\text{mJy beam}^{-1}$ ) | Velocity Resolution ( $\text{km s}^{-1}$ ) | Figures              |
|---------------------------|-------|---------------|--|--|--|----------------------|
| 1.3 mm continuum          | 12 m  | 0.5           | $1.13 \times 0.65, -68$                              | 0.22                                   | ...  | 3, 4, 5, 17, 19 20   |
| 1.3 mm continuum          | 7 m   | 0.5           | $9.63 \times 4.19, -76$                              | 0.78                                   | ...  | 2, 19                |
| $^{12}\text{CO}(J = 2-1)$ | 12 m  | 0.5           | $1.19 \times 0.74, -68$                              | 5.3                                    | 5.0  | 7-9, 14, 15, 17, 21  |
| $\text{SiO}(J = 5-4)$     | 12 m  | 0.5           | $1.26 \times 0.79, -69$                              | 4.8                                    | 5.0  | 21                   |
| $^{12}\text{CO}(J = 2-1)$ | 12 m  | 0.5           | $1.19 \times 0.74, -68$                              | 10.0                                   | 1.0  | 10-13, 16, 22        |
| $\text{SiO}(J = 5-4)$     | 12 m  | 0.5           | $1.26 \times 0.79, -69$                              | 9.0                                    | 1.0  | 7-12, 14, 16, 17, 22 |

$\sim 0.78 \text{ mJy beam}^{-1}$  for the ACA 7 m array. The CO and SiO data cubes were produced using a velocity resolution of 5.0 and  $1.0 \text{ km s}^{-1}$  for the ALMA 12 m array. The synthesized beams obtained for the CO and SiO data cubes for the ALMA 12 m array were  $1''.19 \times 0''.74$  (P.A. =  $-68^\circ$ ) and  $1''.26 \times 0''.79$  (P.A. =  $-69^\circ$ ), respectively. Table 2 summarizes the achieved angular resolutions and noise levels, with the figure numbers indicating the image with the corresponding data set. After some trials, we decided to present the ALMA 12 m array and the ACA 7 m array images separately, rather than combine both data in order to demonstrate the most compact and the most extended structures using individual images.

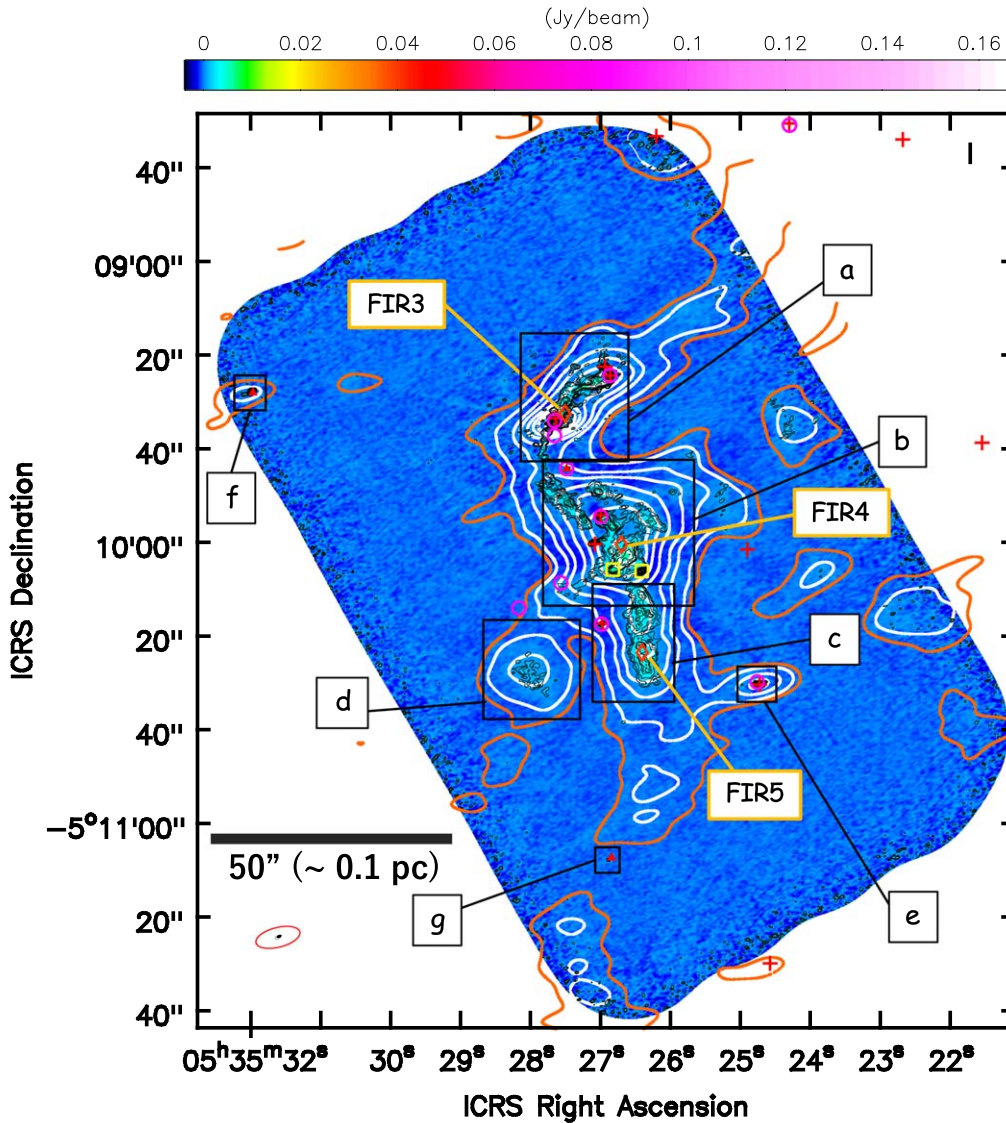
### 3. Results

#### 3.1. 1.3 mm Continuum Emission

Figure 2 shows that the spatial distribution of the 1.3 mm continuum image taken with the ACA 7 m array (white and black contours) is consistent with the  $850 \mu\text{m}$  continuum image taken with the JCMT/SCUBA (color scale, Johnstone & Bally 1999). The ACA 7 m array 1.3 mm continuum image

shows several substructures within the 1.3 mm sources, FIR 3, 4, and 5, previously identified by Chini et al. (1997). In addition, we detected two single-peak bright components with the ACA 7 m array, with peaks at R.A. =  $05^{\text{h}}35^{\text{m}}28^{\text{s}}.047$ , decl. =  $-05^\circ 10' 26''.474$  and R.A. =  $05^{\text{h}}35^{\text{m}}24^{\text{s}}.729$ , decl. =  $-05^\circ 10' 30''.145$ .

Figures 3 and 4 show the 1.3 mm continuum image obtained from the ALMA 12 m array. The spatial resolution of the 1.3 mm continuum for the ALMA 12 m array is about 7 times higher than that for the ACA 7 m array. The ALMA 12 m array provides further spatial resolution of the continuum emission detected with the ACA 7 m array. The ALMA 12 m array also detected structures associated with continuum sources detected in previous works such as at 3 mm continuum sources detected by Kainulainen et al. (2017) and van Terwisga et al. (2019) and 0.87 mm continuum sources detected by Tobin et al. (2019). The spatial resolution of our 1.3 mm continuum image obtained from the ALMA 12 m array is approximately 3 times higher than that of the 3 mm continuum in previous mosaic mapping observations (Kainulainen et al. 2017; van Terwisga et al. 2019). Tobin et al. (2019) observed 0.87 mm continuum



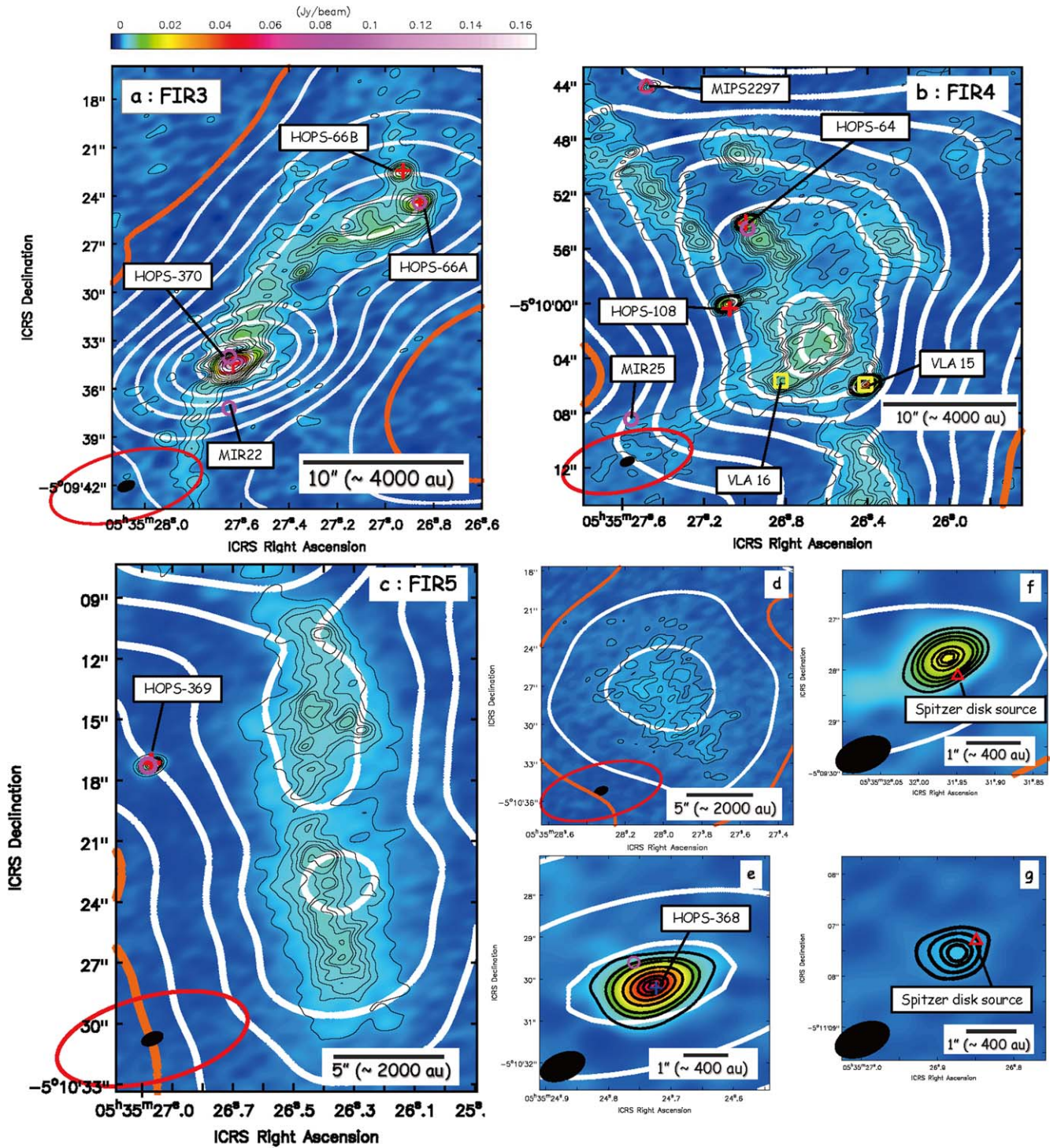
**Figure 3.** Continuum image by the ALMA 12 m array (color and black contours) and ACA 7 m array (orange and white contours). The noise levels ( $1\sigma$ ) for the 12 m array and 7 m array are  $0.22$  and  $0.78$   $\text{mJy beam}^{-1}$ , respectively. The black contour levels are  $[5, 7, 10, 15, 17, 20, 25, 32, 40, 50, 60, 80, 100, 150, 170, 220, 300, 500, 700] \times 1\sigma$  of the ALMA 12 m array. The orange contour level is  $10\sigma$  and the white contour levels are  $[20, 24, 50, 80, 130, 180, 230, 300, 320, 340] \times 1\sigma$  of the ACA 7 m array. The synthesized beams of the 12 m array and 7 m array are denoted by black-filled and red open ellipses in the bottom-left corner. The symbols represent HOPS sources (red crosses, Furlan et al. 2016), TIMMI2 mid-infrared sources (open pink circles, Nielbock et al. 2003), Spitzer disk sources (red triangles, Megeath et al. 2012), VLA sources (yellow squares, Osorio et al. 2017), and the central positions of the FIR regions (red diamonds, Chini et al. 1997).

emissions toward known IR sources with  $0''.1$  ( $\sim 40$  au) resolution, which is approximately 10 times higher than that of our ALMA 12 m array image, while the observations by Tobin et al. (2019) are single pointing toward individual protostellar sources. With mosaic mapping, we were able to image structures in the region that Tobin et al. (2019) did not cover. For example, relatively luminous sources were detected in our ALMA 12 m array image outside the FIR 3, 4, and 5 regions in addition to those in the densest part of the regions. We also detected fainter structures than those previously detected by Kainulainen et al. (2017), van Terwisga et al. (2019), and Tobin et al. (2019), as our observations have approximately two orders of magnitude better dust mass sensitivity compared to their observations (i.e.,  $3\sigma$  dust mass sensitivity of  $3.4 \times 10^{-5} M_{\odot}$  assuming  $T = 15$  K; see Section 3.1.2). Here, the dust mass sensitivity was estimated per corresponding observed beam. Finally, we successfully

resolved substructures such as filamentary and compact structures, including those not previously identified. In the following, we describe more details of the individual regions presented in Figures 4(a)–(g). Identification of the described sources below is made with Astronomical Dendrograms (Rosolowsky et al. 2008) as introduced in Section 3.1.1.

FIR 3 region (Figure 4(a)): three continuum sources were detected with the ALMA 12 m array. One of the detected sources is associated with a Class I source with a peak flux of  $156 \text{ mJy beam}^{-1}$ , HOPS-370. In previous works (e.g., Nielbock et al. 2003), HOPS-370 was identified as a member of a binary system (the two pink circles around HOPS-370 in Figure 4(a)). However, we only detected the northern source in the 1.3 mm continuum emission. This result is consistent with a recent ALMA study using 0.87 mm continuum observations (e.g., Tobin et al. 2019). The other two sources are for a binary system, HOPS-66A/B, which has a flat spectrum (Class flat





**Figure 4.** Zoomed-in images of regions (a)–(g) in Figure 3. The orange and white contour levels and the color scale in all figures are the same as those in Figure 3. The black contour levels in panel (a) are  $[5, 10, 15, 20, 25, 30, 40, 50, 70, 100, 150, 200, 300, 500, 700] \times 1\sigma$  ( $1\sigma = 0.22 \text{ mJy beam}^{-1}$ ). The black contour levels in panel (b) are  $[3, 6, 10, 13, 15, 17, 20, 22, 25, 30, 50, 60, 68, 70, 80, 100, 120, 150, 175] \times 1\sigma$  ( $1\sigma = 0.22 \text{ mJy beam}^{-1}$ ). The black contour levels in panel (c) are  $[5, 10, 13, 15, 17, 18, 20, 25, 30, 33] \times 1\sigma$  ( $1\sigma = 0.22 \text{ mJy beam}^{-1}$ ). The black contour levels in panel (d) are  $[3, 5, 7] \times 1\sigma$  ( $1\sigma = 0.22 \text{ mJy beam}^{-1}$ ). The black contour levels in panel (e) are  $[10, 30, 50, 100, 150, 200, 230, 250] \times 1\sigma$  ( $1\sigma = 0.22 \text{ mJy beam}^{-1}$ ). The black contour levels in panel (f) are  $[20, 30, 40, 50, 70, 80, 85] \times 1\sigma$  ( $1\sigma = 0.22 \text{ mJy beam}^{-1}$ ). The black contour levels in panel (g) are  $[3, 5, 7, 8] \times 1\sigma$  ( $1\sigma = 0.22 \text{ mJy beam}^{-1}$ ). The black-filled and red open ellipses are the same as those in Figure 3.

categorized in Furlan et al. 2016) corresponding to the Class I/II boundary. HOPS-66 was identified as a single source by infrared observations (Furlan et al. 2016). The follow-up 0.87 and 9 mm continuum observations, however, resolved out the

single source and newly identified it as a binary system, HOPS-66A/B (Tobin et al. 2019).

FIR 4 region (Figure 4(b)): within a single-peak structure imaged with the ACA 7 m array (white contours), we detected

**Table 3**  
Integrated Flux Density in the Selected Area ( $F_\nu$ ) and Concentration Factor ( $C_{(ACA/JCMT)}$ )

| Region   | Figures | $F_{850 \mu\text{m}}$<br>(mJy) | Extrapolated Flux at 1.3 mm<br>(mJy) <sup>a</sup> | Sp. Index<br>( $\beta$ ) | $F_{1.3 \text{ mm}}$ for the ACA 7 m Array<br>(mJy) (JCMT beam) | $C_{(ACA/JCMT)}$<br>(%) |
|----------|---------|--------------------------------|---|--------------------------|---|-------------------------|
| FIR 3    | 4(a)    | 9030                           | 1875  | 1.7 <sup>b</sup>         | 874   | 46.6                    |
| FIR 4    | 4(b)    | 20930                          | 4731  | 1.5 <sup>b</sup>         | 2120  | 44.8                    |
| FIR 5    | 4(c)    | 8770                           | 1982  | 1.5 <sup>b</sup>         | 691   | 34.9                    |
| ...      | 4(d)    | 2060                           | 466   | 1.5 <sup>b</sup>         | 143   | 30.7                    |
| HOPS-368 | 4(e)    | 632                            | 111   | 2.1 <sup>c</sup>         | 55  | 49.7                    |

**Notes.** The beam sizes of the data for the ACA 7 m array 1.3 mm continuum was adjusted to  $\sim 14''$  using the CASA task “imsmooth” (sixth column). All the cells in the region over  $10\sigma$  for the ACA 7 m array continuum were selected (white and orange contours in Figures 2 and 4, respectively), and  $F_\nu$  was calculated using them.  $C_{(ACA/JCMT)}$  is the ratio of  $F_\nu$  for the ACA 7 m array 1.3 mm continuum (beam  $\sim 14''$ ) to  $F_\nu$  for the extrapolated 850  $\mu\text{m}$  continuum.

<sup>a</sup> Calculated using  $F_\nu \propto \nu^{\beta+2}$ .

<sup>b</sup> Sadavoy et al. (2016).

<sup>c</sup> Tobin et al. (2019) (index with 0.87–0.9 mm).

substructures with the ALMA 12 m array (black contours). They are part of filamentary structures within which several compact sources are embedded. Although the 1.3 mm continuum emission obtained from the ACA 7 m array shows a single peak, there is no corresponding compact peaked component in the higher-resolution 12 m array image. Instead of a single peak, an extended fluffy structure was detected with the ALMA 12 m array (black contours). The four most compact 1.3 mm continuum sources are associated with previously identified sources: two IR sources (HOPS-64 and HOPS-108; Furlan et al. 2016) and two centimeter sources (VLA 15 and VLA 16; Osorio et al. 2017). These four continuum sources were identified in previous ALMA continuum observations by Kainulainen et al. (2017), van Terwisga et al. (2019), and Tobin et al. (2019).

FIR 5 region (Figure 4(c)): two extended filamentary structures were detected with the ALMA 12 m array. No compact sources were detected within the filamentary structures. This result is different from those for both the FIR 3 and FIR 4 regions described above. A compact 1.3 mm continuum source associated with HOPS-369 (Furlan et al. 2016) was detected outside the filamentary structure.

Figure 4(d): with the ACA 7 m array, we detected a single-peak structure ( $\sim 4000$  au scale), which has already been reported in previous ALMA observations (e.g., Kainulainen et al. 2017; Hacar et al. 2018; Zhang et al. 2020). Our ALMA continuum observations spatially resolved patchy substructures within the single-peak structure corresponding to the  $3\sigma$ – $8\sigma$  emission levels, which is the first time these substructures have been resolved.

Figures 4(e)–(g): we detected three compact sources associated with previously detected IR sources (HOPS-368 and two Spitzer disk sources) outside the FIR 3, 4, and 5 regions.

To evaluate the concentration of the structures, we defined  $C_{(ACA/JCMT)}$  as the ratio between the flux measured by the ACA 7 m array and that measured by the JCMT after taking account of the beam size and wavelength differences, and  $C_{(12 \text{ m}/ACA)}$  as the ratio between the flux measured by the ALMA 12 m array and that measured by the ACA 7 m array after taking into account the beam size differences. The structure concentration factor  $C$  indicates the flux-recovery rate for comparing two different experiments. For  $C_{(ACA/JCMT)}$  presented in Table 3, we estimated ratio ranges between 31% and 50%. The number did not vary much across the regions. Here, we assumed spectral index  $\beta = 1.5$ – $2.1$  listed in Table 3

**Table 4**  
Integrated Flux Density in the Selected Area ( $F_\nu$ ) and Concentration Factor ( $C_{(12 \text{ m}/ACA)}$ )

| Region   | Figures | $F_{1.3 \text{ mm}}$ for the<br>ACA 7 m Array<br>(mJy) | $F_{1.3 \text{ mm}}$ for the<br>ALMA 12 m<br>Array<br>(mJy)<br>(ACA beam) | $C_{(12 \text{ m}/ACA)}$<br>(%) |
|----------|---------|--|---|---------------------------------|
| FIR 3    | 4(a)    | 919  | 610   | 66.4                            |
| FIR 4    | 4(b)    | 2220   | 709   | 31.9                            |
| FIR 5    | 4(c)    | 752  | 318   | 42.3                            |
| ...      | 4(d)    | 166  | 74  | 44.5                            |
| HOPS-368 | 4(e)    | 76   | 80  | 104.7                           |

**Note.** The beam sizes of the data for the ALMA 12 m array 1.3 mm continuum were adjusted to  $\sim 9''$  using the CASA task “imsmooth” (fourth column). All the cells in the region over  $10\sigma$  for the ACA 7 m array continuum were selected (white and orange contours in Figures 2 and 4, respectively), and  $F_\nu$  was calculated using them.  $C_{(12 \text{ m}/ACA)}$  is the ratio of  $F_\nu$  for the ALMA 12 m array 1.3 mm continuum (beam  $\sim 9''$ ) to  $F_\nu$  for the ACA 7 m array 1.3 mm continuum (original data).

to estimate the extrapolated flux at 1.3 mm. For  $C_{(12 \text{ m}/ACA)}$  presented in Table 4, the estimated ratio varies depending on the regions (30%–100%).  $C_{(12 \text{ m}/ACA)}$  obtained toward HOPS-368 (a relatively isolated Class I source) was  $\sim 100\%$ , indicating no missing flux. This can be interpreted as indicating that the emission is mostly due to compact emission associated with a compact dusty disk and that the extended emission from the envelope or core can be ignored. For the same reason, the FIR 3 region, including one Class I source and a binary system of flat sources, shows a relatively high flux-recovery rate ( $\sim 66\%$ ). In contrast, the FIR 4 region, FIR 5 region, and the region presented in Figure 4(d) show small flux-recovery rates of  $C_{(12 \text{ m}/ACA)} = 31\%$ – $44\%$ . These regions contain Class 0 and prestellar sources embedded within the filamentary structures. They are considered to be young compared with HOPS-368 and the sources in the FIR 3 region. Thus, the extended emission from the envelope and core remains.

### 3.1.1. Source Identifications Using the ALMA 12 m Array Continuum Data

In order to uniformly identify the continuum sources for our 1.3 mm continuum image, we used Astronomical Dendrograms (hereafter dendrograms, Rosolowsky et al. 2008; Goodman



et al. 2009). Dendrograms is a structure-identifying algorithm package that abstracts the hierarchical structure of 2D ( $p$ - $p$ ) or 3D ( $p$ - $p$ - $v$ ) data cubes into a visualized representation (Goodman et al. 2009). Dendrograms use three types of representations: *leaves*, *branches*, and *trunk*. The trunk is the base of the hierarchical structure. Branches are structures that split into multiple substructures. Leaves do not include further substructures and are the most compact components. We applied dendrograms to the 1.3 mm continuum image obtained by the ALMA 12 m array with the following three criteria: (1) the structure size is larger than the beam size ( $\text{min\_npix} = 40$ , 1 pixel =  $0''.1$ ), (2) the minimum value of a leaf is more than  $5\sigma$  ( $\text{min\_value} = 5\sigma$ ,  $1\sigma = 0.22$  mJy beam $^{-1}$ ), and (3) the peak flux density of a leaf measured from a nearby local minimum value is more than  $3\sigma$  ( $\text{min\_delta} = 3\sigma$ ). Figure 5 shows the location of identified leaves (top panel) and the tree structure of the 1.3 mm continuum emission (bottom panel) by a dendrogram analysis. As shown in the top panel of Figure 5, dendrograms identified compact structures and faint extended structures as leaves.

Figure 5 (bottom) shows five branches. They are located in the FIR 3, 4, and 5 regions indicating that the three regions contain hierarchical structures. In this study, we used the dendrogram leaves to identify the 1.3 mm continuum sources. In a future paper, we will further discuss the hierarchical structures within the molecular cloud.

We identified 51 continuum sources in total. We call the set the fragmented source catalog in Orion (FraSCO) and indicate the sources within the set by numbers, ordered from north to south in R.A. Most of the identified sources are distributed in the main filamentary structure. The source name, position, peak flux, total flux, and radius of the identified sources are summarized in Table 5. The source position is measured at the peak flux of the leaf. The total flux is measured within the identified leaf. The radius is defined as  $\sqrt{A_{\text{leaf}}/\pi}$ , where  $A_{\text{leaf}}$  is the projected area of a leaf onto the plane of the sky. Note that dendrograms also compute the radius based on the geometric mean of the second moments along the major axis and minor axis. For our data set, the radius computed from the second moments is a factor of 2 smaller than that measured from the projected area. The radius comparisons made in Rosolowsky et al. (2008) for large-scale clumps (comparisons of approximately parsec scale structures) imply that the radii computed from the second moments are smaller than those measured in previous studies. Although our study focuses on smaller size scale structures ( $\sim 1000$  au) compared to Rosolowsky et al. (2008), the trend is consistent with what was reported in their study.

We also compare the identified sources with the previously detected sources in Table 6 (also see Appendix A). For 15 out of the identified 51 sources, there are counterparts previously detected at other wavelengths and located within  $1''$  from our identified sources. The 15 sources are composed of three Class II sources, seven Class 0/I/flat sources, and five sources previously identified with only millimeter/submillimeter wavelength (no classification). The five millimeter/submillimeter sources are considered to be still deeply embedded within the molecular core or too cold to detect clearly at infrared wavelengths. The remaining 36 sources were identified for the first time in this study. We also confirmed these by eye

and compared them with the synthesized beam pattern. We made sure that the detected faint sources are not side-lobe components created by a strong continuum source such as FraSCO-16 (i.e., HOPS-370).

### 3.1.2. Dust Mass

Assuming that the 1.3 mm continuum emission comes from optically thin dust emission and the temperature distribution of the continuum source is uniform, we can estimate the lower limit of the dust mass as

$$M_{\text{dust}} = \frac{F_{\lambda} d^2}{\kappa_{\lambda} B_{\lambda}(T_{\text{dust}})}, \quad (1)$$

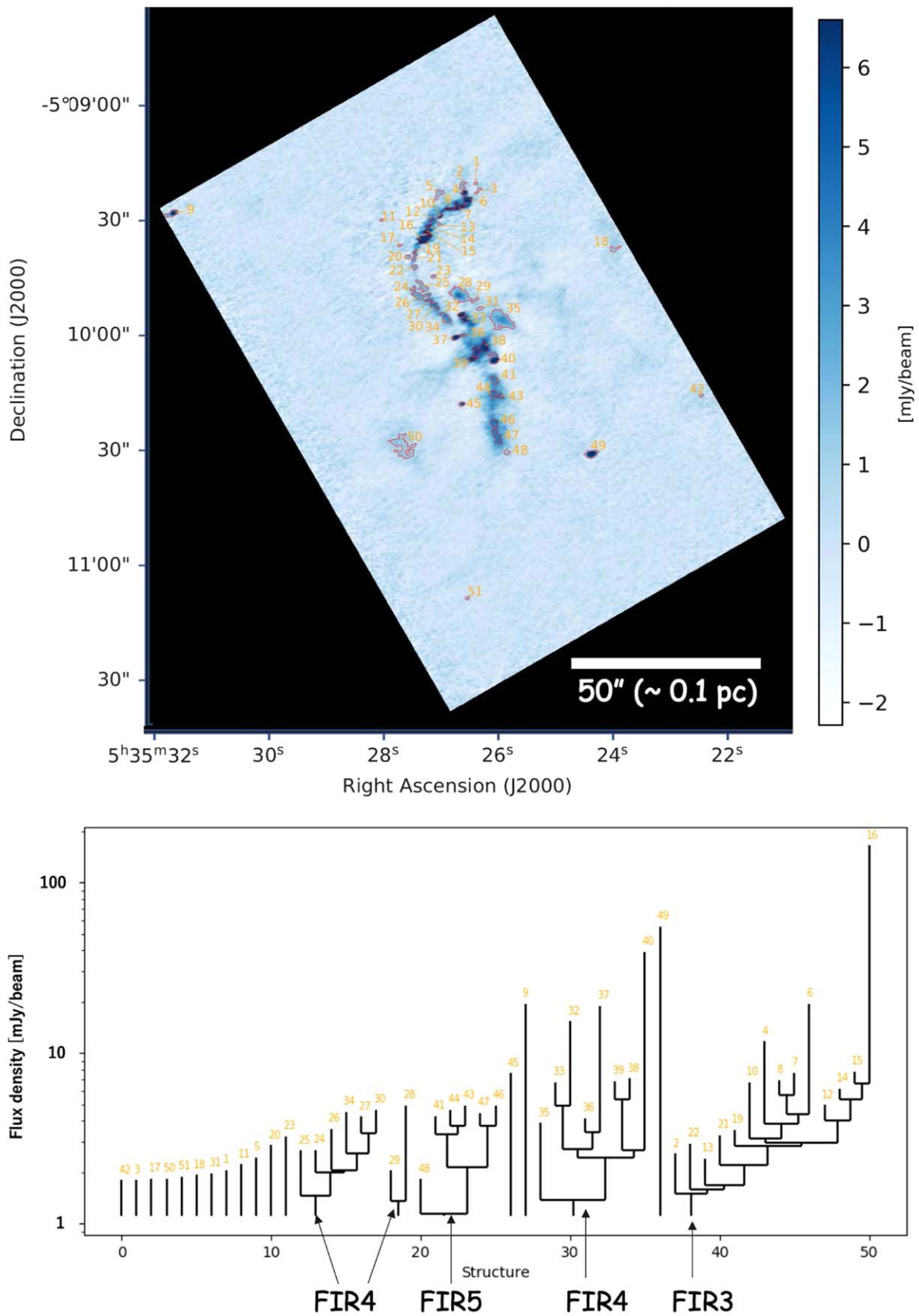
where  $\kappa_{\lambda}$  is the mass-absorption coefficient for dust grains,  $B_{\lambda}$  is the Planck function for the dust temperature  $T_{\text{dust}}$ ,  $F_{\lambda}$  is the total flux density for the continuum source emission, and  $d$  is the distance to the source. The dust masses are listed in Table 7, adopting a dust opacity of  $\kappa_{\lambda} = 0.899$  cm $^2$  g $^{-1}$  (Ossenkopf & Henning 1994), dust temperatures of  $T_{\text{dust}} = 15$  K (Li et al. 2013; Sadavoy et al. 2016; Tatematsu et al. 2016; Kirk et al. 2017; Mason et al. 2020; Zhang et al. 2020), and  $d = 400$  pc (Großschedl et al. 2018; Tobin et al. 2020). Assuming that the gas-to-dust mass ratio is 100:1 (Hayashi 1981) and that the geometrical structure of the identified source is a sphere, the mean molecular hydrogen number densities for the sources are  $n_{\text{H}_2} = M_{\text{H}_2}/((4/3)\pi r^3 \mu m_{\text{H}})$ . Here,  $M_{\text{H}_2}$ ,  $r$ ,  $\mu$ , and  $m_{\text{H}}$  are the gas mass of the source, the continuum source radius, the mean molecular weight ( $\mu = 2.33$ ), and the hydrogen mass, respectively. Table 7 also describes the mean molecular hydrogen number densities for the sources.

The 1.3 mm continuum emission might be contaminated by the free-free emission associated with the YSO ionized jet (Osorio et al. 2017). To estimate the contribution from the free-free emission at the 1.3 mm wavelength, we used the spectral index,  $\alpha$  ( $F_{\nu} \propto \nu^{\alpha}$ ), obtained between 1.3 and 5 cm (Osorio et al. 2017). Osorio et al. (2017) detected seven centimeter sources associated with protostars or YSOs and three centimeter sources considered to be jet knots. With the ALMA 12 m array, we detected six 1.3 mm continuum sources associated with the protostars or YSOs detected by Osorio et al. (2017). We estimated  $\alpha$  for the centimeter sources to be between 0.28 and 1.35 with a mean value of 0.7 using the number reported in Osorio et al. (2017), consistent with the mean  $\alpha$  of 0.6 estimated for the ionized jet by Anglada et al. (1998). Using  $\alpha$ , we concluded that up to 7.0% of the 1.3 mm emission can be attributed to the free-free emission, but the majority of the emission originates from the thermal dust.

### 3.1.3. Jeans Analysis

As described in Section 3.1.2, the detected 1.3 mm sources have dust masses and gas number densities in the range of  $3.8 \times 10^{-5}$ – $1.1 \times 10^{-2} M_{\odot}$  and  $6.4 \times 10^6$ – $3.3 \times 10^8$  cm $^{-3}$ , respectively. To investigate the gravitational stability, we performed a Jeans analysis. Assuming an infinite and homogeneous medium, the Jeans length is described as follows





**Figure 5.** Top: location of 1.3 mm continuum sources. 51 sources (ID = 1–51) were identified as leaves applying dendrograms to the ALMA 12 m array image. The red contours represent individual structures of continuum sources. Bottom: tree structure of the continuum sources with ID. The five tree structures belong to the FIR 3, 4, and 5 regions, respectively.

**Table 5**  
Source Identifications with Dendrograms

| ID | Source Name      | R.A. (ICRS)   | Decl. (ICRS)    | Radius (arcsec) | Peak Flux (mJy beam <sup>-1</sup> ) | Integrated Flux (mJy) |
|----|------------------|---|-----------------|-----------------|-------------------------------------|-----------------------|
| 1  | <b>FraSCO-1</b>  | 05 <sup>h</sup> 35 <sup>m</sup> 26 <sup>s</sup> .7325 | -05°09'20".6600 | 0.36            | 2.06                                | 0.75                  |
| 2  | <b>FraSCO-2</b>  | 05 <sup>h</sup> 35 <sup>m</sup> 26 <sup>s</sup> .9636 | -05°09'20".6044 | 0.80            | 2.57                                | 4.62                  |
| 3  | <b>FraSCO-3</b>  | 05 <sup>h</sup> 35 <sup>m</sup> 26 <sup>s</sup> .6859 | -05°09'21".9646 | 0.57            | 1.79                                | 1.66                  |
| 4  | FraSCO-4         | 05 <sup>h</sup> 35 <sup>m</sup> 26 <sup>s</sup> .9328 | -05°09'22".5670 | 0.70            | 11.70                               | 12.41                 |
| 5  | <b>FraSCO-5</b>  | 05 <sup>h</sup> 35 <sup>m</sup> 27 <sup>s</sup> .3703 | -05°09'22".7829 | 0.97            | 2.45                                | 5.93                  |
| 6  | FraSCO-6         | 05 <sup>h</sup> 35 <sup>m</sup> 26 <sup>s</sup> .8765 | -05°09'24".4338 | 0.99            | 19.36                               | 30.84                 |
| 7  | <b>FraSCO-7</b>  | 05 <sup>h</sup> 35 <sup>m</sup> 27 <sup>s</sup> .2180 | -05°09'26".1418 | 0.89            | 7.69                                | 19.11                 |
| 8  | <b>FraSCO-8</b>  | 05 <sup>h</sup> 35 <sup>m</sup> 27 <sup>s</sup> .1984 | -05°09'26".7078 | 0.54            | 6.93                                | 6.97                  |
| 9  | FraSCO-9         | 05 <sup>h</sup> 35 <sup>m</sup> 31 <sup>s</sup> .9781 | -05°09'27".8434 | 1.12            | 19.40                               | 24.52                 |
| 10 | <b>FraSCO-10</b> | 05 <sup>h</sup> 35 <sup>m</sup> 27 <sup>s</sup> .3491 | -05°09'28".6333 | 0.60            | 6.76                                | 6.21                  |
| 11 | <b>FraSCO-11</b> | 05 <sup>h</sup> 35 <sup>m</sup> 28 <sup>s</sup> .3645 | -05°09'29".5757 | 0.37            | 2.22                                | 0.81                  |
| 12 | <b>FraSCO-12</b> | 05 <sup>h</sup> 35 <sup>m</sup> 27 <sup>s</sup> .4959 | -05°09'29".5413 | 0.59            | 4.97                                | 5.92                  |
| 13 | <b>FraSCO-13</b> | 05 <sup>h</sup> 35 <sup>m</sup> 27 <sup>s</sup> .3666 | -05°09'30".7253 | 0.38            | 2.40                                | 1.11                  |
| 14 | <b>FraSCO-14</b> | 05 <sup>h</sup> 35 <sup>m</sup> 27 <sup>s</sup> .5490 | -05°09'31".2365 | 0.49            | 6.21                                | 5.12                  |
| 15 | <b>FraSCO-15</b> | 05 <sup>h</sup> 35 <sup>m</sup> 27 <sup>s</sup> .5914 | -05°09'32".7387 | 0.47            | 7.77                                | 5.90                  |
| 16 | FraSCO-16        | 05 <sup>h</sup> 35 <sup>m</sup> 27 <sup>s</sup> .6322 | -05°09'34".4991 | 1.25            | 164.64                              | 223.11                |
| 17 | <b>FraSCO-17</b> | 05 <sup>h</sup> 35 <sup>m</sup> 28 <sup>s</sup> .4580 | -05°09'36".1552 | 0.37            | 1.83                                | 0.76                  |
| 18 | <b>FraSCO-18</b> | 05 <sup>h</sup> 35 <sup>m</sup> 24 <sup>s</sup> .3357 | -05°09'37".6100 | 0.77            | 1.92                                | 3.13                  |
| 19 | <b>FraSCO-19</b> | 05 <sup>h</sup> 35 <sup>m</sup> 27 <sup>s</sup> .7866 | -05°09'37".7639 | 0.39            | 3.54                                | 1.88                  |
| 20 | <b>FraSCO-20</b> | 05 <sup>h</sup> 35 <sup>m</sup> 27 <sup>s</sup> .9120 | -05°09'39".1008 | 0.60            | 2.88                                | 2.51                  |
| 21 | <b>FraSCO-21</b> | 05 <sup>h</sup> 35 <sup>m</sup> 27 <sup>s</sup> .7985 | -05°09'39".3549 | 0.62            | 3.30                                | 3.84                  |
| 22 | <b>FraSCO-22</b> | 05 <sup>h</sup> 35 <sup>m</sup> 27 <sup>s</sup> .7952 | -05°09'41".8262 | 0.64            | 2.94                                | 3.36                  |
| 23 | FraSCO-23        | 05 <sup>h</sup> 35 <sup>m</sup> 27 <sup>s</sup> .4689 | -05°09'44".1767 | 0.49            | 3.26                                | 1.82                  |
| 24 | <b>FraSCO-24</b> | 05 <sup>h</sup> 35 <sup>m</sup> 27 <sup>s</sup> .8163 | -05°09'47".3895 | 0.54            | 2.69                                | 2.57                  |
| 25 | <b>FraSCO-25</b> | 05 <sup>h</sup> 35 <sup>m</sup> 27 <sup>s</sup> .6642 | -05°09'46".7290 | 1.09            | 2.68                                | 8.30                  |
| 26 | <b>FraSCO-26</b> | 05 <sup>h</sup> 35 <sup>m</sup> 27 <sup>s</sup> .6948 | -05°09'49".1693 | 1.22            | 3.58                                | 14.09                 |
| 27 | <b>FraSCO-27</b> | 05 <sup>h</sup> 35 <sup>m</sup> 27 <sup>s</sup> .5511 | -05°09'50".3347 | 0.52            | 4.23                                | 3.79                  |
| 28 | FraSCO-28        | 05 <sup>h</sup> 35 <sup>m</sup> 27 <sup>s</sup> .9700 | -05°09'49".5700 | 2.00            | 4.92                                | 37.32                 |
| 29 | <b>FraSCO-29</b> | 05 <sup>h</sup> 35 <sup>m</sup> 26 <sup>s</sup> .7462 | -05°09'50".3119 | 0.63            | 2.04                                | 2.54                  |
| 30 | <b>FraSCO-30</b> | 05 <sup>h</sup> 35 <sup>m</sup> 27 <sup>s</sup> .4488 | -05°09'51".7606 | 0.85            | 4.66                                | 10.68                 |
| 31 | <b>FraSCO-31</b> | 05 <sup>h</sup> 35 <sup>m</sup> 26 <sup>s</sup> .6624 | -05°09'52".4792 | 0.61            | 1.97                                | 2.04                  |
| 32 | FraSCO-32        | 05 <sup>h</sup> 35 <sup>m</sup> 26 <sup>s</sup> .9843 | -05°09'54".1045 | 0.70            | 15.37                               | 15.73                 |
| 33 | <b>FraSCO-33</b> | 05 <sup>h</sup> 35 <sup>m</sup> 26 <sup>s</sup> .9178 | -05°09'55".3142 | 0.77            | 6.72                                | 12.68                 |
| 34 | <b>FraSCO-34</b> | 05 <sup>h</sup> 35 <sup>m</sup> 27 <sup>s</sup> .2507 | -05°09'54".9636 | 1.12            | 4.52                                | 15.41                 |
| 35 | FraSCO-35        | 05 <sup>h</sup> 35 <sup>m</sup> 26 <sup>s</sup> .2906 | -05°09'55".4723 | 2.45            | 3.88                                | 51.81                 |
| 36 | <b>FraSCO-36</b> | 05 <sup>h</sup> 35 <sup>m</sup> 26 <sup>s</sup> .9453 | -05°09'59".3577 | 0.42            | 4.15                                | 2.52                  |
| 37 | FraSCO-37        | 05 <sup>h</sup> 35 <sup>m</sup> 27 <sup>s</sup> .8060 | -05°10'00".1570 | 0.78            | 18.81                               | 19.79                 |
| 38 | <b>FraSCO-38</b> | 05 <sup>h</sup> 35 <sup>m</sup> 26 <sup>s</sup> .6430 | -05°10'03".1720 | 1.43            | 7.08                                | 45.36                 |
| 39 | FraSCO-39        | 05 <sup>h</sup> 35 <sup>m</sup> 26 <sup>s</sup> .7936 | -05°10'05".6117 | 0.70            | 6.84                                | 10.98                 |
| 40 | FraSCO-40        | 05 <sup>h</sup> 35 <sup>m</sup> 26 <sup>s</sup> .4139 | -05°10'05".7640 | 1.28            | 39.13                               | 55.45                 |
| 41 | <b>FraSCO-41</b> | 05 <sup>h</sup> 35 <sup>m</sup> 26 <sup>s</sup> .4059 | -05°10'11".9170 | 0.89            | 4.26                                | 11.12                 |
| 42 | <b>FraSCO-42</b> | 05 <sup>h</sup> 35 <sup>m</sup> 22 <sup>s</sup> .8239 | -05°10'15".7530 | 0.43            | 1.79                                | 0.97                  |
| 43 | <b>FraSCO-43</b> | 05 <sup>h</sup> 35 <sup>m</sup> 26 <sup>s</sup> .3173 | -05°10'15".1954 | 0.63            | 4.93                                | 6.17                  |
| 44 | <b>FraSCO-44</b> | 05 <sup>h</sup> 35 <sup>m</sup> 26 <sup>s</sup> .4303 | -05°10'14".6234 | 0.84            | 4.64                                | 11.12                 |
| 45 | FraSCO-45        | 05 <sup>h</sup> 35 <sup>m</sup> 26 <sup>s</sup> .9738 | -05°10'17".2435 | 0.66            | 7.60                                | 5.87                  |
| 46 | FraSCO-46        | 05 <sup>h</sup> 35 <sup>m</sup> 26 <sup>s</sup> .4099 | -05°10'22".2276 | 0.96            | 4.93                                | 14.47                 |
| 47 | <b>FraSCO-47</b> | 05 <sup>h</sup> 35 <sup>m</sup> 26 <sup>s</sup> .3680 | -05°10'25".6531 | 1.21            | 4.46                                | 22.32                 |
| 48 | <b>FraSCO-48</b> | 05 <sup>h</sup> 35 <sup>m</sup> 26 <sup>s</sup> .1940 | -05°10'29".7729 | 0.65            | 1.82                                | 2.20                  |
| 49 | FraSCO-49        | 05 <sup>h</sup> 35 <sup>m</sup> 24 <sup>s</sup> .7303 | -05°10'30".1727 | 1.28            | 55.09                               | 74.26                 |
| 50 | <b>FraSCO-50</b> | 05 <sup>h</sup> 35 <sup>m</sup> 27 <sup>s</sup> .9954 | -05°10'28".2880 | 2.27            | 1.83                                | 26.09                 |
| 51 | FraSCO-51        | 05 <sup>h</sup> 35 <sup>m</sup> 26 <sup>s</sup> .8767 | -05°11'07".5346 | 0.44            | 1.89                                | 1.08                  |

**Note.** The source ID (1–51) corresponds to the number in Figure 5. The source names in bold represent newly identified 1.3 mm continuum sources. The data in Tables 5 and 7 is available in a machine-readable format.

(This table is available in machine-readable form.)

(Jeans 1902):

$$\lambda_{\text{frag}} = \sqrt{\frac{\pi c_s^2}{G \rho_0}}, \quad (2)$$

where  $G$  is the gravitational constant,  $\rho_0$  is the mean density, and  $c_s$  is the speed of sound. The relation between the speed of sound and the gas temperature is described as  $c_s = \sqrt{kT_{\text{gas}}/\mu m_{\text{H}}}$ , where  $T_{\text{gas}}$  is the gas temperature and  $k$  is the Boltzmann constant. From Equation (2), the critical number density is derived as

**Table 6**  
Summary of Multiwavelength Counterparts with Respect to the Identified 1.3 mm Continuum Sources

| Source Name | 5 cm <sup>a</sup> | 3.6 cm <sup>b</sup> | 3 cm <sup>a</sup> | 9 mm <sup>c</sup> | 7 mm <sup>a</sup> | 3 mm <sup>d</sup> | 870 $\mu\text{m}$ <sup>d</sup> | Infrared <sup>e,f,g</sup> | Class <sup>e</sup> |
|-------------|-------------------|---------------------|-------------------|-------------------|-------------------|-------------------|--------------------------------|---------------------------|--------------------|
| FraSCO-4    |                   |                     |                   | Detected          |                   |                   | Detected                       | HOPS-66B                  | Flat               |
| FraSCO-6    |                   |                     |                   | Detected          |                   | P10               | Detected                       | HOPS-66A/MIR20            | Flat               |
| FraSCO-9    |                   |                     |                   |                   |                   | D4                |                                | Spitzer disk source       | II                 |
| FraSCO-16   | VLA 11            | VLA 11              | VLA 11            | Detected          | VLA 11            | P1                | Detected                       | HOPS-370/MIR21            | I                  |
| FraSCO-23   | MIPS2297          |                     | MIPS2297          | Detected          | MIPS2297          | D23               | Detected                       | MIR 23                    | II                 |
| FraSCO-28   |                   |                     |                   |                   |                   | U7                |                                |                           |                    |
| FraSCO-32   | HOPS-64           |                     | HOPS-64           | Detected          | HOPS-64           | P12               | Detected                       | HOPS-64/MIR24             | I                  |
| FraSCO-35   |                   |                     |                   |                   |                   | U17               |                                |                           |                    |
| FraSCO-37   | HOPS-108          | VLA 12              | HOPS-108          | Detected          | HOPS-108          | P15               | Detected                       | HOPS-108                  | 0                  |
| FraSCO-39   | VLA 16            |                     | VLA 16            | Detected          | VLA 16            | U8                | Detected                       |                           |                    |
| FraSCO-40   | VLA 15            |                     | VLA 15            | Detected          | VLA 15            | U2                | Detected                       |                           |                    |
| FraSCO-45   |                   |                     |                   | Detected          |                   | P22               | Detected                       | HOPS-369/MIR 27           | Flat               |
| FraSCO-46   |                   |                     |                   |                   |                   | U20               |                                |                           |                    |
| FraSCO-49   |                   | VLA 13              |                   | Detected          |                   | P9                | Detected                       | HOPS-368/MIR28            | I                  |
| FraSCO-51   |                   |                     |                   |                   |                   | D30               |                                | Spitzer disk source       | II                 |

**Notes.**

<sup>a</sup> VLA 5 cm, 3 cm, 7 mm (Osorio et al. 2017).

<sup>b</sup> VLA 3.6 cm (Reipurth et al. 1999).

<sup>c</sup> VLA 9 mm and ALMA 870  $\mu\text{m}$  (Tobin et al. 2019).

<sup>d</sup> ALMA 3 mm sources as disk source (D), as protostar (P), and as no IR detected (U) (van Terwisga et al. 2019).

<sup>e</sup> HOPS sources (Furlan et al. 2016).

<sup>f</sup> Mid-infrared sources (Nielbock et al. 2003).

<sup>g</sup> Spitzer disk sources (Megeath et al. 2012).

follows:

$$n_{\text{H}_2}(\lambda_{\text{frag}}, T_{\text{gas}}) = \frac{\pi k}{G(\mu\text{m}_{\text{H}})^2} \frac{T_{\text{gas}}}{\lambda_{\text{frag}}^2}. \quad (3)$$

Figure 6 shows the relation between the  $\text{H}_2$  gas number density and radius for the continuum sources. Using a solid curve, we also plotted the Jeans critical number density as a function of radius, with  $r = \lambda_{\text{frag}}/2$  and a gas temperature of 15 K (e.g., Tatematsu et al. 2016). Here, we assumed that the gas temperature is equal to the dust temperature (see Section 3.1.2). The critical number density determines whether the identified sources are gravitationally bound, with the sources being bound when the gas number density is above the critical number density.

It should be noted that we assumed that the turbulent/nonthermal motions are acting isotropically and therefore can be treated as thermal-like support. Recent interferometric observations toward the OMC-2/3 region show that the nonthermal velocity dispersion of the spatially resolved cores is  $0.12 \pm 0.05 \text{ km s}^{-1}$ , whereas the mean thermal velocity dispersion for  $\text{H}_2$  gas is estimated to be  $0.23 \text{ km s}^{-1}$  at the gas temperature of 15 K (Zhang et al. 2020). These results indicate that the detected cores are thermal dominant. Moreover, Takahashi et al. (2013) and Teixeira et al. (2016) presented that the fragmentation length within the OMC filaments is rather consistent with the Jeans length, implying that the region is thermal dominant. These facts also strengthen the scenario that in the OMC-2/3 region turbulence is dissipated in the size scale of less than a few thousand astronomical units, where individual star formation has taken place. We should also consider another effect; the magnetic field. Star formation activities are actually confirmed in the FIR 3, 4, and 5 regions (e.g., Furlan et al. 2016), which indicates that the magnetic field may not be strong enough to suppress the star formation. Note that we do not have direct measurements of the magnetic field

in the observed size scale here; hence, it is difficult to discuss the effects of the magnetic field in detail. Another factor in a full virial analysis that is not included here is the external pressure from the material surrounding the FraSCO sources, which can help bind them, including turbulent pressure (e.g., Pattle et al. 2015) and cloud weight pressure (e.g., Lada et al. 2008; Kirk et al. 2017). Estimates of these pressures are not available for FraSCO sources; however, we expect the latter pressure to be the more significant factor, since turbulence appears to be largely dissipated around FraSCO sources as mentioned above.

Figure 6 shows that the majority ( $\sim 80\%$ ) of the previously identified sources, denoted by triangles, have  $\text{H}_2$  gas number densities above the Jeans critical number density regardless of whether they are pre- or protostellar sources, while three sources (FraSCO-23, FraSCO-45, and FraSCO-51, also known as MIR 23, HOPS-369/MIR 27, and a Spitzer disk source) have  $\text{H}_2$  gas number densities below the threshold. Among these three sources, FraSCO-23 and FraSCO-51 are associated with Class II sources, while FraSCO-45 is known to be a flat spectrum source, HOPS-369 (Furlan et al. 2016), which is considered to be between the Class I and Class II evolutionary stages. Therefore, these three sources are considered to be relatively evolved and the dust emission originating from the core and envelope are mostly dissipated.

In addition, Figure 6 shows that a low percentage of newly identified sources ( $\sim 14\%$ ) have  $\text{H}_2$  gas number densities above the Jeans critical number density (i.e., the sources are considered to be gravitationally bound). Among them, two continuum sources are associated with two outflows newly detected in this study, flow-5 and flow-7 (see Section 3.2.1). The rest of the newly identified sources, about 86%, have  $\text{H}_2$  gas number densities below the critical density and are considered to be gravitationally unbound. A majority of the sources newly detected in this study show sizes comparable or smaller than the best angular resolution previously achieved



**Table 7**

Dust Mass of the Identified Sources for  $T_{\text{dust}} = 15$  K ( $M_{\text{dust}}$ ) and the Mean Molecular Hydrogen Number Density ( $n_{\text{H}_2}$ , Gas-to-dust Mass Ratio of 100:1):

| Source Name | Radius (au) | $M_{\text{dust}} (M_{\odot})$ (15 K) | $n_{\text{H}_2} (\text{cm}^{-3})$ (15 K) |
|-------------|-------------|--------------------------------------|--|
| FraSCO-1    | 143         | 3.8E-05                              | 4.7E+07                                  |
| FraSCO-2    | 319         | 2.4E-04                              | 2.6E+07                                  |
| FraSCO-3    | 228         | 8.5E-05                              | 2.6E+07                                  |
| FraSCO-4    | 281         | 6.3E-04                              | 1.0E+08                                  |
| FraSCO-5    | 390         | 3.0E-04                              | 1.9E+07                                  |
| FraSCO-6    | 398         | 1.6E-03                              | 9.0E+07                                  |
| FraSCO-7    | 355         | 9.8E-04                              | 7.9E+07                                  |
| FraSCO-8    | 218         | 3.6E-04                              | 1.2E+08                                  |
| FraSCO-9    | 447         | 1.3E-03                              | 5.1E+07                                  |
| FraSCO-10   | 240         | 3.2E-04                              | 8.3E+07                                  |
| FraSCO-11   | 146         | 4.1E-05                              | 4.8E+07                                  |
| FraSCO-12   | 237         | 3.0E-04                              | 8.2E+07                                  |
| FraSCO-13   | 153         | 5.7E-05                              | 5.7E+07                                  |
| FraSCO-14   | 194         | 2.6E-04                              | 1.3E+08                                  |
| FraSCO-15   | 187         | 3.0E-04                              | 1.7E+08                                  |
| FraSCO-16   | 499         | 1.1E-02                              | 3.3E+08                                  |
| FraSCO-17   | 150         | 3.9E-05                              | 4.2E+07                                  |
| FraSCO-18   | 309         | 1.6E-04                              | 1.9E+07                                  |
| FraSCO-19   | 158         | 9.6E-05                              | 8.8E+07                                  |
| FraSCO-20   | 239         | 1.3E-04                              | 3.4E+07                                  |
| FraSCO-21   | 249         | 2.0E-04                              | 4.6E+07                                  |
| FraSCO-22   | 257         | 1.7E-04                              | 3.6E+07                                  |
| FraSCO-23   | 195         | 9.3E-05                              | 4.5E+07                                  |
| FraSCO-24   | 215         | 1.3E-04                              | 4.8E+07                                  |
| FraSCO-25   | 434         | 4.2E-04                              | 1.9E+07                                  |
| FraSCO-26   | 488         | 7.2E-04                              | 2.2E+07                                  |
| FraSCO-27   | 208         | 1.9E-04                              | 7.8E+07                                  |
| FraSCO-28   | 801         | 1.9E-03                              | 1.3E+07                                  |
| FraSCO-29   | 252         | 1.3E-04                              | 2.9E+07                                  |
| FraSCO-30   | 341         | 5.5E-04                              | 5.0E+07                                  |
| FraSCO-31   | 244         | 1.0E-04                              | 2.6E+07                                  |
| FraSCO-32   | 280         | 8.0E-04                              | 1.3E+08                                  |
| FraSCO-33   | 308         | 6.5E-04                              | 8.0E+07                                  |
| FraSCO-34   | 447         | 7.9E-04                              | 3.2E+07                                  |
| FraSCO-35   | 982         | 2.6E-03                              | 1.0E+07                                  |
| FraSCO-36   | 169         | 1.3E-04                              | 9.7E+07                                  |
| FraSCO-37   | 313         | 1.0E-03                              | 1.2E+08                                  |
| FraSCO-38   | 571         | 2.3E-03                              | 4.5E+07                                  |
| FraSCO-39   | 279         | 5.6E-04                              | 9.3E+07                                  |
| FraSCO-40   | 514         | 2.8E-03                              | 7.6E+07                                  |
| FraSCO-41   | 358         | 5.7E-04                              | 4.5E+07                                  |
| FraSCO-42   | 170         | 5.0E-05                              | 3.6E+07                                  |
| FraSCO-43   | 251         | 3.2E-04                              | 7.2E+07                                  |
| FraSCO-44   | 338         | 5.7E-04                              | 5.3E+07                                  |
| FraSCO-45   | 264         | 3.0E-04                              | 5.9E+07                                  |
| FraSCO-46   | 384         | 7.4E-04                              | 4.7E+07                                  |
| FraSCO-47   | 483         | 1.1E-03                              | 3.6E+07                                  |
| FraSCO-48   | 259         | 1.1E-04                              | 2.3E+07                                  |
| FraSCO-49   | 512         | 3.8E-03                              | 1.0E+08                                  |
| FraSCO-50   | 909         | 1.3E-03                              | 6.4E+06                                  |
| FraSCO-51   | 176         | 5.5E-05                              | 3.6E+07                                  |

**Note.** The radius (astronomical units) here was calculated from the radius (arcsec) in Table 5 with  $d = 400$  pc.

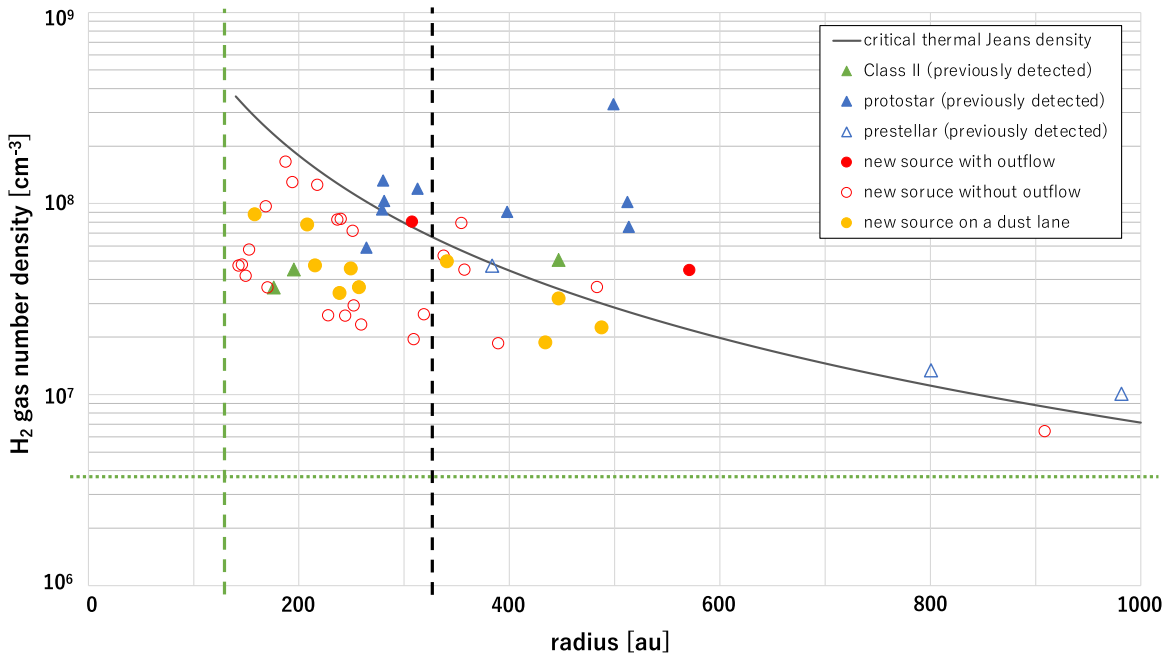
with the ALMA mosaic mapping studies in this region (i.e.,  $\theta \sim 0''.8$  by van Terwisga et al. 2019). Note that 10 of the newly identified sources with number densities below the Jeans critical number density may be on a dust lane heated by outflow driven by HOPS-370, flow-3, denoted by yellow-filled circles in Figure 6 (further explanation in Section 4.1.1). This means

that the origin of dust concentrations may not be dominated by thermal fragmentation, but rather is affected by outflow shocks. Excluding these 10 sources, the percentage of newly detected sources that are gravitationally unbound is reduced to 80%. Finally, we found that gravitationally unbound sources are located more or less uniformly across the region. In the Jeans analysis, no clear trend in terms of the core nature and evolutionary stage was found among the FIR 3, 4, and 5 regions.

### 3.2. CO( $J = 2-1$ ) and SiO( $J = 5-4$ ) Line Emissions

Outflows are a significant part of the star formation process. Outflows are important for efficiently transporting angular momentum from pre- and protostellar cores as part of the process of cores evolving to stars (Arce et al. 2007; Machida et al. 2007, 2008). Outflow gas can be traced by CO line emissions on the protostellar scale of  $\sim 0.01-0.1$  pc (Snell et al. 1980; Bachiller 1996; Bontemps et al. 1996). Interactions between outflows and surrounding gas are often observed with shocked gas tracers such as SiO line emissions. SiO in the gas phase is believed to be formed through sputtering dust grains (Ziurys et al. 1989; Caselli et al. 1997) and SiO emission is considered to be a tracer of collimated high-velocity outflows (Zhang et al. 2002; Zapata et al. 2006; Hirano et al. 2010; Matsushita et al. 2019; Liu et al. 2021). SiO emission is also considered to be an extended bow shock from protostellar outflow (Gueth et al. 1998; Shimajiri et al. 2008).

Figure 7 shows the integrated intensity maps obtained from the CO( $J = 2-1$ ) (left panel) and SiO( $J = 5-4$ ) (right panel) data sets. The images indicate that the gas distributions traced by CO and SiO are very different. The CO emission traces extended structures, while the SiO emission traces compact structures. The CO( $J = 2-1$ ) emission traces the molecular outflows well, and their spatial and velocity distributions are consistent with previous CO studies (Takahashi et al. 2008; González-García et al. 2016; Tanabe et al. 2019; Tobin et al. 2019; Feddersen et al. 2020). Our CO observations achieved 8 times higher angular resolution compared to recent interferometric CO observations (e.g., Feddersen et al. 2020). We successfully resolved internal structures toward previously reported molecular outflows. The SiO( $J = 5-4$ ) emission was intensely detected toward the FIR 4 region. While the strongest SiO component detected in the FIR 4 region was previously reported in the lower transition of the SiO( $J = 2-1$ ) observations (Shimajiri et al. 2008), our observations detected some additional SiO components. Extended and relatively strong components are located around the FIR 4 region, and several compact SiO components likely originated from the local shocked regions. Individual structures traced by CO( $J = 2-1$ ) and SiO( $J = 5-4$ ) emissions are described in the following subsections. In Section 3.2.1, we focus on identifying molecular outflows using the CO( $J=2-1$ ) image. In Section 3.2.2, we identify shocked regions (i.e., shocked gas not directly produced from outflow or jet components). The identification of the shocked regions was based on the SiO ( $J = 5-4$ ) image. Note that we adopted a systemic velocity ( $v_{\text{sys}}$ ) of  $11 \text{ km s}^{-1}$  in our observational mapping regions based on multiple line survey observations toward the FIR 4 region (López-Sepulcre et al. 2013; Tobin et al. 2019).



**Figure 6.**  $\text{H}_2$  gas number density for  $T_{\text{dust}} = 15$  K vs. source radius. Both parameters are estimated from our ALMA 12 m array 1.3 mm continuum emission following the method described in Sections 3.1.2 and 3.1.3. The different data point symbols indicate the category of the source. Triangles indicate 1.3 mm continuum sources associated with previously identified sources. Protostars denoted by blue-filled triangles represent 1.3 mm continuum sources associated with previously identified Class 0, Class I, and Class flat sources, while pre-main-sequence sources denoted by green-filled triangles are 1.3 mm continuum sources associated with previously identified Class II sources (Davis et al. 2010; Megeath et al. 2012; Furlan et al. 2016). Prestellar sources are denoted by open blue triangles are 1.3 mm continuum sources associated with 3 mm sources not identified at infrared wavelengths (Kainulainen et al. 2017; van Terwisga et al. 2019). Circles represent 1.3 mm continuum sources identified for the first time in this study. Red-filled circles indicate 1.3 mm continuum sources considered to be outflow driving sources, while open red circles indicate sources not considered to drive outflows. Yellow-filled circles indicate 1.3 mm continuum sources detected on the dust lane discussed in Section 4.1.1. The black solid curve represents the critical thermal Jeans density for 15 K. The radius for the Jeans density is defined as  $\lambda_{\text{frag}}/2$ . The green- and black-dashed lines represent half of the minor axes of the synthesized beam sizes achieved from our 1.3 mm continuum ( $\theta \sim 0''.33 \sim 130$  au) and 3 mm continuum ( $\theta \sim 0''.8 \sim 320$  au; van Terwisga et al. 2019). The lower threshold of the  $\text{H}_2$  gas number density calculated from the  $3\sigma$  mass limit is  $3.7 \times 10^6 \text{ cm}^{-3}$  for our study (the green-dotted line), while the threshold in van Terwisga et al. (2019) is  $1.9 \times 10^8 \text{ cm}^{-3}$ .

### 3.2.1. Outflow Identifications

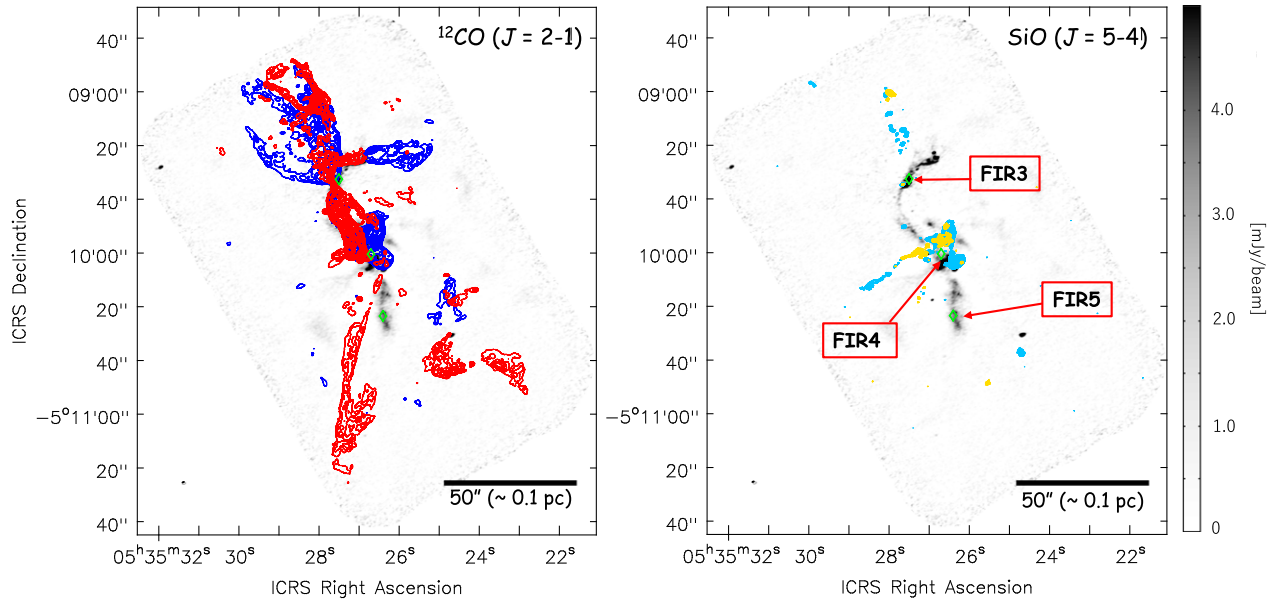
To identify the molecular outflow, we set the following five criteria: (1) CO emission is detected at greater than  $10\sigma$  in the integrated intensity map (where the velocity range of the integrated intensity map is optimized for individual regions),<sup>11</sup> (2) the extension of the CO emission is larger than the beam size, (3) the CO emission has a collimated structure, (4) the gas velocity of the CO emission is greater than  $5 \text{ km s}^{-1}$  with respect to the systemic velocity, and (5) the driving source candidate is identified from the 1.3 mm sources listed in our FraSCO catalog or sources previously cataloged in other studies.

We then identified molecular outflow for which the CO emission satisfies the five criteria. We also categorized the identified outflows into three groups, “clear,” “probable,” and “marginal” (C, P, and M in Table 8), to indicate the confidence level of the outflow detection. The categorization criteria are as follows. Clear: emissions have both localized blue- and redshifted lobes with clear bipolarity in the  $\text{CO}(J = 2-1)$  integrated intensity map. Probable: emissions show a monopolar structure of either a localized blue- or redshifted lobe in

the  $\text{CO}(J = 2-1)$  integrated intensity maps. Marginal: emissions have either blue- or redshifted components associated with a candidate driving source. However, it is hard to completely identify the molecular outflow separate from the ambient gas, due to contamination from the extended gas around the systemic velocity.

Based on the criteria, we have identified 12 CO molecular outflows as summarized in Figure 8. Zoomed-in images are presented in Figures 9–15. Of the 12 CO molecular outflows, we have newly identified six in the CO emission: flow-4, -5, -7, -8, -9, and -10. Table 8 summarizes the outflow identifications and includes the names of the identified outflows, candidate driving sources, and comparisons with previous multiwavelength studies, specifically the CO, SiO,  $2.12 \mu\text{m}$ ,  $v = 1-0$   $s(1)$   $\text{H}_2$  line emission, and centimeter continuum emission (Yu et al. 1997; Reipurth et al. 1999; Stanke et al. 2002; Shimajiri et al. 2008; Takahashi et al. 2008; González-García et al. 2016; Osorio et al. 2017; Tanabe et al. 2019; Tobin et al. 2019; Feddersen et al. 2020; Habel et al. 2021; Kang et al. 2021; Matsushita et al. 2021). The outflow detection rate with respect to the FraSCO sources is estimated to be 24%. Outflow properties such as the outflow P.A. and size, the maximum gas velocity, and the dynamical timescale for the outflow are summarized in Table 9. The P.A. of the outflow was measured from the north and is positive when the rotation is counterclockwise ( $-180^\circ$ – $180^\circ$ ). The projected outflow length,  $L_{\text{proj}}$ , was measured using the integrated intensity maps (Figures 9–15). Along the P.A.,  $L_{\text{proj}}$  was measured up to the lowest contour level presented in each figure. The projected maximum gas velocity from the outflow,

<sup>11</sup> We decided to use a  $10\sigma$  threshold instead of  $5\sigma$  to identify outflows. This threshold was decided upon after carefully checking the channel maps (i) so as not to miss any faint and high-speed outflow-related emission and at the same time (ii) to not pick up faint and extended emission originating from the molecular cloud around the systemic velocity. We confirmed that outflow identification with the thresholds as  $5\sigma$  and  $10\sigma$  does not change the number of detected outflows.



**Figure 7.** Left: CO blue- and redshifted integrated intensity maps obtained from the ALMA 12 m array. The red contours represent the integrated intensity map using the redshifted CO components in the velocity range of  $v_{\text{LSR}} = 15\text{--}95 \text{ km s}^{-1}$ . The red contour levels are  $[10, 15, 20, 25, 30, 35, 40, 45, 50, 55, 60, 65] \times 1\sigma$  ( $1\sigma = 0.17 \text{ Jy beam}^{-1} \text{ km s}^{-1}$ ). The blue contours represent the integrated intensity map using the blueshifted CO components in the velocity range of  $v_{\text{LSR}} = -100$  to  $10 \text{ km s}^{-1}$ . The blue contour levels are  $[10, 15, 20, 25, 30, 35, 40, 45, 50, 55, 60, 65, 70, 75, 80] \times 1\sigma$  ( $1\sigma = 0.23 \text{ Jy beam}^{-1} \text{ km s}^{-1}$ ). Right: SiO blue- and redshifted integrated intensity map obtained from the ALMA 12 m array. The yellow contours represent the integrated intensity map using the redshifted SiO components in the velocity range of  $v_{\text{LSR}} = 12\text{--}29 \text{ km s}^{-1}$ . The yellow contour levels are  $[10, 15, 20, 25, 30, 35, 40, 45, 50, 55] \times 1\sigma$  ( $1\sigma = 0.015 \text{ Jy beam}^{-1} \text{ km s}^{-1}$ ). The cyan contours represent the integrated intensity map using the blueshifted SiO components in the velocity range of  $v_{\text{LSR}} = -30$  to  $11 \text{ km s}^{-1}$ . The cyan contour levels are  $[10, 15, 20, 25, 30, 35, 40, 45, 50, 55, 60, 70, 80, 90, 100, 120, 140, 160, 180, 200] \times 1\sigma$  ( $1\sigma = 0.02 \text{ Jy beam}^{-1} \text{ km s}^{-1}$ ). In both panels, the grayscale represents our 1.3 mm continuum image obtained from the ALMA 12 m array. The green diamonds denote the locations of FIR 3, 4, and 5 identified by single-dish 1.3 mm continuum observations (Chini et al. 1997). The synthesized beam sizes of the CO, SiO, and 1.3 mm continuum emission are  $1''.19 \times 0''.74$ ,  $1''.26 \times 0''.79$ , and  $1''.13 \times 0''.65$ , respectively. The black ellipse at the bottom-left corner represents the largest synthesized beam sizes among them, i.e., SiO.

**Table 8**  
Outflow Properties

| Name    | Identification |                | Driving Source Candidate |            | Counterpart |     |                |            |
|---------|----------------|----------------|--------------------------|------------|-------------|-----|----------------|------------|
|         | CO             | SiO            | HOPS <sup>a</sup>        | FraSCO     | CO          | SiO | H <sub>2</sub> | 3 cm, 5 cm |
| Flow-1  | P              | M              | HOPS-350                 | ...        | ✓           |     | ✓              |            |
| Flow-2  | C              | ...            | HOPS-66A/B               | FraSCO-4/6 | ✓           |     | ✓              |            |
| Flow-3  | C              | C <sup>b</sup> | HOPS-370                 | FraSCO-16  | ✓           |     | ✓              | ✓          |
| Flow-4  | P              | ...            | HOPS-64                  | FraSCO-32  |             |     | ✓              | ✓          |
| Flow-5  | P              | P              | ...                      | FraSCO-33  |             |     |                |            |
| Flow-6  | P              | P              | HOPS-108                 | FraSCO-37  | ✓           |     |                | ✓          |
| Flow-7  | M              | ...            | ...                      | FraSCO-38  |             |     |                |            |
| Flow-8  | C              | M              | ...                      | FraSCO-39  |             |     | ✓              |            |
| Flow-9  | P              | P              | ...                      | FraSCO-40  |             | ✓   |                | ✓          |
| Flow-10 | C              | ...            | HOPS-369                 | FraSCO-45  |             |     | ✓              |            |
| Flow-11 | C              | M              | HOPS-368                 | FraSCO-49  | ✓           |     | ✓              | ✓          |
| Flow-12 | C              | ...            | HOPS-60                  | ...        | ✓           |     | ✓              |            |

**Notes.** In the identification columns, C, P, and M indicate structures identified as clear, probable, and marginal, respectively. A check mark indicates that the corresponding line/continuum emission has been detected in previous works.

<sup>a</sup> Infrared source (Megeath et al. 2012; Furlan et al. 2016).

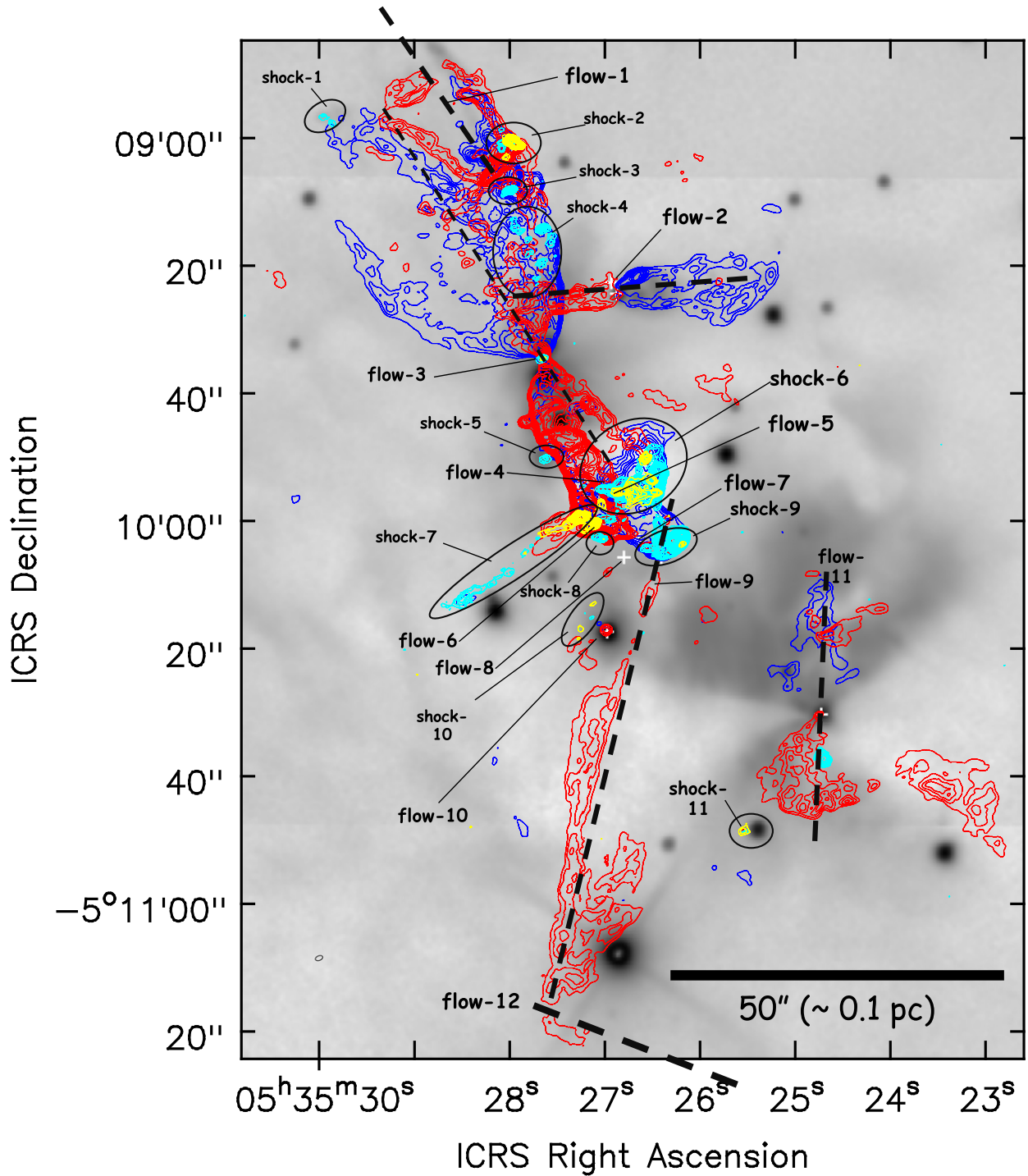
<sup>b</sup> The compact SiO emission is elongated perpendicular to the CO outflow axis.

$v_{\text{max,proj}}$ , is taken from the difference between the absolute value of the maximum LSR velocity and  $v_{\text{sys}}$ . The maximum LSR velocity was determined based on the CO channel maps (see Appendix B) where the outflow emission is greater than  $4\sigma$ . The projection uncorrected outflow dynamical timescale,  $t_{\text{dyn,proj}}$ , is estimated from  $L_{\text{proj}}/v_{\text{max,proj}}$ . The projection corrected outflow dynamical timescale,  $t_{\text{dyn,corr}}$ , is estimated from  $(L_{\text{proj}}/\cos\theta)/(v_{\text{max,proj}}/\sin\theta)$ . Here,  $\theta = 30^\circ$  was adopted as a representative inclination angle of the outflow. This inclination angle was taken from a recent study by Tobin et al. (2020) measuring the disk

inclination angle peaking at  $\sim 60^\circ$  ( $30^\circ$  in terms of the outflow inclination defined here). Note that there is no clear correlation between the elongation of the dust filamentary structures and the P.A. of the detected outflows. Below, we present detailed results of the identified individual outflows.

*Flow-1* (probable; Figure 9(a)): a blue- and redshifted cavity-like structure colliding with flow-2 blueshifted emission, observed around R.A. =  $05^{\text{h}}35^{\text{m}}28^{\text{s}}.535$ , decl. =  $-05^\circ08'57''.687$ . The emission was detected in the LSR velocity range of  $0\text{--}30 \text{ km s}^{-1}$ . Due to the limited observed imaging area, our image appears to

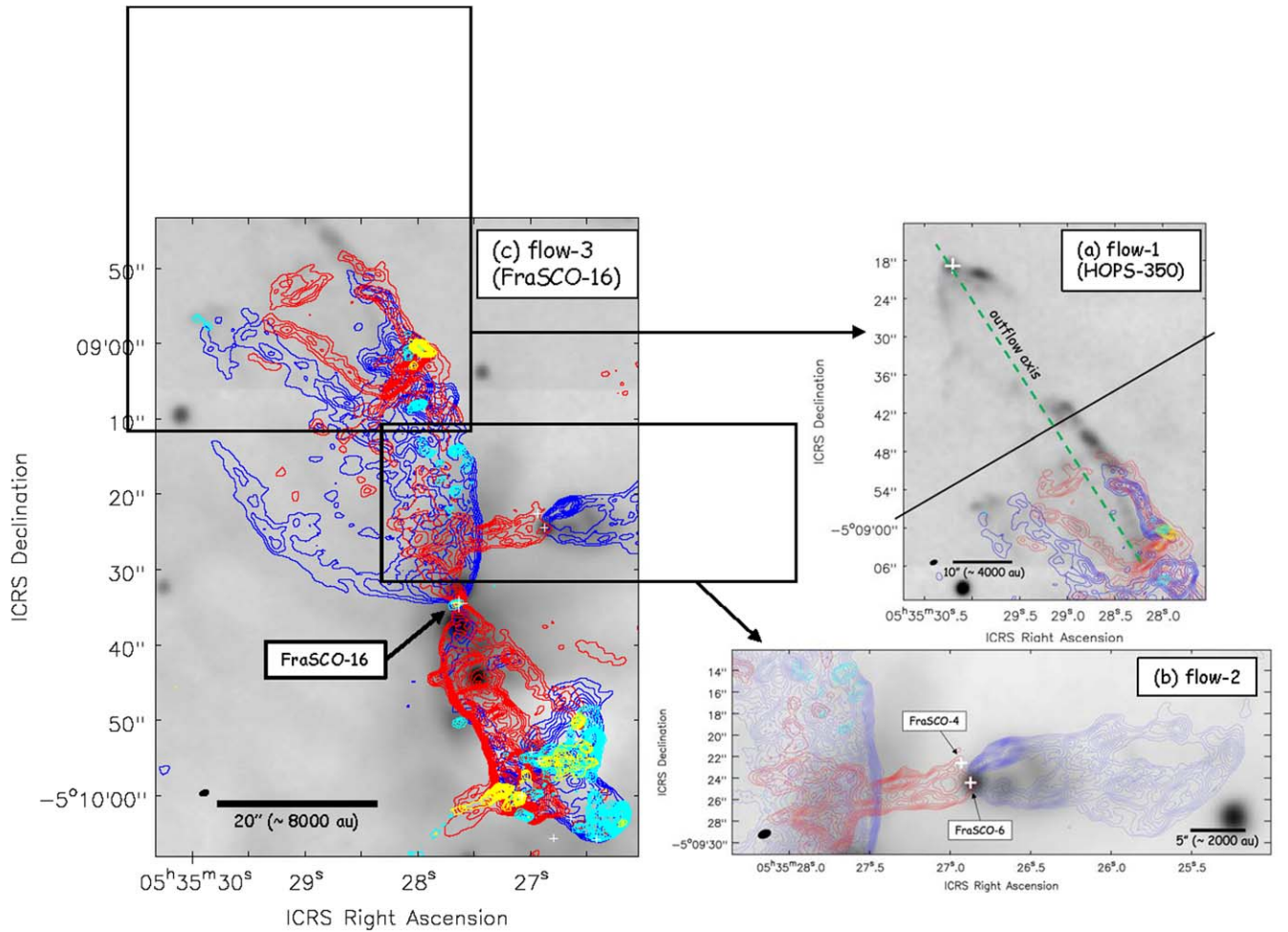




**Figure 8.** Identification of CO outflows and SiO-shocked structures, summarized in Tables 8 and 10, respectively. The white crosses correspond to the locations of outflow driving 1.3 mm continuum sources identified in Section 3.1.1 using dendrograms (see Table 5), although the driving sources of flow-1 and flow-12 are outside our observation mapping image. The red, blue, yellow, and cyan contours are the same as those in Figure 7. The gray background images show the  $2.2 \mu\text{m}$   $K_s$  band image obtained from SIRIUS/IRSF (Takahashi et al. 2008). Some expected outflow axes are represented by the black-dashed lines. Note that flow-12 is not visible here because the integrated intensity map is not optimized for the velocity range of this outflow. The image of flow-12 with an optimized velocity range can be found in Figure 15. The black open ellipse at the bottom-left corner denotes the synthesized beam size of SiO (same as that in Figure 7).

only cover half of the lobe extending in the southwest direction with respect to the candidate driving source. After checking previous wide-field observations (Stanke et al. 2002), we find that the outflow is most likely driven by CRW FIR 3 (also known as HOPS-350). Further evidence of mass ejection phenomena was

reported from previous  $\text{H}_2$  line ( $2.12 \mu\text{m}$ ,  $v = 1-0$  s(1)) observations by Stanke et al. (2002). Their  $\text{H}_2$  line image shows an S-shaped structure, which is also seen in the  $K_s$  image presented in Figure 9. The detected CO cavity-like structure spatially correlates well with a part of the S-shaped structure. Assuming that



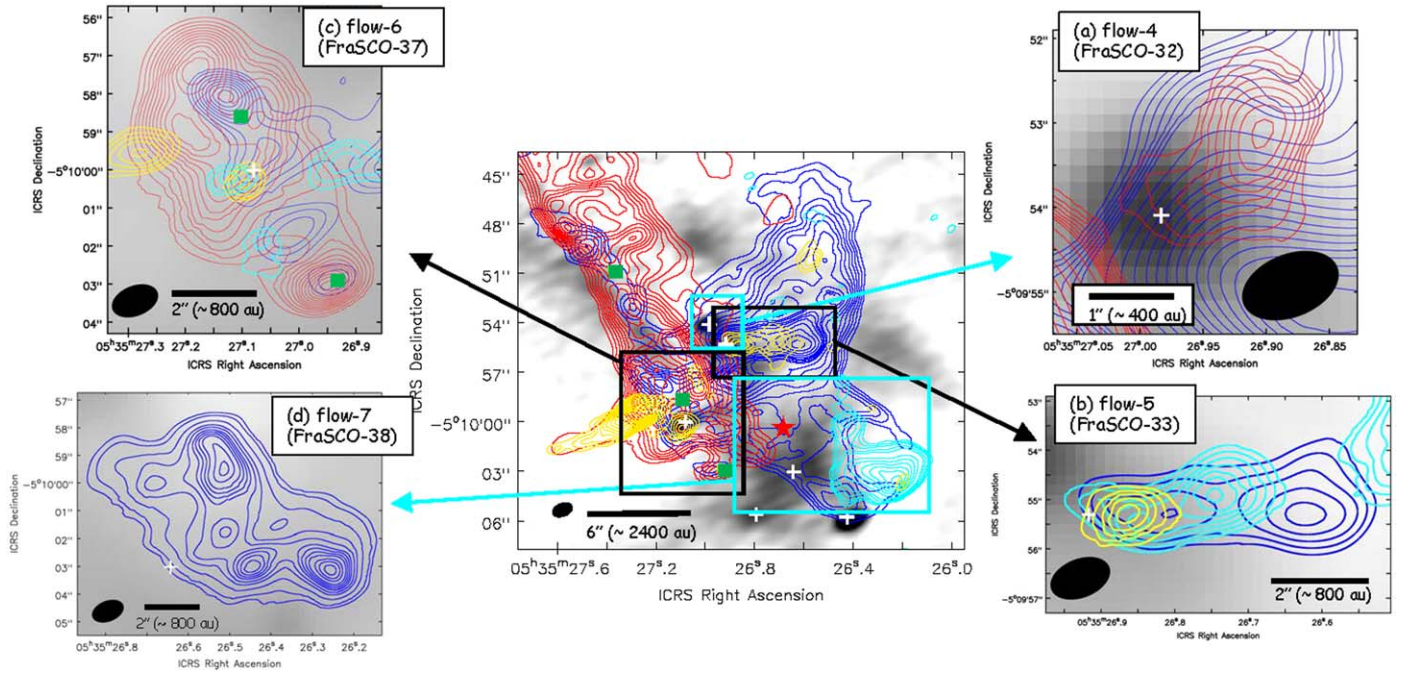
**Figure 9.** Flow-1–flow-3. The red, blue, yellow, and cyan contours represent the integrated intensities obtained from the ALMA 12 m array of redshifted CO, blueshifted CO, redshifted SiO, and blueshifted SiO line emissions, respectively. The gray background images show the  $2.2\ \mu\text{m}$   $K_s$  band image obtained from SIRIUS/IRSF (Takahashi et al. 2008). The white crosses denote the positions of the outflow driving sources in all the figures. The black ellipse at the bottom-left corner is the same as that in Figure 7. (a) flow-1 (probable). The red contour levels are  $[20, 30, 40, 50, 60, 70, 80, 90, 100, 110, 120, 130, 140] \times 1\sigma$  ( $1\sigma = 0.08\ \text{Jy beam}^{-1}\ \text{km s}^{-1}$ ,  $v_{\text{LSR}} = 12\text{--}30\ \text{km s}^{-1}$ ). The blue contour levels are  $[20, 30, 40, 50, 60, 70, 80, 90, 100] \times 1\sigma$  ( $1\sigma = 0.08\ \text{Jy beam}^{-1}\ \text{km s}^{-1}$ ,  $v_{\text{LSR}} = 0\text{--}11\ \text{km s}^{-1}$ ). The yellow contour levels are  $[10, 15, 20, 25, 30, 35, 40, 45, 50, 55] \times 1\sigma$  ( $1\sigma = 0.015\ \text{Jy beam}^{-1}\ \text{km s}^{-1}$ ,  $v_{\text{LSR}} = 12\text{--}30\ \text{km s}^{-1}$ ). The cyan contour levels are  $[5, 10, 15, 20] \times 1\sigma$  ( $1\sigma = 0.03\ \text{Jy beam}^{-1}\ \text{km s}^{-1}$ ,  $v_{\text{LSR}} = 0\text{--}11\ \text{km s}^{-1}$ ). The black solid line represents the boundary of our observation mapping. The green-dashed line represents the outflow axis. (b) flow-2 (clear). This outflow is considered to be driven by two sources (FraSCO-4 and FraSCO-6). The red contour levels are  $[8, 10, 12, 14, 16, 18, 20, 22, 24, 26, 28, 30, 32, 34, 36, 38, 40, 42, 44, 46, 48, 50, 52, 54, 56, 58, 60, 62, 64] \times 1\sigma$  ( $1\sigma = 0.2\ \text{Jy beam}^{-1}\ \text{km s}^{-1}$ ,  $v_{\text{LSR}} = 15\text{--}35\ \text{km s}^{-1}$ ). The blue contour levels are  $[8, 11, 14, 17, 20, 23, 26, 29, 32, 35, 38, 41, 44, 47, 50] \times 1\sigma$  ( $1\sigma = 0.2\ \text{Jy beam}^{-1}\ \text{km s}^{-1}$ ,  $v_{\text{LSR}} = -70\ \text{to}\ 10\ \text{km s}^{-1}$ ). The cyan contour levels are  $[4, 5, 6, 8, 10, 12, 16, 20] \times 1\sigma$  ( $1\sigma = 0.07\ \text{Jy beam}^{-1}\ \text{km s}^{-1}$ ,  $v_{\text{LSR}} = -30\ \text{to}\ 11\ \text{km s}^{-1}$ ). (c) flow-3 (clear). The driven source candidates are considered to be FraSCO-16. The red contour levels are  $[10, 15, 20, 25, 30, 35, 40, 45, 50, 55, 60, 65] \times 1\sigma$  ( $1\sigma = 0.17\ \text{Jy beam}^{-1}\ \text{km s}^{-1}$ ,  $v_{\text{LSR}} = 12\text{--}85\ \text{km s}^{-1}$ ). The blue contour levels are  $[10, 15, 20, 25, 30, 35, 40, 45, 50, 55, 60, 65, 70, 75, 80] \times 1\sigma$  ( $1\sigma = 0.23\ \text{Jy beam}^{-1}\ \text{km s}^{-1}$ ,  $v_{\text{LSR}} = -40\ \text{to}\ 11\ \text{km s}^{-1}$ ). The yellow contour levels are  $[10, 15, 20, 25, 30, 35, 40, 45, 50, 55, 60, 70, 80, 90, 100, 120, 140, 160, 180, 200] \times 1\sigma$  ( $1\sigma = 0.015\ \text{Jy beam}^{-1}\ \text{km s}^{-1}$ ,  $v_{\text{LSR}} = -30\ \text{to}\ 11\ \text{km s}^{-1}$ ). The cyan contour levels are  $[10, 15, 20, 25, 30, 35, 40, 45, 50, 55, 60, 70, 80, 90, 100, 120, 140, 160, 180, 200] \times 1\sigma$  ( $1\sigma = 0.02\ \text{Jy beam}^{-1}\ \text{km s}^{-1}$ ,  $v_{\text{LSR}} = 12\text{--}30\ \text{km s}^{-1}$ ).

the CO outflow is driven by HOPS-350, the projected outflow length of the southwest lobe is  $\sim 58''$  ( $\sim 23,200\ \text{au}$ ).

*Flow-2* (clear; Figure 9(b)): flow-2 is driven by a binary system consisting of FraSCO-4 and FraSCO-6 (also known as HOPS-66B and HOPS-66A). The identified outflow elongates along the east–west direction. The CO blueshifted emission extends to  $\sim 26''$  ( $\sim 10,400\ \text{au}$ ) and the redshifted emission extends to  $\sim 19''$  ( $\sim 7600\ \text{au}$ ). The CO emission is detected in the LSR velocity with a range of  $-70\text{--}35\ \text{km s}^{-1}$ . The redshifted component elongated in the east direction clearly shows the emission driven from both FraSCO sources (channel maps at  $v_{\text{LSR}} = 20, 25,$  and  $30\ \text{km s}^{-1}$  in the online journal). This component collides and penetrates through a

blueshifted outflow originating from another outflow, flow-3, located  $\sim 10''$  east of the binary system. The blueshifted emission elongated to the west seems to be mainly driven by FraSCO-6 (i.e., the southern component of the binary system). The blueshifted component shows complicated internal structures such as blobs and wiggly structures within the lobe. Episodic mass ejection is suggested in the western lobe where the blueshifted CO emission is located (Habel et al. 2021).

*Flow-3* (clear; Figure 9(c)): flow-3 is driven by a bright 1.3 mm source, FraSCO-16 (also known as HOPS-370). The CO outflow is elongated to the northeast and southwest direction. The CO emission is detected in the LSR velocity



**Figure 10.** Flow-4–flow-7. The red, blue, yellow, and cyan contours represent the integrated intensities obtained from the ALMA 12 m array of redshifted CO, blueshifted CO, redshifted SiO, and blueshifted SiO, respectively. The white crosses denote the positions of the outflow driving sources in all the figures. The green squares denote the positions of nonthermal radio knots detected by 5 cm continuum emission (Osorio et al. 2017). Central panel: zoomed-out image around the position of FIR 4 (red star, Chini et al. 1997). The gray background image represents our 1.3 mm continuum image. The red contour levels are  $[10, 20, 30, 40, 50, 60, 70, 80, 90, 100, 110] \times 1\sigma$  ( $1\sigma = 0.1 \text{ Jy beam}^{-1} \text{ km s}^{-1}$ ,  $v_{\text{LSR}} = 15\text{--}22 \text{ km s}^{-1}$ ). The blue contour levels are  $[10, 15, 20, 25, 30, 35, 40, 45, 50, 52, 55, 57, 60, 65, 70, 75, 80] \times 1\sigma$  ( $1\sigma = 0.2 \text{ Jy beam}^{-1} \text{ km s}^{-1}$ ,  $v_{\text{LSR}} = 2\text{--}9 \text{ km s}^{-1}$ ). The yellow contour levels are  $[3, 4, 5, 6, 7, 8, 9, 10, 11, 12, 13, 14, 15] \times 1\sigma$  ( $1\sigma = 0.04 \text{ Jy beam}^{-1} \text{ km s}^{-1}$ ,  $v_{\text{LSR}} = 15\text{--}20 \text{ km s}^{-1}$ ). The cyan contour levels are  $[3, 4, 5, 7, 9, 15, 20, 25, 30, 35, 40] \times 1\sigma$  ( $1\sigma = 0.04 \text{ Jy beam}^{-1} \text{ km s}^{-1}$ ,  $v_{\text{LSR}} = 0\text{--}5 \text{ km s}^{-1}$ ). Figures 10(a)–(d) are zoomed-in images overlaid on the  $2.2 \mu\text{m}$  *Ks* band image obtained from SIRIUS/IRSF (gray background image; Takahashi et al. 2008). (a) flow-4 (probable). The red contour levels are  $[8, 10, 12, 14, 16, 18, 20, 22, 30, 50, 70, 90, 110, 130, 150, 170, 190, 210, 230, 250] \times 1\sigma$  ( $1\sigma = 0.04 \text{ Jy beam}^{-1} \text{ km s}^{-1}$ ,  $v_{\text{LSR}} = 1\text{--}23 \text{ km s}^{-1}$ ). The blue contour levels are  $[8, 10, 12, 14, 16, 18, 20, 30, 40, 50, 60, 70, 80, 90, 100, 110, 120, 130, 140, 150, 160, 170, 180, 190, 200, 210, 220, 230, 235] \times 1\sigma$  ( $1\sigma = 0.04 \text{ Jy beam}^{-1} \text{ km s}^{-1}$ ,  $v_{\text{LSR}} = -1 \text{ to } 5 \text{ km s}^{-1}$ ). (b) flow-5 (probable). The blue contour levels are  $[60, 65, 70, 75, 80] \times 1\sigma$  ( $1\sigma = 0.2 \text{ Jy beam}^{-1} \text{ km s}^{-1}$ ,  $v_{\text{LSR}} = 2\text{--}9 \text{ km s}^{-1}$ ). The yellow contour levels are  $[4, 6, 8, 10, 12, 14] \times 1\sigma$  ( $1\sigma = 0.015 \text{ Jy beam}^{-1} \text{ km s}^{-1}$ ,  $v_{\text{LSR}} = 14\text{--}16 \text{ km s}^{-1}$ ). The cyan contour levels are  $[10, 12, 14, 16, 18, 20, 22] \times 1\sigma$  ( $1\sigma = 0.027 \text{ Jy beam}^{-1} \text{ km s}^{-1}$ ,  $v_{\text{LSR}} = 2\text{--}5 \text{ km s}^{-1}$ ). (c) flow-6 (probable). The red contour levels are  $[4, 6, 8, 10, 12, 14, 16, 18, 20, 22, 24, 26, 28] \times 1\sigma$  ( $1\sigma = 0.2 \text{ Jy beam}^{-1} \text{ km s}^{-1}$ ,  $v_{\text{LSR}} = 25\text{--}50 \text{ km s}^{-1}$ ). The blue contour levels are  $[8, 10, 12, 14, 16, 18, 20, 22, 24] \times 1\sigma$  ( $1\sigma = 0.2 \text{ Jy beam}^{-1} \text{ km s}^{-1}$ ,  $v_{\text{LSR}} = -7 \text{ to } 5 \text{ km s}^{-1}$ ). The yellow contour levels are  $[6, 7, 8, 9, 10, 11, 12, 13, 14, 15] \times 1\sigma$  ( $1\sigma = 0.04 \text{ Jy beam}^{-1} \text{ km s}^{-1}$ ,  $v_{\text{LSR}} = 12\text{--}18 \text{ km s}^{-1}$ ). The cyan contour levels are  $[6, 8, 10, 12] \times 1\sigma$  ( $1\sigma = 0.01 \text{ Jy beam}^{-1} \text{ km s}^{-1}$ ,  $v_{\text{LSR}} = 1\text{--}3 \text{ km s}^{-1}$ ). (d) flow-7 (marginal). The blue contour levels are  $[3, 5, 10, 15, 18, 21, 23, 25, 27, 30, 32, 34] \times 1\sigma$  ( $1\sigma = 0.1 \text{ Jy beam}^{-1} \text{ km s}^{-1}$ ,  $v_{\text{LSR}} = -5 \text{ to } 5 \text{ km s}^{-1}$ ). In all the figures, the black ellipses at the bottom corners are the same as that in Figure 7.

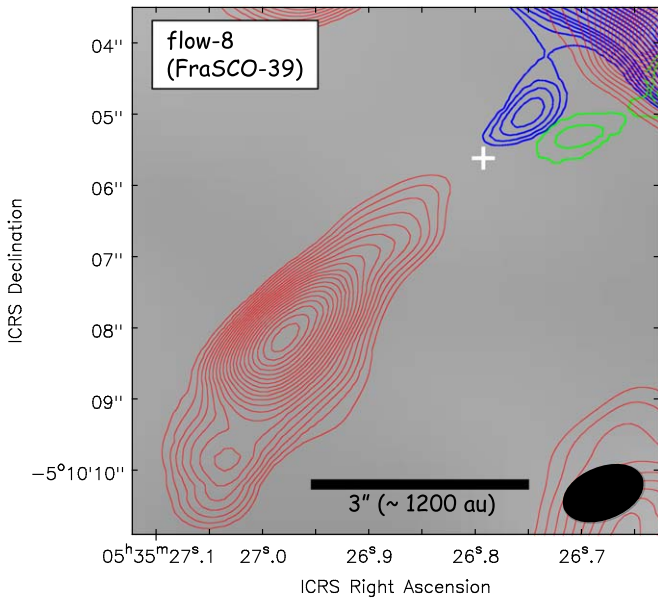
range of  $-40$  to  $85 \text{ km s}^{-1}$ . The lobes are bright in both the red- and blueshifted emissions, and hence the outflow is considered to be aligned closer to the plane of the sky. Adopting an inclination angle of  $10^\circ$  with respect to the plane of the sky, the corrected dynamical timescale is 3 times shorter than the corrected dynamical timescale for an inclination of  $30^\circ$  listed in Table 9. The northeast lobe extends to  $\sim 48''$  ( $\sim 19,200 \text{ au}$ ) and shows a U-shaped outflow lobe, which is particularly clear in the blueshifted emission, while the redshifted emission is mainly distributed in the right side of the northeast lobe. Note that the cavity-like structure from another outflow, flow-1, overlaps with this redshifted component. The lobe located in the southwest part of FraSCO-16 extends to  $\sim 37''$  ( $\sim 14,800 \text{ au}$ ) and is slightly compact compared to the other side of the lobe. In addition, the southwestern lobe appears to be more collimated than the northeast lobe. The shape of the eastern edge of the southwest lobe overlaps identified 1.3 mm continuum sources aligned within the dust filamentary structure (see Section 4.1 for a possible interpretation). The left side of the southwest lobe is bright in both the red- and blueshifted emissions, while the right side is bright mainly in the redshifted emission from the gas in the root of the outflow, and bright in the blueshifted emission at the tip of the outflow lobe. A compact SiO emission was

detected at FraSCO-16. It extends to  $\sim 3''$  ( $\sim 1200 \text{ au}$ ). The emission was detected in an LSR velocity range of  $-1$  to  $16 \text{ km s}^{-1}$ . The SiO emission is elongated perpendicular to the CO outflow axis and shows a velocity gradient across the major axis of the SiO component. This SiO emission might be not related to the CO outflow, but a rotational envelope.

*Flow-4* (probable; Figure 10(a)): this compact and elongated redshifted CO emission is likely associated with FraSCO-32 and hence we identify this as a probable candidate. The emission is distributed to the northwest direction with respect to FraSCO-32 (also known as HOPS-64). It extends to  $\sim 2''7$  ( $\sim 1080 \text{ au}$ ) and shows a velocity range of  $v_{\text{LSR}} = 18\text{--}30 \text{ km s}^{-1}$ . There is an extended blueshifted emission in this region; however, no clear collimated lobe-like structure associated with the driving source candidate was detected.

*Flow-5* (probable; Figure 10(b)): a collimated monopolar outflow associated with the compact 1.3 mm source FraSCO-33, which was detected as a millimeter source for the first time by our study. The CO emission is distributed in the west direction with respect to FraSCO-33. The outflow extends to  $\sim 6''$  ( $\sim 2400 \text{ au}$ ) and the blueshifted emission velocity reaches the LSR velocity of  $2 \text{ km s}^{-1}$ . Collimated SiO emission is detected in both the blue- and redshifted emissions. The blue-

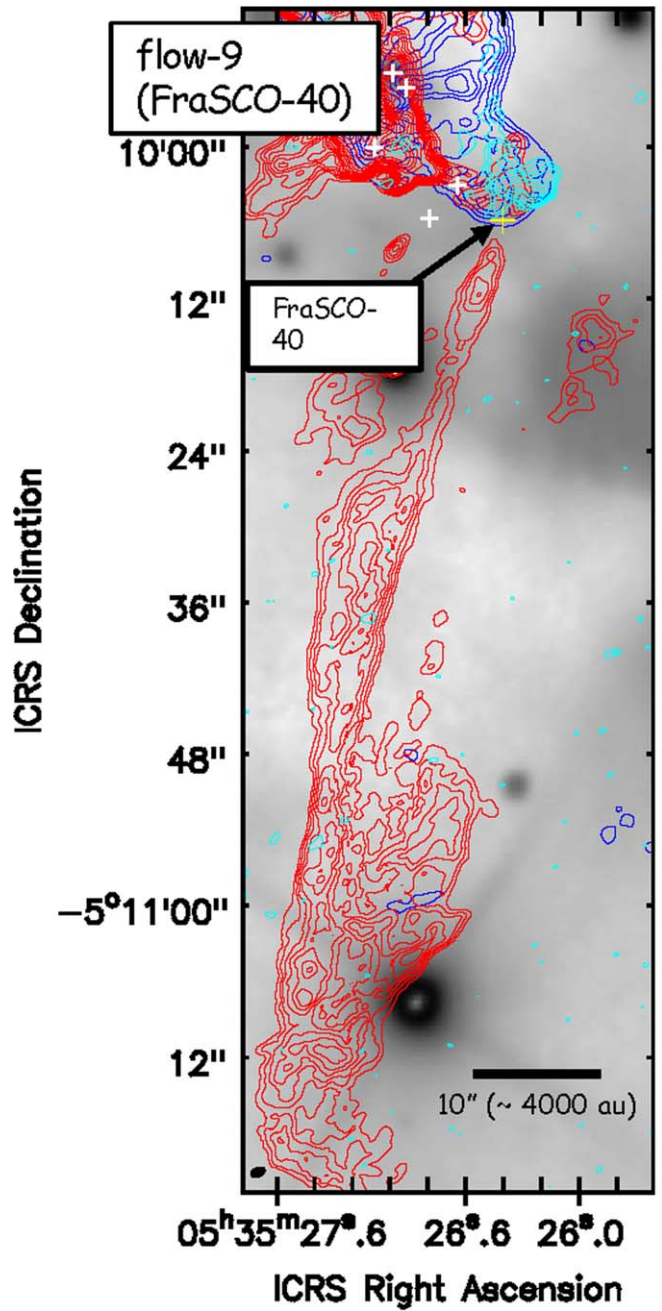




**Figure 11.** Flow-8 (clear). The gray background shows the  $2.2\ \mu\text{m}$   $K_s$  band image obtained from SIRIUS/IRSF (Takahashi et al. 2008). The white cross denoted the position of the outflow driving source (FraSCO-39). The red contours represent the integrated intensity of the redshifted CO components obtained from the ALMA 12 m array ( $v_{\text{LSR}} = 13\text{--}18\ \text{km s}^{-1}$ ). The red contour levels are  $[10, 14, 18, 22, 26, 30, 34, 38, 42, 46, 50, 54, 58, 62, 66, 70, 74, 78, 82, 86] \times 1\sigma$  ( $1\sigma = 0.02\ \text{Jy beam}^{-1}\ \text{km s}^{-1}$ ). The blue contours represent the integrated intensity of the blueshifted CO components obtained from the ALMA 12 m array ( $v_{\text{LSR}} = 7\text{--}9\ \text{km s}^{-1}$ ). The blue contour levels are  $[10, 12, 14, 16, 18, 20, 24, 28, 32, 36, 40, 44, 48, 52, 56, 60, 64, 68, 72, 76, 80, 84] \times 1\sigma$  ( $1\sigma = 0.03\ \text{Jy beam}^{-1}\ \text{km s}^{-1}$ ). The green contours represent the integrated intensity of the SiO component obtained from the ALMA 12 m array ( $v_{\text{LSR}} = 10\text{--}12\ \text{km s}^{-1}$ ). The green contour levels are  $[3, 4] \times 1\sigma$  ( $1\sigma = 0.03\ \text{Jy beam}^{-1}\ \text{km s}^{-1}$ ). The black ellipse at the bottom-right corner is the same as that in Figure 7.

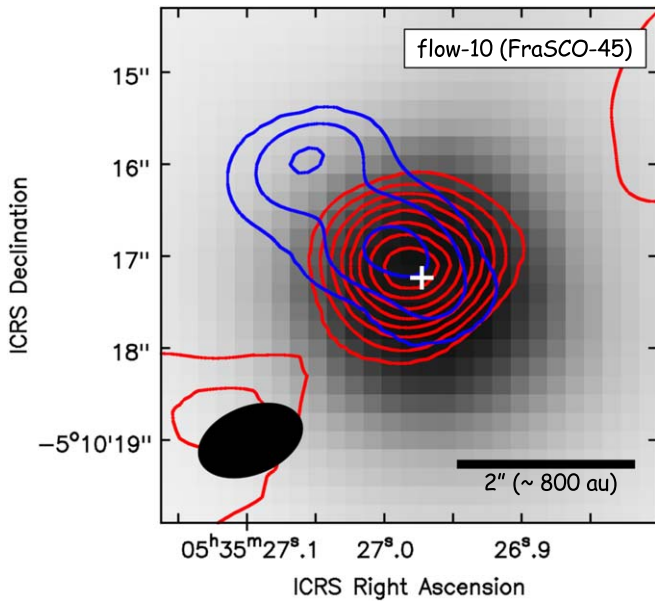
and redshifted SiO emission is elongated in the westward direction by  $\sim 3''.8$  ( $\sim 1520\ \text{au}$ ) and  $\sim 2''$  ( $\sim 800\ \text{au}$ ), respectively, with respect to FraSCO-33. The blue- and redshifted velocities reach  $v_{\text{LSR}} = 2\ \text{km s}^{-1}$  and  $v_{\text{LSR}} = 16\ \text{km s}^{-1}$ . This region is strongly affected by the shocked gas (shock-6, as discussed in Section 3.2.2), and hence it is difficult to disentangle the emission from the outflow and shocked components. However, the detected CO and SiO emissions show compact localized emission peaks associated with FraSCO-33. The first peaks associated with FraSCO-33 (Figure 10(b)) most probably originate from flow-5, while some of the more extended emissions are possibly associated with shock-originated extended gas (i.e., shock-6 as explained in Section 3.2). Therefore, we identified the emission as an outflow.

*Flow-6* (probable; Figure 10(c)): the driving source of flow-6 is considered to be FraSCO-37 (also known as HOPS-108). This region shows localized CO blue- and redshifted emissions. Although the emission peaks are not directly associated with FraSCO-37, the emission shows elongated structures in the northeast and southwest directions with a projected length of  $\sim 7''$  ( $\sim 2800\ \text{au}$ ) centered at FraSCO-37. The red- and blue-shifted emissions reach  $v_{\text{LSR}} = 50$  and  $-7\ \text{km s}^{-1}$ , respectively. A compact SiO emission, extending to  $\sim 1''.2$  ( $\sim 480\ \text{au}$ ), associated with FraSCO-37 is also detected in the LSR velocity ranges of  $1\text{--}3$  and  $12\text{--}18\ \text{km s}^{-1}$ . The spatial distribution is not consistent with the CO emission, but is perpendicular to the elongation of the CO emission. Osorio et al. (2017) detected

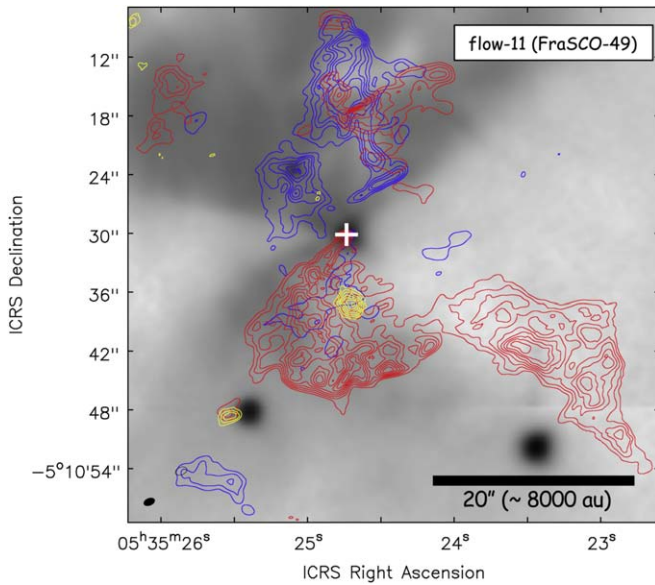


**Figure 12.** Flow-9 (probable). The gray background shows the  $2.2\ \mu\text{m}$   $K_s$  band image obtained from SIRIUS/IRSF (Takahashi et al. 2008). The white crosses and yellow cross represent the positions of outflow driving sources. The yellow cross represents the position of the outflow driving source of flow-9 (FraSCO-40). The red contours represent the integrated intensity of the redshifted CO components obtained from the ALMA 12 m array ( $v_{\text{LSR}} = 13\text{--}60\ \text{km s}^{-1}$ ). The red contour levels are  $[10, 15, 20, 25, 30, 35, 40, 45, 50, 60, 70, 80, 90, 100, 110, 120, 130, 140, 150, 160] \times 1\sigma$  ( $1\sigma = 0.1\ \text{Jy beam}^{-1}\ \text{km s}^{-1}$ ). The blue contours represent the integrated intensity of the blueshifted CO components obtained from the ALMA 12 m array ( $v_{\text{LSR}} = -5$  to  $10\ \text{km s}^{-1}$ ). The blue contour levels are  $[10, 20, 30, 40, 50, 60, 70, 80] \times 1\sigma$  ( $1\sigma = 0.2\ \text{Jy beam}^{-1}\ \text{km s}^{-1}$ ). The cyan contours represent the integrated intensity of the blueshifted SiO component obtained from the ALMA 12 m array ( $v_{\text{LSR}} = -5$  to  $5\ \text{km s}^{-1}$ ). The cyan contour levels are  $[10, 20, 30, 50, 90, 130, 170] \times 1\sigma$  ( $1\sigma = 0.005\ \text{Jy beam}^{-1}\ \text{km s}^{-1}$ ). The black ellipse at the bottom-left corner is the same as that in Figure 7.

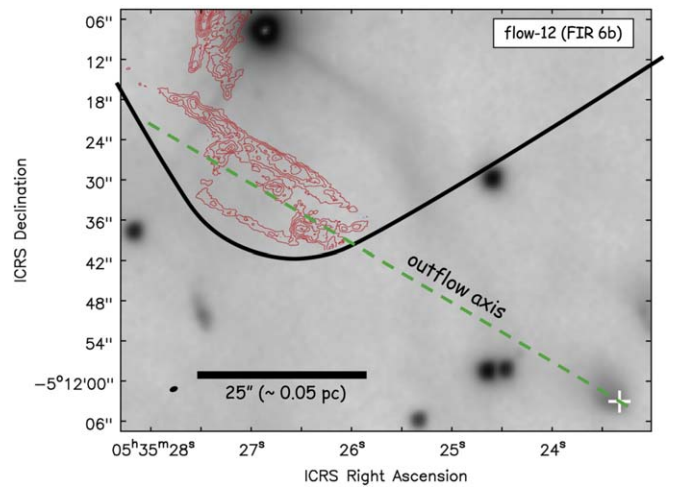
centimeter continuum emission from a nonthermal origin. They reported two emission peaks, denoted by green-filled squares in Figure 10(c), which spatially coincide with locations of one of



**Figure 13.** Flow-10 (clear). The gray background shows the  $2.2\ \mu\text{m}$   $K_s$  band image obtained from SIRIUS/IRSF (Takahashi et al. 2008). The white cross denotes the position of the outflow driving source (FraSCO-45). The red contours represent the integrated intensity of the redshifted CO components obtained from the ALMA 12 m array ( $v_{\text{LSR}} = 13\text{--}21\ \text{km s}^{-1}$ ). The red contour levels are  $[10, 15, 20, 25, 30, 35, 40, 45] \times 1\sigma$  ( $1\sigma = 0.08\ \text{Jy beam}^{-1}\ \text{km s}^{-1}$ ). The blue contours represent the integrated intensity of the blueshifted CO components obtained from the ALMA 12 m array ( $v_{\text{LSR}} = 3\text{--}7\ \text{km s}^{-1}$ ). The blue contour levels are  $[10, 15, 20] \times 1\sigma$  ( $1\sigma = 0.08\ \text{Jy beam}^{-1}\ \text{km s}^{-1}$ ). The black ellipse at the bottom-left corner is the same as that in Figure 7.



**Figure 14.** Flow-11 (clear). The gray background shows the  $2.2\ \mu\text{m}$   $K_s$  band image obtained from SIRIUS/IRSF (Takahashi et al. 2008). The white cross denotes the position of the outflow driving source (FraSCO-49). The red contours represent the integrated intensity of the redshifted CO components obtained from the ALMA 12 m array ( $v_{\text{LSR}} = 15\text{--}35\ \text{km s}^{-1}$ ). The red contour levels are  $[10, 15, 20, 25, 30, 35, 40, 45] \times 1\sigma$  ( $1\sigma = 0.1\ \text{Jy beam}^{-1}\ \text{km s}^{-1}$ ). The blue contours represent the integrated intensity of the blueshifted CO components obtained from the ALMA 12 m array ( $v_{\text{LSR}} = 0\text{--}5\ \text{km s}^{-1}$ ). The blue contour levels are  $[10, 15, 20, 25, 30, 35] \times 1\sigma$  ( $1\sigma = 0.1\ \text{Jy beam}^{-1}\ \text{km s}^{-1}$ ). The yellow contours represent the integrated intensity of the blueshifted SiO component obtained from the ALMA 12 m array ( $v_{\text{LSR}} = 15\text{--}35\ \text{km s}^{-1}$ ). The cyan contour levels are  $[4, 6, 8, 10, 12, 14, 16] \times 1\sigma$  ( $1\sigma = 0.05\ \text{Jy beam}^{-1}\ \text{km s}^{-1}$ ). The black ellipse at the bottom-left corner is the same as that in Figure 7.



**Figure 15.** Flow-12 (clear). The gray background shows the  $2.2\ \mu\text{m}$   $K_s$  band image obtained from SIRIUS/IRSF (Takahashi et al. 2008). The white cross denotes the position of the outflow driving source (FIR 6b, Matsushita et al. 2021). The red contours represent the integrated intensity of the redshifted CO components obtained from the ALMA 12 m array ( $v_{\text{LSR}} = 20\text{--}85\ \text{km s}^{-1}$ ). The red contour levels are  $[8, 12, 16, 20, 24, 28, 32, 36, 40, 44] \times 1\sigma$  ( $1\sigma = 0.05\ \text{Jy beam}^{-1}\ \text{km s}^{-1}$ ). The black solid line is the boundary of our observation mapping. The green-dashed line represents the outflow axis. The black ellipse at the bottom-left corner is the same as that in Figure 7.

the blue- (northeast) and redshifted (southwest) CO lobes identified as flow-6.

*Flow-7* (marginal; Figure 10(d)): This blueshifted emission shows a butterfly wing-like structure in the integrated intensity image. The blueshifted emission reaches  $v_{\text{LSR}} = -14\ \text{km s}^{-1}$ . The possible driving source is FraSCO-38, which was detected as a millimeter source for the first time by our study. The compact blueshifted emission is located in the most complex area. It is difficult to distinguish whether the blueshifted component is actually associated with FraSCO-38 or originates from the surrounding environment. No compact localized redshifted emission is detected around FraSCO-38.

*Flow-8* (clear; Figure 11): flow-8 is a collimated bipolar CO outflow associated with FraSCO-39 (known as VLA 16). The blue- and redshifted emissions are located in the northwest and the southeast directions with respect to FraSCO-39, extending with a projected length of  $1''.25$  ( $\sim 500\ \text{au}$ ) and  $6''.5$  ( $\sim 2600\ \text{au}$ ), respectively. The blue- and redshifted emissions are detected in the LSR velocity ranges of  $8\text{--}9$  and  $13\text{--}17\ \text{km s}^{-1}$ , respectively. A compact SiO emission was also detected just next to the CO blueshifted emission (LSR velocity range of  $10\text{--}12\ \text{km s}^{-1}$ ). However, the emission is associated with neither of the candidate driving sources nor the CO blueshifted emission, and hence the SiO emission is not likely associated with the outflow.

*Flow-9* (probable; Figure 12): an elongated structure with a length of  $\sim 80''$  ( $\sim 32,000\ \text{au}$ ) was detected in the redshifted emission with an LSR velocity range of  $13\text{--}60\ \text{km s}^{-1}$ . The structure is prominent in the observed region, and the corresponding features were also detected in the  $2.12\ \mu\text{m}$   $\text{H}_2$  line image (Stanke et al. 2002). Assuming that the emission originates from a strongly collimated redshifted CO outflow, FraSCO-40 (known as VLA 15), located at the northern end of the collimated emission, is the only candidate driving source. Checking the other side, we also found a blueshifted emission although the emission is difficult to disentangle from the extended emission originating from the cloud velocity.

**Table 9**  
Physical Properties of the Identified CO Outflows

| Name               | R or B | P.A. (deg) | $L_{\text{proj}}$ (au) | $v_{\text{max,proj}}$ (km s $^{-1}$ ) | $t_{\text{dyn,proj}}$ (yr) | $t_{\text{dyn,corr}}$ (yr) |
|--------------------|--------|------------|------------------------|---------------------------------------|----------------------------|----------------------------|
| Flow-1             | R      | -148       | 22,400                 | 19                                    | 5.6E+04                    | 3.2E+04                    |
| Flow-1             | B      | -150       | 23,200                 | 11                                    | 1.0E+05                    | 5.8E+04                    |
| Flow-2             | R      | 104        | 7600                   | 24                                    | 1.5E+04                    | 8.7E+03                    |
| Flow-2             | B      | -76        | 10,400                 | 81                                    | 6.1E+03                    | 3.5E+03                    |
| Flow-3 (northeast) | R      | 27         | 19,200                 | 34                                    | 2.7E+04                    | 1.6E+04                    |
| Flow-3 (northeast) | B      | 37         | 19,200                 | 51                                    | 1.8E+04                    | 1.0E+04                    |
| Flow-3 (southwest) | R      | -154       | 12,000                 | 74                                    | 7.7E+03                    | 4.5E+03                    |
| Flow-3 (southwest) | B      | -144       | 14,800                 | 16                                    | 4.4E+04                    | 2.5E+04                    |
| Flow-4             | R      | -48        | 1080                   | 19                                    | 2.7E+03                    | 1.6E+03                    |
| Flow-4             | B      | ...        | ...                    | ...                                   | ...                        | ...                        |
| Flow-5             | R      | ...        | ...                    | ...                                   | ...                        | ...                        |
| Flow-5             | B      | -90        | 2400                   | 9                                     | 1.3E+04                    | 7.3E+03                    |
| Flow-6             | R      | -150       | 2800                   | 39                                    | 3.4E+03                    | 2.0E+03                    |
| Flow-6             | B      | -150       | 2600                   | 18                                    | 6.9E+03                    | 4.0E+03                    |
| Flow-7             | R      | ...        | ...                    | ...                                   | ...                        | ...                        |
| Flow-7             | B      | -55        | 2000                   | 25                                    | 3.8E+03                    | 2.2E+03                    |
| Flow-8             | R      | 135        | 2600                   | 6                                     | 2.1E+04                    | 1.2E+04                    |
| Flow-8             | B      | 135        | 500                    | 5                                     | 4.8E+03                    | 2.7E+03                    |
| Flow-9             | R      | 155        | 32,000                 | 49                                    | 3.1E+04                    | 1.8E+04                    |
| Flow-9             | B      | -          | ...                    | ...                                   | ...                        | ...                        |
| Flow-10            | R      | 44         | 800                    | 8                                     | 4.8E+03                    | 2.7E+03                    |
| Flow-10            | B      | 44         | 800                    | 10                                    | 3.8E+03                    | 2.2E+03                    |
| Flow-11            | R      | 139        | 6000                   | 19                                    | 1.5E+04                    | 8.7E+03                    |
| Flow-11            | B      | -5         | 8000                   | 11                                    | 3.5E+04                    | 2.0E+04                    |
| Flow-12            | R      | 60         | 36,000                 | 74                                    | 2.3E+04                    | 1.3E+04                    |
| Flow-12            | B      | ...        | ...                    | ...                                   | ...                        | ...                        |

**Note.** R and B correspond to the measured value in the redshifted and blueshifted components, respectively.

Interestingly, we also detected a very collimated knot-like SiO blueshifted emission with an LSR velocity range of  $-5$  to  $5$  km s $^{-1}$  (see the channel maps in the online journal). This emission extends to the north with  $L_{\text{proj}} \sim 14''$  ( $\sim 5600$  au) and is associated with bright components (more than  $0.2$  Jy beam $^{-1}$ ) of the blueshifted CO emission with an LSR velocity in the range of  $-1$  to  $3$  km s $^{-1}$ . No counterpart (i.e., redshifted SiO emission extending to the south) was detected from our observations.

*Flow-10* (clear; Figure 13): a compact bipolar outflow driven by FraSCO-45 (also known as HOPS-369). The blueshifted emission has two peaks and is elongated in the northeast direction with an LSR velocity range of  $3$ – $7$  km s $^{-1}$ , extending with a projected length of  $2''$  ( $\sim 800$  au). The redshifted emission peaks at the location of FraSCO-45. It has an LSR velocity range of  $13$ – $21$  km s $^{-1}$  and extends  $L_{\text{proj}} \sim 2''$  ( $\sim 800$  au). This is the most compact outflow identified in our study.

*Flow-11* (clear; Figure 14): a clear bipolar CO outflow driven by FraSCO-49 (also known as HOPS-368 and VLA 13). The blueshifted emission with  $L_{\text{proj}} \sim 20''$  ( $\sim 8000$  au) and the redshifted emission with  $L_{\text{proj}} \sim 15''$  ( $\sim 6000$  au) extend to the north and south with respect to FraSCO-49, respectively. The CO emission traces a cone-shaped outflow cavity structure, which was previously detected in the *Ks* image (e.g., Takahashi et al. 2008). The blue- and redshifted emissions have LSR velocities up to  $0$  and  $30$  km s $^{-1}$ , respectively. A compact SiO redshifted emission, extending to  $L_{\text{proj}} \sim 3''$  ( $\sim 1200$  au) with  $v_{\text{LSR}} = 15$ – $35$  km s $^{-1}$ , was detected  $\sim 10''$  south of the driving source. This emission is considered to trace shocked gas within the outflow. Note that another compact SiO redshifted emission was detected  $\sim 20''$  ( $\sim 8000$  au) southeast of the driving source.

This emission is not associated with CO emissions originating from flow-11, thus we identified this emission as shocked gas not originating outflow, shock-11 (see Section 3.2.2).

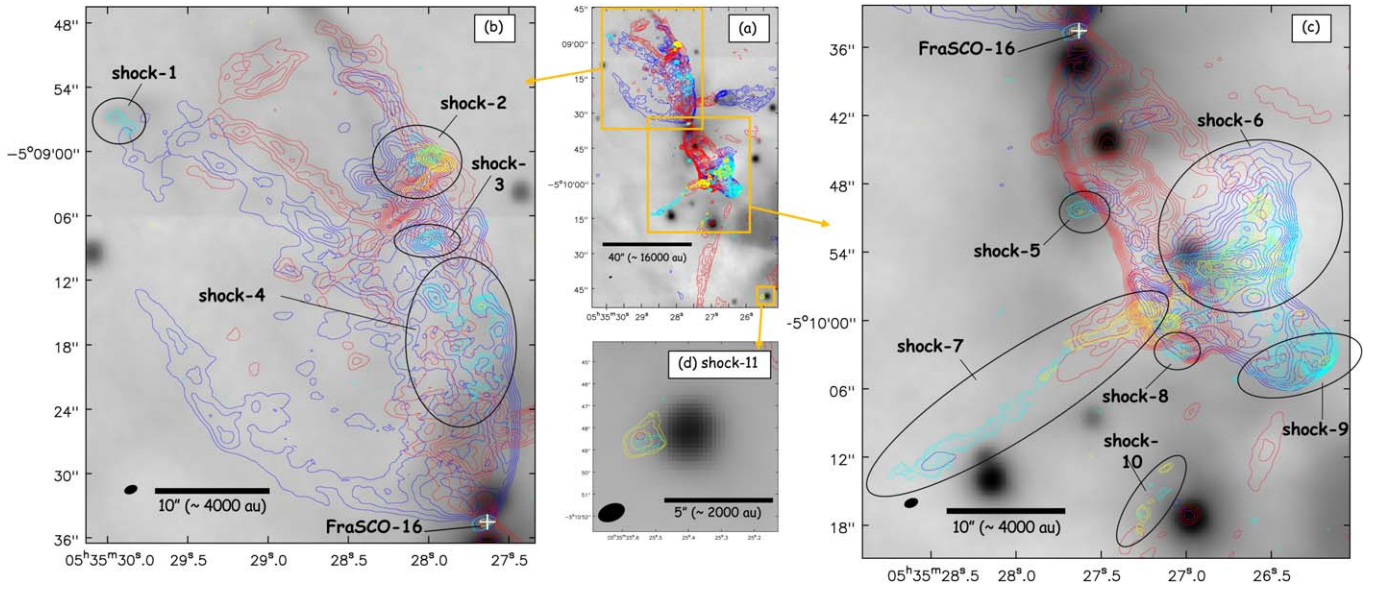
*Flow-12* (clear; Figure 15): this is a known CO outflow driven by FIR 6b also known as HOPS-60 (e.g., Takahashi et al. 2008; Feddersen et al. 2020; Kang et al. 2021; Matsushita et al. 2021). Due to the limited imaging, we only imaged the northern half of the redshifted CO lobe. The redshifted emission extends to  $\sim 90''$  ( $\sim 36,000$  au) in the northeast direction with respect to the driving source. A cavity-like structure appears with an LSR velocity range of  $25$ – $35$  km s $^{-1}$  and a collimated structure appears within the cavity-like structure with an LSR velocity range of  $60$ – $85$  km s $^{-1}$ . Our results are consistent with those in a recent study (Matsushita et al. 2019).

### 3.2.2. Non-outflow Emission Originating from Shocked Gas

In addition to identifying outflows, we identified SiO-shocked gas structures that do not originate from outflows. To identify shocked gas structures, we set the following three criteria: (1) SiO emission detected at greater than  $10\sigma$  in the integrated intensity map (Figure 8), (2) SiO emission shows a gas velocity greater than  $2$  km s $^{-1}$  with respect to the systemic velocity, and (3) SiO gas structure is not associated with the identified outflows in Section 3.2.1.

Based on these criteria, we identified 11 shocked gas structures. An overview and zoomed-in images are presented in Figure 16. Table 10 lists the sizes of the shocked regions measured using the integrated intensity map (Figure 16) showing SiO emission detection greater than the  $8\sigma$  level. The maximum velocity,  $v_{\text{max}}$ , is defined as the difference between the maximum LSR velocity and the systemic velocity,





**Figure 16.** Interacting structure identification. The data and contour levels are the same in each panel. The white cross denotes the position of the flow-3 driving source (FraSCO-16). The gray background images show the  $2.2\ \mu\text{m}$   $K_s$  band image obtained from SIRIUS/IRSF (Takahashi et al. 2008). The red and blue contours are the same as those in Figure 7. The yellow contours represent the integrated intensity map using the redshifted SiO components with a velocity range of  $v_{\text{LSR}} = 12\text{--}29\ \text{km s}^{-1}$ . The yellow contour levels are  $[8, 10, 15, 20, 25, 30, 35, 40, 45, 50, 55] \times 1\sigma$  ( $1\sigma = 0.015\ \text{Jy beam}^{-1}\ \text{km s}^{-1}$ ). The cyan contours represent the integrated intensity map using the blueshifted SiO components with a velocity range of  $v_{\text{LSR}} = -30\ \text{to}\ 11\ \text{km s}^{-1}$ . The cyan contour levels are  $[8, 10, 15, 20, 25, 30, 35, 40, 45, 50, 55, 60, 70, 80, 90, 100, 120, 140, 160, 180, 200] \times 1\sigma$  ( $1\sigma = 0.02\ \text{Jy beam}^{-1}\ \text{km s}^{-1}$ ). In all the figures, the black ellipses at the bottom-left corner are the same as that in Figure 7.

**Table 10**  
Physical Properties of the Identified SiO-shocked Gas

| Name     | Projected Size (au) | $v_{\text{LSR}}$ Range ( $\text{km s}^{-1}$ ) | Comment               |
|----------|---------------------|---|-----------------------|
| Shock-1  | 800                 | −4–10   | ...                   |
| Shock-2  | 1400                | −5–23   | ...                   |
| Shock-3  | 1200                | −1–6  | ...                   |
| Shock-4  | 800                 | 0–13  | Size is a typical one |
| Shock-5  | 1000                | 9–12  | ...                   |
| Shock-6  | 4000                | 0–13  | Previously detected   |
| Shock-7  | 11,200              | 5–21  | ...                   |
| Shock-8  | 800                 | 3–12  | ...                   |
| Shock-9  | 3200                | −14–16  | ...                   |
| Shock-10 | 600                 | 10–14   | Size is a typical one |
| Shock-11 | 840                 | 10–15   | ...                   |

**Note.** We did not assume inclination angles to determine the sizes and velocities. Only shock-6 has been detected in previous SiO( $J = 2-1$ ) line observations.

for SiO emission greater than  $4\sigma$  in the SiO channel maps. Below, we provide detailed results for the individually identified SiO-shocked gas structures.

**Shock-1** (Figure 16(b)): shock-1 was detected at the tip of the blueshifted outflow, flow-3, driven by FraSCO-16. The SiO emission extends to  $\sim 800$  au, showing a blueshifted component with a velocity range of  $-4$  to  $10\ \text{km s}^{-1}$ . Since the emission is detected at the edge of the outflow, the emission might originate from the interacting region between the outflow and surrounding ambient gas. Faint emission associated with SiO emission was detected in the  $K_s$  band, including a  $2.12\ \mu\text{m}$   $\text{H}_2$  shock-originated emission.

**Shock-2** (Figure 16(b)): shock-2 was detected  $\sim 34''$  north of FraSCO-16. The SiO emission shows both blue- and redshifted

emissions with an LSR velocity range of  $-5$  to  $23\ \text{km s}^{-1}$ . The spatial distribution of the SiO emission seems to spatially correlate with the tip of a cavity-like structure, possibly originating from HOPS-350 (flow-1), which seems to interact with a blueshifted outflow emission originating from FraSCO-16, flow-3. No obvious  $K_s$  band emission associated with the SiO emission was detected in shock-2.

**Shock-3** (Figure 16(b)): shock-3 was detected  $\sim 27''$  north of FraSCO-16. The SiO emission extends to  $\sim 2''.5$  and was only detected in the blueshifted component with a velocity range of  $-1$  to  $6\ \text{km s}^{-1}$ . The origin of the emission is uncertain, but it may trace the post-shock region produced by the outflow interaction between flow-1 and flow-3, although the spatial correlation between the outflow cavity and the detected emission is not as clear as shock-1. No obvious  $K_s$  band emission associated with the SiO emission was detected in shock-3.

**Shock-4** (Figure 16(b)): shock-4 was detected  $\sim 15''$  north of FraSCO-16. It consists of several compact components with a typical size of  $\sim 2''$  ( $\sim 800$  au) and distributed over  $\sim 9''$  ( $\sim 3600$  au). The SiO emission was only detected in the blueshifted component with a velocity range of  $0\text{--}13\ \text{km s}^{-1}$ . The detected SiO emission is located in the northern area of the region where flow-2 and flow-3 collide, and hence the origin of the shocked SiO gas might be related to the interaction between those two outflows. No obvious  $K_s$  band emission associated with the SiO emission was detected in shock-4.

**Shock-5** (Figure 16(c)): shock-5 was detected  $\sim 16''$  south of FraSCO-16. The SiO emission was mainly detected as a blue component with a velocity range of  $9\text{--}12\ \text{km s}^{-1}$ , while a redshifted component was detected marginally with a  $3\sigma$  emission level in the integrated intensity map. The structure is as compact as  $\sim 2''.5$  ( $\sim 1000$  au). A faint emission associated with the SiO emission was detected in the  $K_s$  band. This compact SiO emission is located just outside the outflow lobes

of flow-3 detected with both red- and blueshifted CO components. This SiO emission seems to show a local shock created by the outflow lobe from flow-3 interacting with ambient dense gas. Indeed, the CO lobe from flow-3 detected for both blue- and redshifted gas shows a clear anticorrelation with the dust lane traced by the 1.3 mm continuum emission (further discussion in Section 4.1.1). The SiO emission is located between the CO outflow and dust lane. This also supports the suggestion that the local shock is produced by the interaction between the outflow and the dust lane.

*Shock-6* (Figure 16(c)): shock-6 was detected  $\sim 23''$  southwest of FraSCO-16. The detected SiO emission is the most extended and brightest component in the observed area. The emission extends to  $\sim 10''$  ( $\sim 4000$  au). The SiO emission was previously detected in SiO( $J = 2-1$ ) by Shimajiri et al. (2008) with a velocity range of  $4-13$  km s $^{-1}$ . Our observations also confirmed this detection with a higher transition of SiO ( $J = 5-4$ ). The emission was detected with both blue- and redshifted velocity and the LSR velocity range is  $0-13$  km s $^{-1}$ . The spatial distribution of the SiO blueshifted emission is well correlated with that of the CO blueshifted emission. Their velocity coverage is the same. In contrast, there is no clear spatial correlation between the SiO blueshifted emission and the CO redshifted emission, but rather an anticorrelated distribution is suggested between CO (mainly tracing the flow-3 lobe) and SiO (shock-originated gas distributed at the edge of the outflow lobe). The interaction between flow-3 and dense gas in the FIR 4 region was suggested by Shimajiri et al. (2008) based on previous SiO observations and also Nakamura et al. (2019) using multi-molecular line observations. Our SiO result, showing an arc-like structure (particularly recognized around the systemic velocity), geometrically suggests an interaction between flow-3 and dense gas from the FIR 4 region. Our result does not conflict with the proposed scenario by Shimajiri et al. (2008). It is important to note that two outflows (flow-4 and flow-5; see Figure 10) are identified within the FIR 4 region, where strong CO and SiO emissions are located at shock-6. It is difficult to disentangle the CO and SiO blueshifted emissions associated with shock-6 and flow-5 because they overlap spatially and also in the velocity domain. Moreover, another outflow, flow-9, shows a chain-like collimated outflow (see Figure 12). The distribution of the blueshifted collimated SiO emission reaches shock-6. Our results show very complicated SiO and CO emission distributions within a protocluster star-forming environment. Further discussion and interpretation will be presented in Sections 4.1 and 4.2.

*Shock-7* (Figure 16(c)): the SiO emission for shock-7 shows an elongated structure with an overall length of  $\sim 28''$  ( $\sim 11,200$  au). This structure is located southeast of shock-6. The SiO emission shows an LSR velocity range of  $5-21$  km s $^{-1}$  with a smooth velocity gradient. The redshifted velocity component seems to be connected to the velocity component observed in shock-6, and hence both emissions may be related. The elongated structure showing both blue- and redshifted components seems to be explained by the molecular outflow; however, no driving source candidate was found in the region searching with multiwavelength images.

*Shock-8* (Figure 16(c)): shock-8 was detected  $\sim 30''$  south of FraSCO-16. The SiO emission was mainly detected in the blueshifted component with a velocity range of  $3-12$  km s $^{-1}$ , while a redshifted component was detected marginally with a

$3\sigma$  emission level in the integrated intensity map. The structure is as compact as  $\sim 2''$  ( $\sim 800$  au). This compact SiO emission seems to be located at the tip of flow-3 and seems to show a local shock created by the outflow lobe from flow-3 interacting with ambient dense gas.

*Shock-9* (Figure 16(c)): shock-9 was detected  $\sim 35''$  southwest of FraSCO-16. The blueshifted component of the SiO emission extends  $\sim 8''$  ( $\sim 3200$  au) in the east-west direction with an LSR velocity range of  $-14$  to  $16$  km s $^{-1}$ . The spatial distribution of the blueshifted component is well correlated with that of the CO blueshifted emission, as shown in Figure 16(c). A compact redshifted component of SiO emission is associated with the blueshifted component at R.A. =  $05^{\text{h}}35^{\text{m}}26^{\text{s}}.179$ , decl. =  $-05^{\circ}10'03''.638$ . Note that the SiO emission originating from flow-9 overlaps with the blueshifted component of shock-9 in the south-north direction (Figure 12). Shock-9 was newly resolved as an isolated feature in a SiO emission. Shock-9 seems to show a local shock created by the outflow lobe from flow-3 interacting with ambient dense gas.

*Shock-10* (Figure 16(c)): shock-10 was detected at R.A. =  $05^{\text{h}}35^{\text{m}}27^{\text{s}}.193$ , decl. =  $-05^{\circ}10'15''.172$  and consists of a few blobs with a typical size of  $\sim 1''.5$  ( $\sim 600$  au). The LSR velocity of the detected blobs has a range of  $10-14$  km s $^{-1}$ , which is close to the systemic velocity. The blobs are distributed along the northwest to southeast direction. The origin of the SiO emission potentially tracing shocked gas is not clear because there is no direct evidence of gas interaction caused by an outflow.

*Shock-11* (Figure 16(d)): shock-11 was detected at R.A. =  $05^{\text{h}}35^{\text{m}}25^{\text{s}}.527$ , decl. =  $-05^{\circ}10'48''.637$ . It extends  $\sim 2''.1$  ( $\sim 840$  au) with an LSR velocity range of  $10-15$  km s $^{-1}$ . This compact emission is also detected in the CO emission with the same velocity range. Around the detected SiO emission, there is a Two Micron All Sky Survey (2MASS) source located  $\sim 2''$  west of shock-11. This SiO emission may be explained by an outflow from this source. However, the 2MASS source is detected in the  $J$ ,  $H$ , and  $K_s$  bands (Nielbock et al. 2003), suggesting the source is evolved and not likely associated with the dense envelope. In addition, the SiO emission is only detected at the relative velocity of  $\leq 4$  km s $^{-1}$ . Therefore, the emission likely does not originate from a molecular outflow driven by this 2MASS source. The origin of this emission is uncertain.

#### 4. Discussion

In this section, we discuss the star-forming environment in the FIR 4 region, which is presented in Figure 4(b). The FIR 4 region ( $L = 1000 L_{\odot}$ ; Crimier et al. 2009) is known to be the most bright and centrally concentrated dust condensation within the embedded protocluster (Chini et al. 1997; Lis et al. 1998; Johnstone & Bally 1999). Previous millimeter and submillimeter interferometric observations have suggested possible star formation activity within the FIR 4 region (Shimajiri et al. 2008; Takahashi et al. 2008; López-Sepulcre et al. 2013; Fontani et al. 2017; Osorio et al. 2017; Favre et al. 2018; Nakamura et al. 2019; Tobin et al. 2019; Evans et al. 2022). Multiwavelength infrared and centimeter observations have also revealed that the region contains several sources, indicating the presence of protostellar candidates (Reipurth et al. 1999; Megeath et al. 2012; Furlan et al. 2016; Osorio et al. 2017). Our ALMA 12 m array observations, with an angular resolution of  $\sim 1''$ , spatially resolved substructures

within the FIR 4 region in the 1.3 mm continuum emission. In addition, the spatial distributions of outflow and shock-originated gas were traced by CO and SiO emissions. In Section 4.1, we use this data set to discuss three previously proposed scenarios to explain the star formation environment in the FIR 4 region. In Section 4.2, we compare timescales to assess the previously proposed triggered star formation scenario within the FIR 4 region. Finally, in Section 4.3, we discuss a hub-filament system in the FIR 4 region.

#### 4.1. Star Formation Environment in the FIR 4 Region

Three possible scenarios have been proposed in previous studies to explain the origin of the protocluster in the FIR 4 region. The first scenario is the collision of an energetic outflow, flow-3, driven from FraSCO-16 (known as HOPS-370) in the FIR 3 region, with the dust condensation, FIR 4 (Shimajiri et al. 2008; Nakamura et al. 2019; Tobin et al. 2019). Shimajiri et al. (2008) found 11 dust condensations embedded within the FIR 4 region. Since these condensations are located around the southwest tip of flow-3, it was proposed that the interaction triggered a fragmentation process within the protocluster and formed next-generation protostars in the FIR 4 region. The second scenario is that the large  $L_{\text{bol}}$  indicated in the FIR 4 region ( $L = 1000 L_{\odot}$ ) originates from an internal source (López-Sepulcre et al. 2013). López-Sepulcre et al. (2013) proposed that the FIR 4 region could be a H II region powered by a B3-B4 type young star. The third scenario is that the FIR 4 region is irradiated by an external source but not by flow-3 (Fontani et al. 2017; Favre et al. 2018; Evans et al. 2022). These three scenarios have been mainly examined with regard to (sub)millimeter interferometric observations with a single pointing. However, some of the observations have an insufficient angular resolution of  $1''.5\text{--}6''$  to spatially resolve substructures and shocked gas within the FIR 4 region (Shimajiri et al. 2008; López-Sepulcre et al. 2013; Favre et al. 2018; Evans et al. 2022). ALMA 0.87 mm observations by Tobin et al. (2019) and ALMA 1.3 mm observations by Tobin et al. (2020) have a high-angular resolution of  $\sim 0''.25$  and can image dust emission and several molecular lines from sources embedded in the FIR 4 region, though their fields of view do not cover the whole FIR 4 region, and therefore cannot be used to investigate each proposed scenario. Our ALMA 12 m array observations covered a large spatial area to map the entire FIR 3 and FIR 4 regions with a sufficiently high-angular resolution of  $\sim 1''$  to spatially resolve substructures within each region.

In summary, we have spatially resolved the 1.3 mm continuum, CO( $J = 2\text{--}1$ ), and SiO( $J = 5\text{--}4$ ) emissions across the FIR 3 and FIR 4 regions for the first time. Our data set enables us to discuss the three previously proposed scenarios to explain the protocluster environment in the FIR 4 region. We compared the spatial locations between the shocked gas traced by SiO( $J = 5\text{--}4$ ), the outflow originating emission traced by CO( $J = 2\text{--}1$ ), and the dust filament traced in the 1.3 mm continuum emission. Our results are most consistent with an interaction model between the energetic flow-3 and the dense condensations within the FIR 4 region that is described in Section 4.1.1. The schematic picture of the model is summarized in Figure 18. In the following, we discuss the three proposed scenarios.

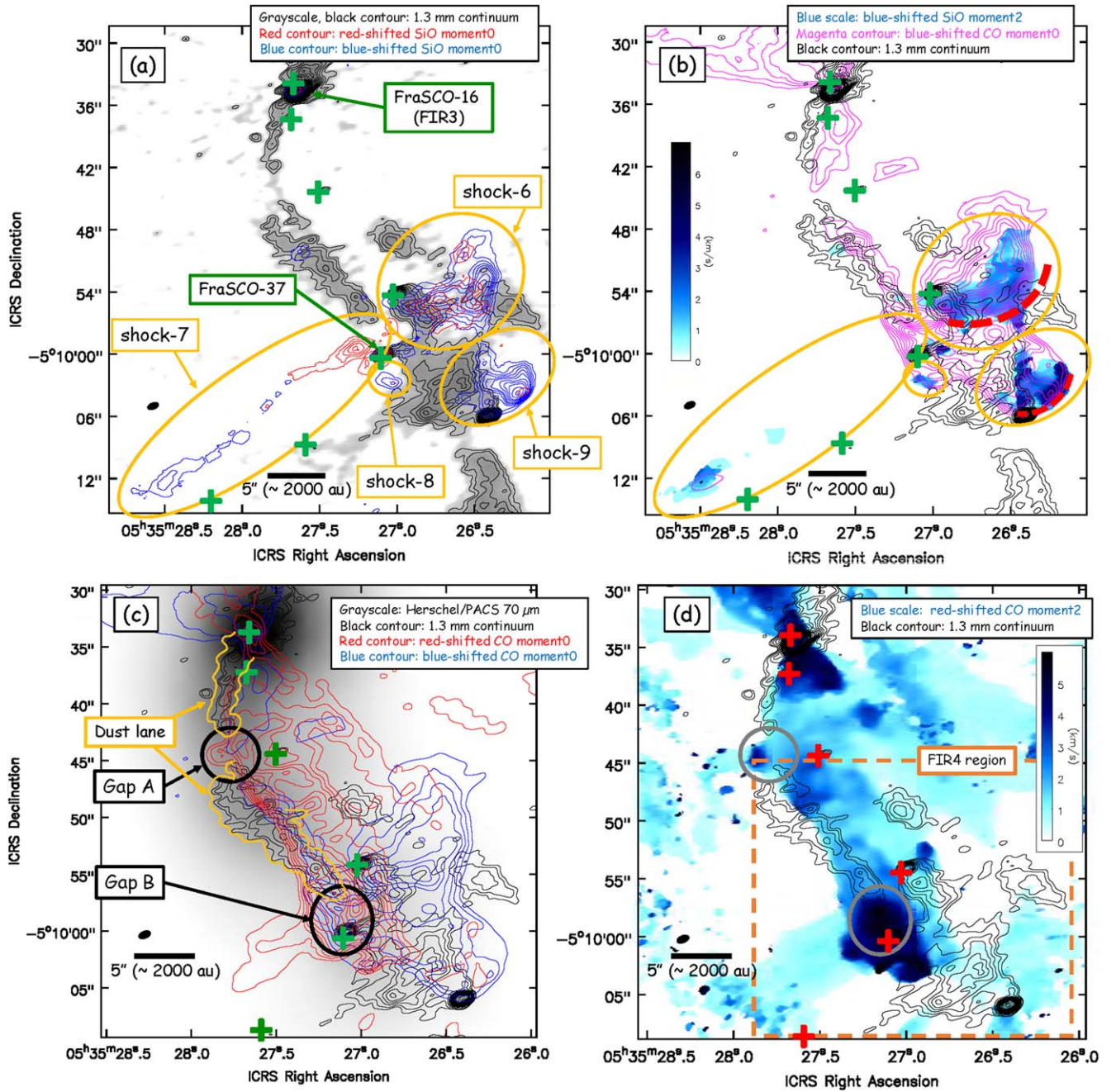
##### 4.1.1. Outflow Interaction Scenario

Shock-originating SiO ( $J = 2\text{--}1$ ) emission was previously detected in the FIR 4 region and interpreted as an interaction between the molecular outflow (flow-3) and a dense clump (Shimajiri et al. 2008). Our ALMA 12 m array observations, with a higher transition of SiO( $J = 5\text{--}4$ ), spatially resolved further detailed structures to strengthen the outflow–dense clump interaction scenario. The SiO( $J = 5\text{--}4$ ) emission was detected in four regions within the FIR 4 region (shock-6, shock-7, shock-8, and shock-9 shown in Figure 17(a)). Among the four components, shock-6 and shock-9 show very clear U-shaped structures, denoted by red-dashed lines in Figure 17(b). These two shocks also seem to be located downstream of the southwest lobe of flow-3. Shock-6 was previously detected in SiO ( $J = 2\text{--}1$ ) observations by Shimajiri et al. (2008) with a similar velocity range, whereas shock-9 is newly detected in this study.

As presented in Figure 17(b), both shock-6 and shock-9 show large velocity dispersion in the range of  $\sim 2\text{--}5 \text{ km s}^{-1}$  in the SiO( $J = 5\text{--}4$ ) emission. For shock-6, the SiO gas distribution partially overlaps the blueshifted CO emission. The 1.3 mm continuum emission is distributed downstream of shock-6. The positional relationship between the 1.3 mm dust, CO, and SiO emissions can be explained by an interaction between flow-3 and dust condensations located in the FIR 4 region. The SiO emission from shock-9 also seems to spatially correlate with the southwest tip of the outflow lobe traced by the CO blueshifted emission, as described in Figure 17(b). Unlike the case of shock-6, we did not detect dust condensations downstream of shock-9. A possible explanation for this is that the interacting condensations are not dense enough to be traced by our ALMA 12 m array continuum observations ( $n_{\text{H}_2} \lesssim 3.9 \times 10^6 \text{ cm}^{-3}$ ). Alternatively, their structure is rather extended and the emission is not detected with our 12 m array observations ( $\gtrsim 5200 \text{ au}$ ). Indeed, an extended continuum emission was detected in that region both in the 1.3 mm continuum emission with our ACA 7 m array and by previous single-dish (sub)millimeter continuum observations (Chini et al. 1997; Lis et al. 1998; Johnstone & Bally 1999).

We also found a southwest outflow lobe of flow-3, clearly shaped by the surrounding dense material. The eastern edge of the CO outflow lobe, which is detected in both blue- and redshifted CO emissions, shows a tight spatial correlation with the 1.3 mm continuum emission (denoted as the *dust lane* in Figure 17(c), which is bright all along the edge). The CO contours are very steep at that edge of the outflow, indicating that the outflow is clearly compressed along the entire eastern edge. The CO second moment map presented in Figure 17(d) also shows that a large CO velocity dispersion (up to  $10 \text{ km s}^{-1}$ ) associated with the eastern edge of the CO outflow lobe has a tight correlation with the 1.3 mm continuum emission. These tight correlations support a scenario in which the outflow lobe interacts with filamentary dense structures traced by the 1.3 mm continuum emission, distributed just next to the outflow lobe. Note that the southwest lobe of flow-3 has a smaller opening angle compared with the northeast lobe of flow-3, as described in Section 3.2.1 (Figure 9(c)). This implies that the surrounding material traced by the continuum emission prevents gas at the eastern edge of the southwest outflow lobe from expanding freely. Tobin et al. (2019) pointed out that the mid-infrared emission (24 and  $70 \mu\text{m}$  band images), indicating warm dust, is bright not only at the location of FraSCO-16





**Figure 17.** Spatial distribution comparisons between the 1.3 mm continuum, CO( $J = 2-1$ ), SiO( $J = 5-4$ ), and Herschel/PACS  $70\ \mu\text{m}$  emissions. In all figures, the black contours represent the 1.3 mm continuum emission and the contour levels are [7, 10, 15, 20, 25, 30, 35, 40, 45, 50, 60, 70, 80, 90, 100, 120, 150, 170, 200, 300, 400, 500, 600, 700]  $\times 1\sigma$  ( $1\sigma = 0.22\ \text{mJy beam}^{-1}$ ). The black-filled ellipses in the bottom-left corner show the synthesized beam size of the continuum image. The green and red crosses show the positions of previously identified infrared sources (Nielbock et al. 2003; Furlan et al. 2016). (a) The 1.3 mm continuum image overlaid with the SiO( $J = 5-4$ ) moment 0 images separated with red- ( $v_{\text{LSR}} = 12-30\ \text{km s}^{-1}$ ) and blueshifted ( $v_{\text{LSR}} = -30$  to  $10\ \text{km s}^{-1}$ ) components. The blue contour levels are [10, 20, 30, 40, 50, 60, 80, 100, 120, 160, 200]  $\times 1\sigma$  ( $1\sigma = 0.02\ \text{Jy beam}^{-1}$ ). The red contour levels are [10, 20, 30, 40, 50]  $\times 1\sigma$  ( $1\sigma = 0.015\ \text{Jy beam}^{-1}$ ). Locations of the identified shocked regions (shock-6, shock-7, shock-8, and shock-9) are denoted by yellow ellipses. (b) The 1.3 mm continuum image overlaid with a moment 2 image obtained from the SiO( $J = 5-4$ ) blueshifted component ( $v_{\text{LSR}} = -30$  to  $10\ \text{km s}^{-1}$ ) and a moment 0 image obtained from the CO( $J = 2-1$ ) blueshifted component ( $v_{\text{LSR}} = -10$  to  $10\ \text{km s}^{-1}$ ). The magenta contour levels are [10, 15, 20, 25, 30, 35, 40, 45, 50, 55, 60, 65, 70, 75, 80]  $\times 1\sigma$  ( $1\sigma = 0.23\ \text{Jy beam}^{-1}$ ). The two red-dashed lines represent the U-shaped structures mentioned in the main text (indicating interacted regions between outflows and surrounding dense materials). Locations of the identified shocked regions (shock-6, shock-7, shock-8, and shock-9) are denoted by yellow ellipses. (c) Spatial distribution comparisons between the Herschel/PACS  $70\ \mu\text{m}$  (grayscale), 1.3 mm continuum (black contours), and CO( $J = 2-1$ ) moment 0 images (red and blue contours). The CO( $J = 2-1$ ) moment 0 images were produced with the red- ( $v_{\text{LSR}} = 15-85\ \text{km s}^{-1}$ ) and blueshifted ( $v_{\text{LSR}} = -10$  to  $10\ \text{km s}^{-1}$ ) components separately. The red contour levels are [10, 20, 30, 40, 50, 60, 70, 80, 90]  $\times 1\sigma$  ( $1\sigma = 0.17\ \text{Jy beam}^{-1}$ ). The blue contour levels are [10, 20, 30, 40, 50, 60, 70]  $\times 1\sigma$  ( $1\sigma = 0.23\ \text{Jy beam}^{-1}$ ). The dust lane is marked with an orange solid line. The two black circles represent the locations of Gap A and Gap B. (d) Moment 2 image obtained from the CO( $J = 2-1$ ) redshifted component ( $v_{\text{LSR}} = 15-85\ \text{km s}^{-1}$ ). The two gray circles represent the locations of Gap A and Gap B. The orange-dashed square corresponds to the FIR 4 region.

(HOPS-370) where a protostar is located, but also along the dust filament extending to the south ( $\sim 30''$ ). We found that the elongated direction of the warm dust corresponds to the region where a strong interaction occurs between the outflow lobe and dust lane, as presented in Figure 17(c). Spatial correlations between the outflow lobe, dust lanes, and the large velocity dispersion of the CO gas clearly support a scenario where the dust emission from the dust lane arises from shock-originating warm dust produced by the interaction between flow-3 and the dust lanes.

It is interesting to note that there is spatial anticorrelation between the 1.3 mm continuum emission and the redshifted CO emission tracing the east edge of the southwest outflow lobe, as presented in Figure 17(c). Redshifted CO gas appears to be leaking from gaps in the dust lanes traced by the 1.3 mm continuum emission, denoted by Gap A and Gap B in Figure 17(c). The redshifted CO components of flow-3 are flowing with a P.A. of  $210^\circ$ . At the positions of both Gap A and Gap B, a part of the redshifted CO emission suddenly changes the P.A. to  $\sim 120^\circ$ , i.e., the P.A. of the flow changes  $90^\circ$  clockwise. Furthermore, the CO second moment map shows local spots at Gap A and Gap B, which show an increased velocity dispersion up to 5.0 and 9.7 km s $^{-1}$ , respectively (Figure 17(d)). This value is 1.5–2 times larger than that of the typical velocity dispersion measured in other parts of the outflow lobe. This can be interpreted as showing that the CO outflow collides with surrounding dense materials (i.e., observed as the dust condensation) and is compressed at the locations of Gap A and Gap B, resulting in a part of the outflow being changed by  $90^\circ$  in P.A., and the redshifted gas is a hint of leaking through a low-density region of the dust lane.

Furthermore, two SiO components identified as shock-8 and shock-7 are detected at the eastern edge of the southwest lobe of flow-3 (see Figure 17(a)). In particular, shock-8 and the redshifted component of shock-7 with a large velocity dispersion of  $\sim 5$  km s $^{-1}$  are detected at the region where the eastern edge of the redshifted CO outflow lobe changes the P.A. with a local increment of the velocity dispersion up to 11 km s $^{-1}$ . This is considered to be another local point having a strong interaction between the outflow and dense material traced by the 1.3 mm continuum emission.

In summary, as presented in a schematic image (Figure 18), we have revealed detailed spatial distributions of shock-originating gas traced by higher transition SiO( $J = 5-4$ ) emissions. We confirmed that the shocked region associated with previously detected shocked gas has a U-shaped structure at the colliding surface between flow-3 and the condensations within the FIR 4 region. In addition, another interaction region was newly detected further downstream of flow-3. Furthermore, our observations revealed that the eastern side of the flow-3 southwest lobe interacts with surrounding dense dust material. The interacting material shows a narrow dust lane and the velocity dispersion of flow-3 increases around the dust lane. These results are clear evidence that a prominent outflow driven by FraSCO-16, flow-3, significantly interacts with surrounding material and possibly affects the star formation environment in the FIR 4 region. Thus, our results strongly support the outflow interaction scenario.

#### 4.1.2. Internal Heating Source Scenario

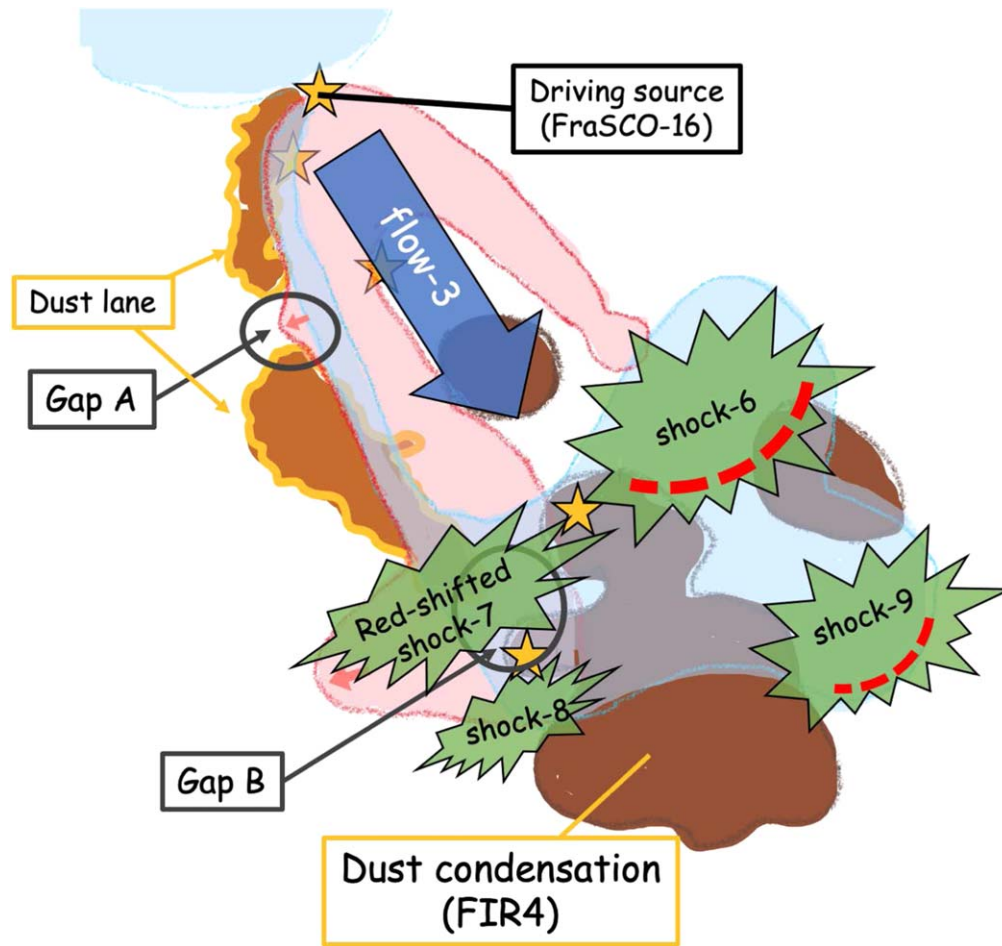
López-Sepulcre et al. (2013) obtained CH $_3$ OH, DCO $^+$ , C $^{34}$ S, DCN, and NH $_3$  line images with an angular resolution of

$\sim 2''.7$  centered at FIR 4 ( $\sim 35''$  FoV). Based on the observations, they proposed an internal heating scenario from an embedded B star. Their conclusion was drawn from (i) the large bolometric luminosity estimated in the FIR 4 region ( $1000 L_\odot$ ; Crimier et al. 2009) and (ii) their interferometric observations, showing a bright peak in the 2 mm continuum emission and CH $_3$ OH at the center of the FIR 4 region. The source position coincides with a previously detected 3.6 cm source, VLA 12, identified by Reipurth et al. (1999), which is considered to be a free-free jet. A more recent centimeter wavelength study by Osorio et al. (2017) spatially resolved VLA 12 into three components, VLA 12C, HOPS-108 (associated with FraSCO-37), and VLA 12S using multi-wave bands between 5 and 0.7 cm. Their proper motion study concluded that only HOPS-108 originates from the heating source embedded within the FIR 4 region, while VLA 12C and VLA 12S are likely associated with radio jets driven by HOPS-370 located within the FIR 3 region. In addition, an infrared wavelength study with higher angular resolution resolving individual sources within the FIR 4 region by Furlan et al. (2016) reestimated the bolometric luminosity of HOPS-108 as  $38.3 L_\odot$ . Assuming that the bolometric luminosity of  $38.3 L_\odot$  originates from the stellar luminosity at a stellar age of  $\sim 10^5$  yr, the spectral type of the star is expected to be G0-G5 based on the relation between the stellar luminosity and effective temperature (Palla & Stahler 1993). In fact, HOPS-108 is classified as a Class 0 source from its spectral energy distribution (Furlan et al. 2016). Therefore, most of the bolometric luminosity likely originates from accretion luminosity (not stellar-internal luminosity). This indicates that the stellar luminosity should be much less than  $38.3 L_\odot$ , i.e., the embedded source is less massive than G0-G5 stars. Finally, the FWHM for FraSCO-37 associated with HOPS-108 is measured to be  $\sim 0''.8$  from a 2D Gaussian fitting to our 1.3 mm continuum image. The gas mass of FraSCO-37 is also estimated to be  $0.18 M_\odot$  from the 1.3 mm continuum observations, which is an order of magnitude less than typical B-type stellar masses (2.68–17.7  $M_\odot$ ; Pecaut & Mamajek 2013). Updated observational results since López-Sepulcre et al. (2013) provide further support that HOPS-108 (considered to be a main source in the FIR 4 region) is likely to be an ordinary Class 0 source, but not an embedded B-type source. Hence, our study does not strongly support this internal heating scenario and indicates that the large bolometric luminosity estimated in the FIR 4 region is mainly caused by the interaction between the outflow and the dust condensation of FIR 4.

#### 4.1.3. Irradiation by a Far-UV Field Scenario

Fontani et al. (2017) made HC $_3$ N and HC $_5$ N observations centered at FIR 4 (FoV  $\sim 60''$  and  $\theta \sim 6''$ ), under the framework of the IRAM/NOEMA Large Program SOLIS. They found that the HC $_3$ N/HC $_5$ N abundance ratio is smaller ( $\leq 10$ ) in the eastern region of the FIR 4 region than in the western region. According to their chemical models, this small ratio can be reproduced only when the cosmic-ray ionization rate is as large as  $\sim 4 \times 10^{-14}$  s $^{-1}$  in the eastern region. This value is  $\sim 1000$  times higher than that of the interstellar medium, implying that the FIR 4 region is strongly irradiated. Hence, they proposed that the FIR 4 region is irradiated by energetic cosmic-ray particles from an interior embedded source, following the internal heating source scenario proposed by López-Sepulcre et al. (2013). As discussed in Section 4.1.2, our observations do





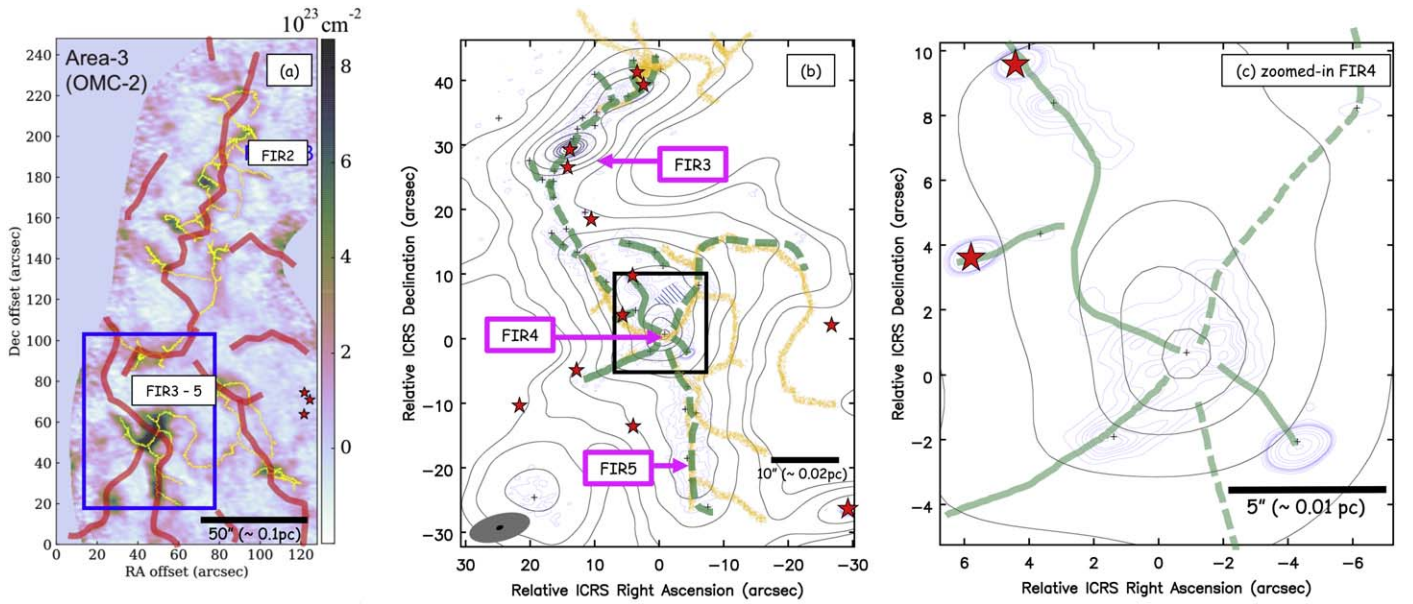
**Figure 18.** Schematic image of the interaction between flow-3 and condensations within the FIR 4 region. The yellow star symbols show the locations of FraSCO sources associated with infrared sources (Nielbock et al. 2003; Furlan et al. 2016). The red and blue colored sketches represent the red- and blueshifted CO gas of flow-3 from FraSCO-16, respectively. The brown-colored sketches represent the condensations within the FIR 4 region. The blue arrow presents the proceeding directions of flow-3. The four green shock-shaped sketches denote shock-6, shock-7, shock-8, and shock-9, indicating interactions of flow-3 with condensations within the FIR 4 region (brown area). The two red-dashed lines represent the U-shaped structures observed in the  $\text{SiO}(J = 5-4)$  emission at the locations of shock-6 and shock-9 presented in Figure 17(b).

not support the scenario by López-Sepulcre et al. (2013). A follow-up study by Favre et al. (2018) performed  $c\text{-C}_3\text{H}_2$  observations centered at FIR 4 ( $\text{FoV} \sim 60''$  and  $\theta \sim 6''$ ) in the same framework as Fontani et al. (2017). They derived the excitation temperature distribution within the FIR 4 region using chemical models. They noted that if the outflow interaction scenario proposed by Shimajiri et al. (2008) is appropriate, there should be some physically induced effects such as temperature gradients along the outflow axis of flow-3 as evidence of the interaction between flow-3 and the FIR 4 region. However, their  $c\text{-C}_3\text{H}_2$  observations do not show a temperature gradient along the outflow axis, suggesting that there is no evidence of direct physical interaction between flow-3 and objects within the FIR 4 region. Their  $c\text{-C}_3\text{H}_2$  observations instead show that the cosmic-ray ionization rate in the eastern side of the FIR 4 region is higher than in the western side and the value of  $\sim 4 \times 10^{-14} \text{ s}^{-1}$  is high enough to show that the eastern region is irradiated, which is consistent with the case of  $\text{HC}_5\text{N}$  observations by Fontani et al. (2017). Furthermore, they noted that previous Herschel observations show that there is a tenuous cloud between OMC-2 illuminated by a far-UV (FUV) field. They concluded that the FIR 4 region

is bathed in an FUV field and is irradiated by energetic particles.

These previous studies have investigated the chemical properties in the FIR 4 region, but did not directly investigate the dynamical properties of flow-3 itself, which would be relevant to the discussion of the interaction between flow-3 and objects within the FIR 4 region. Comparing a map of the  $\text{HC}_3\text{N}/\text{HC}_5\text{N}$  abundance ratio derived by Fontani et al. (2017) with our CO image, the area where the abundance ratio is small is spatially in agreement with the tip of the redshifted CO outflow lobe. From another comparison of the temperature distribution derived by Favre et al. (2018) and our CO second moment map, we found that the location of the  $c\text{-C}_3\text{H}_2$  temperature peak is located downstream of Gap B. Furthermore, the P.A. of the redshifted CO outflow after colliding with objects within the FIR 4 region ( $\sim 120^\circ$ ) is well aligned with the temperature gradient perpendicular to the outflow axis obtained from the  $c\text{-C}_3\text{H}_2$  presented in Figure 4 of Favre et al. (2018). These spatial correlations imply that the interaction between flow-3 and objects within the FIR 4 region creates a shock, heating the surrounding materials and decreasing the abundance ratio. Although our data set does not contradict the





**Figure 19.** (a)  $\text{N}_2\text{H}^+$  ( $J = 1-0$ ) column density map, as in Figure 3 of Zhang et al. (2020). The yellow and red lines represent the  $\text{N}_2\text{H}^+$  fibers identified by Zhang et al. (2020) and Hacar et al. (2018), respectively. The blue frame shows the area of panel (b). (b) Fiber-like structures identified with a 1.3 mm continuum image with the ALMA 12 m array (blue contours). Our identified three fiber-like structures (green-dashed lines) are consistent with some of the  $\text{N}_2\text{H}^+$  fibers (yellow lines, as in panel (a)), whereas the six fiber-like structures denoted by the green solid lines are newly identified. The red star symbols represent the locations of previously detected infrared sources (Nielbock et al. 2003; Furlan et al. 2016). The locations of FIR 3, 4, and 5 (Chini et al. 1997) are indicated by pink arrows. The blue contour levels are  $[5, 10, 15, 20, 25, 30] \times 1\sigma$  ( $1\sigma = 0.22 \text{ mJy beam}^{-1}$ ). The gray contours represent the 1.3 mm continuum emission with the ACA 7 m array. The gray contour levels are  $[10, 20, 50, 100, 150, 230, 290, 310, 325, 340] \times 1\sigma$  ( $1\sigma = 0.78 \text{ mJy beam}^{-1}$ ). The black frame shows the area of panel (c). (c) Zoomed-in image of the FIR 4 region. The gray contour levels are  $[160, 240, 290, 310, 325] \times 1\sigma$  ( $1\sigma = 0.78 \text{ mJy beam}^{-1}$ ). The blue contour levels are  $[16, 20, 23, 25, 27, 28, 30, 40, 60, 80, 130, 170] \times 1\sigma$  ( $1\sigma = 0.22 \text{ mJy beam}^{-1}$ ). The red star, black crosses, and green lines are the same as those in panel (b).

scenario where the FIR 4 region is likely bathed in an FUV field, as proposed by Fontani et al. (2017) and Favre et al. (2018), our study indicates that the heating source causing the high cosmic-ray rate and low abundance rate of the  $\text{HC}_3\text{N}/\text{HC}_5\text{N}$  may originate from the interaction between the outflow and the dust condensation of FIR 4.

#### 4.2. Star Formation Triggered by Molecular Outflow

In the previous section, we presented evidence of the interaction between flow-3 and condensations within the FIR 4 region. Shimajiri et al. (2008) analyzed fragmentation within the FIR 4 region, considered to occur due to an interaction between flow-3 and a clump within the FIR 4 region. They identified 11 cores within the FIR 4 region and estimated a fragmentation timescale ( $\tau_{\text{frag}}$ ) of  $3.8 \times 10^4 \text{ yr}$  by measuring the separations between the identified cores. We compare the peak positions of the 11 cores with those of our identified FraSCO sources in Appendix A. Shimajiri et al. (2008) also estimated the dynamical timescale ( $\tau_{\text{dyn}}$ ) of the outflows associated with flow-3 as  $1.4 \times 10^4 \text{ yr}$  with the  $\text{CO}(J = 3-2)$  line emission. Assuming that  $\tau_{\text{dyn}}$  is similar to an interaction timescale ( $\tau_{\text{interact}}$ ), they interpreted  $\tau_{\text{dyn}} \sim \tau_{\text{interact}} \sim \tau_{\text{frag}}$ . In addition, they found that mid-infrared sources detected by Nielbock et al. (2003) were located at the root of the outflow and along the lobe. From these estimates and previous IR observations, Shimajiri et al. (2008) proposed a triggered star formation scenario within the FIR 4 region using the following four steps:

1. An embedded star associated with a mid-infrared source was born within the FIR 3 region and drove the outflow (i.e., HOPS-370 drove flow-3).

2. The outflow driven by the embedded star started interacting with the FIR 4 region.
3. The interaction caused the fragmentation of the FIR 4 region into 11 cores.
4. These cores will form stars.

Megeath et al. (2012) and Furlan et al. (2016) developed a model of the spectral energy distribution fitting for protostars in this region. They classified two sources within the FIR 3 and FIR 4 regions as Class I sources. This indicates that star formation within both these regions started at almost the same time, which is inconsistent with the triggered star formation scenario proposed by Shimajiri et al. (2008). Therefore, the scenario requires further consideration.

We estimated the fragmentation timescale ( $\tau_{\text{frag}}$ ) of FraSCO sources within the FIR 4 region assuming that  $\tau_{\text{frag}}$  is a sound crossing timescale, following Equations (4)–(6), described in Shimajiri et al. (2008). First, we estimate the average three-dimensional separation among FraSCO sources located within the FIR 4 region by

$$\Delta l = 2\left(\frac{1}{\gamma^{1/3}} - 1\right)r, \quad (4)$$

$$\gamma = \frac{n_{\text{leaf}} V_{\text{leaf}}}{V_{\text{clump}}}, \quad (5)$$

where  $\gamma$ ,  $r$ ,  $n_{\text{leaf}}$ ,  $V_{\text{clump}}$ , and  $V_{\text{leaf}}$  are the volume filling factor, average radius of the FraSCO sources, number of sources, and average volume of the FIR 4 region and a single source, respectively. Note that only  $V_{\text{clump}}$  was estimated from our ACA 7 m array data and the remaining values were estimated from our ALMA 12 m array data. Then, we can estimate  $\tau_{\text{frag}}$

by the following formula:

$$\tau_{\text{frag}} = \frac{\Delta l}{C_{\text{eff}}}, \quad (6)$$

where  $C_{\text{eff}}$  is the effective speed of sound estimated from the line. Here, we employed the same value of  $C_{\text{eff}}$  used by Shimajiri et al. (2008) because our observations do not include any line data tracing dense material detected with the 1.3 mm continuum emission. We conservatively estimated  $\tau_{\text{frag}} \sim (2.5\text{--}3.2) \times 10^4$  yr. Note that we estimated the minimum timescale of  $2.5 \times 10^4$  yr using six sources (FraSCO-28, -32, -35, -37, -39, and -40), which are all gravitationally bound. A maximum timescale of  $3.2 \times 10^4$  yr was estimated using 18 sources (FraSCO-23 to -40), which include both gravitationally bound and unbound sources. Note the latter timescale is longer despite the additional leaves within the same clump volume because the average leaf volume is much smaller (the mean radius of FraSCO sources is approximately 2.7 times smaller). The dynamical timescale for flow-3 ( $\tau_{\text{dyn}}$ ) was also estimated to be in the range of  $\sim(0.46\text{--}2.54) \times 10^4$  yr from the CO( $J=2\text{--}1$ ) emissions discussed in Section 3.2.1.  $\tau_{\text{frag}}$  and  $\tau_{\text{dyn}}$  estimated from our observations are roughly consistent with the timescales previously estimated by Shimajiri et al. (2008); however, the errors of our estimated timescales are so large that it is difficult to determine whether  $\tau_{\text{frag}}$  is similar to  $\tau_{\text{dyn}}$  with our data. Furthermore, the dynamical timescale for outflow driven within the FIR 4 region was estimated to be in the range of  $\sim(0.2\text{--}1.7) \times 10^4$  yr, which is similar to that for outflow driven within the FIR 3 region,  $\sim(0.4\text{--}2.5) \times 10^4$  yr.

In summary, fragmentation within the FIR 4 region is considered to have started when flow-3 started interacting with the FIR 4 region or before this interaction. This conclusion does not strongly support the triggered star formation scenario proposed by Shimajiri et al. (2008).

Finally, we should note that the timescale discussion described above using the outflow dynamical timescale may be limited by the current mass ejection event. Previous studies suggest a possibility of episodic mass ejection in the protostellar phase (e.g., Plunkett et al. 2015; Zhang et al. 2019). Indeed, HOPS-370 is identified as a Class I source, having the stellar age of  $\sim 10^5$  yr. In comparison, the timescale for readsorption of evaporated SiO on dust grains is estimated as  $\sim 8 \times 10^3$  yr in the case of the density of  $4 \times 10^5$  cm $^{-3}$  (Mikami et al. 1992), implying previous mass ejection phenomena (if any exist) is not detectable with our SiO observations.

#### 4.3. Hub-filament System in the FIR 4 Region

In this section, we discuss the morphology of our 1.3 mm continuum image in the FIR 3, 4, and 5 regions, comparing its spatial distribution with the hub-fiber system previously identified in this region with N $_2$ H $^+$  ( $J=1\text{--}0$ ) observations (Hacar et al. 2018; Zhang et al. 2020). Note that we focus on the spatial distribution of dense material rather than the dynamics of the gas, i.e., we focus on filaments detected in the 1.3 mm continuum image. Investigating velocity structures within the hub-fiber system would be a future topic for high-angular resolution molecular observations.

Filamentary molecular clouds are considered to play a critical role in forming dense cores. Recent studies have shown

that dense cores tend to be located around a hub in hub-filament systems (e.g., Clarke et al. 2020). It has also been reported that column densities and velocity gradients increase along the filaments toward a hub (Hill et al. 2011; Kirk et al. 2013; Tanaka et al. 2013; Yuan et al. 2018; Treviño-Morales et al. 2019; Ren et al. 2021; Cao et al. 2022). This implies possible gas inflows toward the hub and enhanced star formation activity in the hub (Schneider et al. 2010).

As presented in Figure 19(a), previous N $_2$ H $^+$  ( $J=1\text{--}0$ ) observations have identified several velocity-coherent structures, i.e., fibers, in FIR 3, 4, and 5 in the OMC-2 regions (Hacar et al. 2018; Zhang et al. 2020). In particular, Zhang et al. (2020) identified three fibers intersecting at FIR 4, showing a hub-fiber system and reported that dense cores tend to be located around the hub.

Figure 19(b) shows the 1.3 mm continuum image of the FIR 3, 4, and 5 regions obtained from this study. Our ALMA 12 m array 1.3 mm continuum observations showed a factor of  $\sim 3$  improvement in the spatial resolution compared with previous N $_2$ H $^+$  ( $J=1\text{--}0$ ) observations by Hacar et al. (2018) and Zhang et al. (2020). In order to identify filaments from our ALMA 12 m array 1.3 mm continuum image, we assume that filaments are elongated structures within which FraSCO sources are continuously located, and then the filaments are connected toward the peak of the FIR 4 imaged with the ACA 7 m array data. With these two criteria, we identified eight filaments (green solid and dashed lines in Figure 19(b)). Three of the filaments identified by our ALMA 12 m array 1.3 mm observations (green-dashed lines in Figure 19(b)) are approximately consistent with previously identified fibers (yellow lines in the same panel) in the N $_2$ H $^+$  ( $J=1\text{--}0$ ) emission reported by Zhang et al. (2020), whereas the other five filaments (green solid lines in the same panel) are identified for the first time in our high-angular resolution ALMA 12 m array continuum image. The newly identified filaments are located within FIR 4, where a hub was identified in the previous study by Zhang et al. (2020). The hub was also determined to be a single-peak condensation in FIR 4 with our ACA 7 m array image (gray contours in Figure 19(b)).

The newly identified filaments are estimated to have H $_2$  gas column densities in the range of  $(1\text{--}17) \times 10^{23}$  cm $^{-2}$ <sup>12</sup>. These values are denser by one order of magnitude than those measured by Hacar et al. (2018) and denser by a factor of 2 than those measured by Zhang et al. (2020). Hence, the filaments identified from our ALMA 12 m array 1.3 mm continuum image are considered to trace inner dense parts compared with the previously identified N $_2$ H $^+$  ( $J=1\text{--}0$ ) fibers. The locations of newly identified filaments with higher density indirectly support a scenario of gas inflow motion to accumulate material onto the hub, as previously reported for other protocluster regions (e.g., Hill et al. 2011; Kirk et al. 2013; Treviño-Morales et al. 2019).

More interestingly, the ALMA 12 m array continuum image denoted by blue contours in Figure 19(c) does not exhibit a single-peak structure within the hub, as the lower resolution ACA 7 m array continuum image shows (gray contours in Figure 19(c)), but rather exhibits the highly complex substructures within. A Jeans analysis suggested that a central extended substructure within the hub was gravitationally bound, whereas no star formation activity such as outflows or

<sup>12</sup> In order to estimate the average column density of each filament, we fitted the elongated filaments using the 2D Gaussian.

disks was clearly detected within the central substructure. The results signify that the central substructure within the hub was possibly present in the prestellar phase and may be deemed as transient. We should note that the feedback of outflows driven within the FIR 4 region could also affect the star formation within the FIR 4 region. We detected six outflows driven by FraSCO sources located within FIR 4 region: flow-4–flow-9 identified in Section 3.2.1. These outflows could mix the surrounding material within the FIR 4 region and affect the star formation there.

To test a scenario of massive core formation through the OMC-2 hub-filament system, the gas inflow motion along the filaments should be determined. This dynamical information will enable us to constrain how much material can be accumulated onto the hub by estimating the gas inflow rates, and will eventually determine the final mass of the forming stars.

## 5. Summary

To reveal the star-forming environment in one of the nearest embedded protoclusters, FIR 3, 4, and 5 in the OMC-2 region, we obtained observations of the 1.3 mm continuum, CO( $J = 2-1$ ) line, and SiO( $J = 5-4$ ) line emissions with ALMA. The main results and conclusions are summarized as follows.

1. Using the 1.3 mm continuum image obtained with the ALMA 12 m array, we identified 51 dense sources. Among them, 36 sources were newly identified in this study. The dust masses and projected sizes of all the 51 sources are in the ranges of  $3.8 \times 10^{-5}$ – $1.1 \times 10^{-2} M_{\odot}$  and 28–1964 au, respectively. Their  $H_2$  gas number densities are estimated to be  $6.4 \times 10^6$ – $3.3 \times 10^8 \text{ cm}^{-3}$ . Most of the previously identified 15 sources (~80%) have number densities above the critical Jeans number density regardless of whether they are pre- or protostellar sources, whereas the remaining sources, consisting of three protostellar sources, have number densities below the critical density. Among the newly identified sources, ~14% have a number density above the critical Jeans number density.
2. Using the CO( $J = 2-1$ ) line image with the ALMA 12 m array, we identified six clear, five probable, and one marginal outflow in total. In addition, seven of the identified outflows have associated SiO emission. This study newly identified six CO outflows consisting of two clear, three probable, and one marginal outflows. These are associated with newly identified 1.3 mm continuum sources in the FIR 4 region. In addition to the molecular outflow, we detected 11 extended and compact SiO emissions that do not originate from molecular outflows. The SiO emissions are mainly distributed in the FIR 4 region and along lobes of an energetic outflow driven by HOPS-370.
3. We discussed three previously proposed scenarios to explain the origin of the protocluster in the FIR 4 region: (1) outflow interaction, (2) internal heating source, and (3) irradiation by an FUV field. High-angular resolution and high sensitivity observations of CO( $J = 2-1$ ) and SiO( $J = 5-4$ ) provided spatially resolved images showing direct evidence of an interaction between the dust condensation, FIR 4, and an outflow (flow-3) driven

from HOPS-370. Our observational results support the first scenario above, while no evidence was found to support the second and third scenarios.

4. Based on the outflow interaction scenario described above, we discussed fragmentation of FraSCO sources within the FIR 4 region by comparing the fragmentation timescale for the FraSCO sources with the dynamical timescale for flow-3. The fragmentation timescale was estimated to be  $\sim(2.5-3.2) \times 10^4 \text{ yr}$ , which is similar to the dynamical timescale for flow-3,  $\sim(0.46-2.54) \times 10^4 \text{ yr}$ . Furthermore, the dynamical timescale for the outflow driven within the FIR 4 region is estimated to be in the range of  $\sim(0.2-1.7) \times 10^4 \text{ yr}$ , which is similar to the dynamical timescale for the outflow driven within the FIR 3 region,  $\sim(0.4-2.5) \times 10^4 \text{ yr}$ . Therefore, fragmentation within the FIR 4 region is considered to have started when flow-3 started interacting with the FIR 4 region or before that interaction. This conclusion does not strongly support the triggered star formation scenario previously proposed by Shimajiri et al. (2008).
5. Finally, using the 1.3 mm continuum images with the ALMA 12 m array and the ACA 7 m array, we discussed the morphology of the hub-filament system located within the FIR 3, 4, and 5 regions. We identified eight filaments intersecting at the central hub, i.e., the center of FIR 4. Five of them were newly identified in this study and located within the FIR 4 region. The  $H_2$  gas column densities of the filaments were estimated to be  $(1-17) \times 10^{23} \text{ cm}^{-2}$ , which is denser than those of the previously identified  $N_2H^+$  fibers. Interestingly, the ALMA 12 m array continuum image exhibits highly complex substructures within the hub. Based on the result that the central substructure within the hub is gravitationally bound with no star formation activity, the central substructure was possibly present in the prestellar phase and may be deemed as transient. To test a scenario of massive core formation through the OMC-2 hub-filament system, the gas inflow motion along the filaments should be determined. However, our observations have no velocity information about the detected hub-filament system, and hence investigation of the dynamical motion will be a topic for future study.

We deeply acknowledge the referee for the very careful reading and constructive comments that have helped improve this manuscript. We thank D. Johnstone for providing us with the submillimeter continuum data taken by JCMT. We thank Y. Aso for helping us with creating the animations presented in this paper. This paper makes use of the following ALMA data: ADS/JAO.ALMA#2017.1.01353.S. ALMA is a partnership of ESO (representing its member states), NSF (USA) and NINS (Japan), together with NRC (Canada), MOST and ASIAA (Taiwan), and KASI (Republic of Korea), in cooperation with the Republic of Chile. The Joint ALMA Observatory is operated by ESO, AUI/NRAO, and NAOJ. This work was supported by NAOJ ALMA Scientific Research grant No. 2022-22B. The present study was supported by JSPS KAKENHI grants (JP17H06360, JP17K05387, JP17KK0096, JP21H00046, JP21K03617: MNM, 20K04034: SI). L.A.Z. acknowledges financial support from CONACyT-280775 and UNAM-PAPIIT IN110618 grants, México. This project has received funding from the European Research Council (ERC)



under the European Union’s Horizon 2020 research and innovation program (grant agreement No. 851435).

## Appendix A

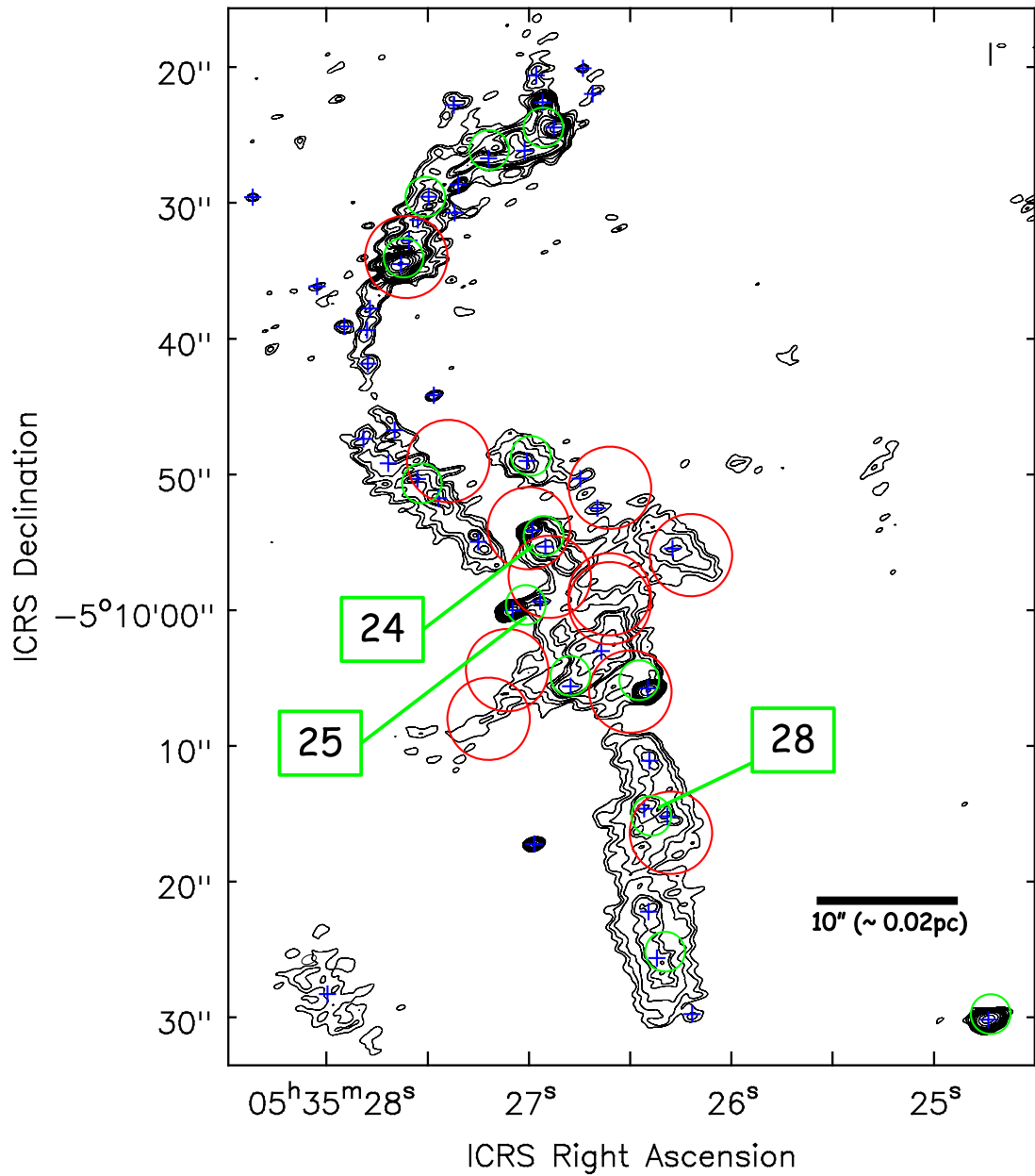
### Comparisons of Images with Previous Observations

In Table 6 of Section 3.1.1, we compared the positions of FraSCO sources with those of previously identified sources located within the synthesized beam size for our 1.3 mm continuum image obtained from the ALMA 12 m array ( $\sim 1''$ ) from the positions of FraSCO sources. However, some of the millimeter sources identified by Shimajiri et al. (2008) and Kainulainen et al. (2017) are not associated with individual FraSCO sources due to differences in the angular resolutions and observational frequencies. These spatial associations made it difficult to list their source positions in Table 6. Therefore, in this section, we plot their positions over our 1.3 mm continuum image obtained from the ALMA 12 m array in Figure 20 to spatially compare them with FraSCO sources.

Shimajiri et al. (2008) carried out 3.3 mm observations toward the FIR 3 and FIR 4 regions using the Nobeyama

Millimeter Array (NMA) with an angular resolution of  $\sim 6''$  and rms noise level of  $1.4 \text{ mJy beam}^{-1}$ . In Figure 20, we compared the positions of the sources identified in our 1.3 mm ALMA observations and the 3.3 mm NMA observations. Although beam sizes are very different between the two observations, we found that a few FraSCO sources are located within most of the 3.3 mm continuum sources, denoted by the red open circles in Figure 20. Positional inconsistency between FraSCO sources and the 3.3 mm continuum sources could be explained by the sources identified with lower angular resolution breaking up into multiple components at higher resolution.

Kainulainen et al. (2017) carried out 3 mm continuum observations toward the OMC-2/3 region using the ALMA 12 m array and the ACA 7 m array data. They combined these two data and obtained images with an angular resolution of  $\sim 3''$  and rms noise level of  $0.23 \text{ mJy beam}^{-1}$ . As shown in Figure 20, the position of most 3 mm continuum sources is located within  $\sim 1''$  from the position of the FraSCO sources, while three of them, named 24, 25, and 28 in Kainulainen et al. (2017), are located between the positions of two FraSCO

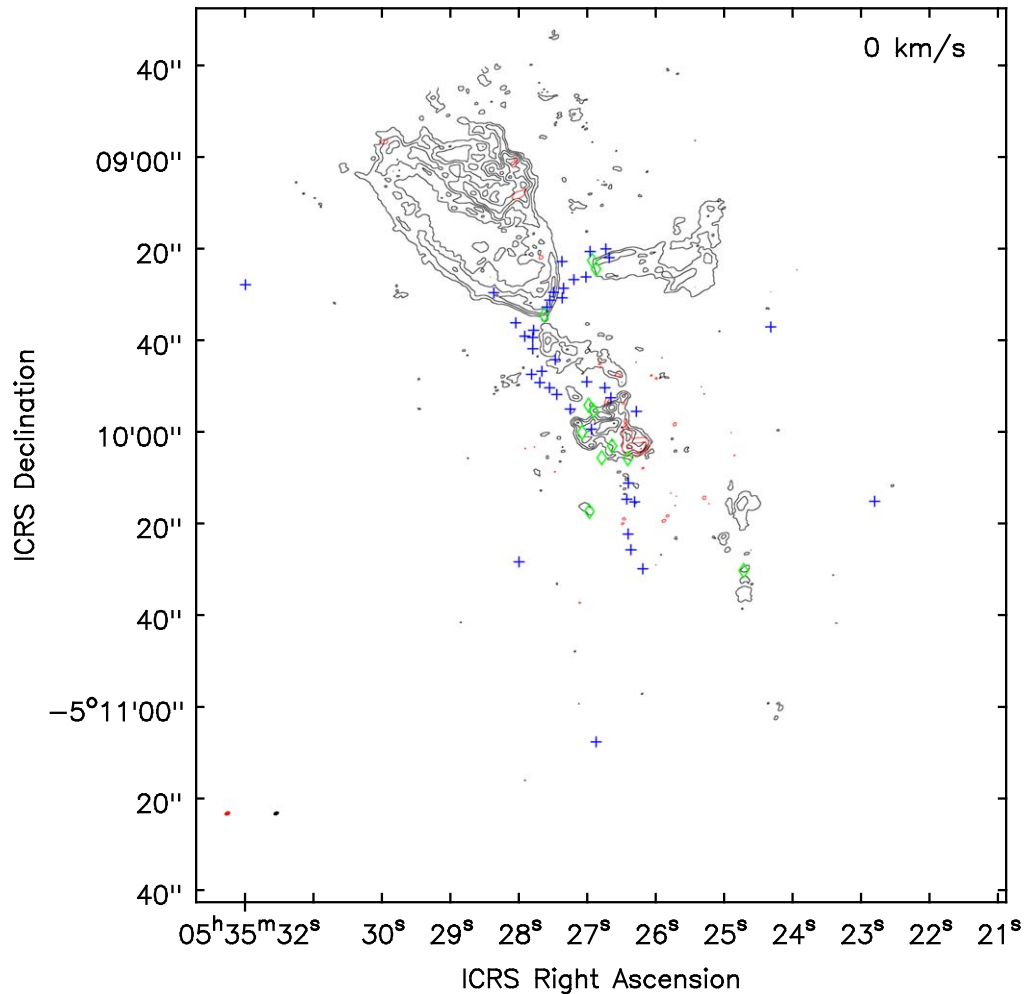


**Figure 20.** Comparison between 1.3 mm FraSCO sources and previously identified millimeter dense cores. The black contours and blue crosses represent our 1.3 mm continuum images obtained from the ALMA 12 m array and the positions of FraSCO sources, respectively. The red open circles and green open circles show the positions of 3.3 mm dense cores identified by Shimajiri et al. (2008) and 3 mm dense cores identified by Kainulainen et al. (2017). The size of the red and green circles corresponds to the angular resolution of each observation, 6'' and 3'', respectively. The black contour levels are [5, 7, 10, 15, 17, 20, 25, 32, 40, 60, 100, 170, 300, 700]  $\times 1\sigma$  ( $1\sigma = 0.22 \text{ mJy beam}^{-1}$ ). FraSCO-16 and FraSCO-32 are the names of the FraSCO sources identified in this study. 24, 25, and 28 are the names of the 3 mm sources identified by Kainulainen et al. (2017).

sources. This positional inconsistency could also explain that the three sources with lower angular resolution break up into two components at higher resolution, as mentioned above when we compared the results with Shimajiri et al. (2008).

### Appendix B CO( $J = 2-1$ ) and SiO( $J = 5-4$ ) Channel Maps

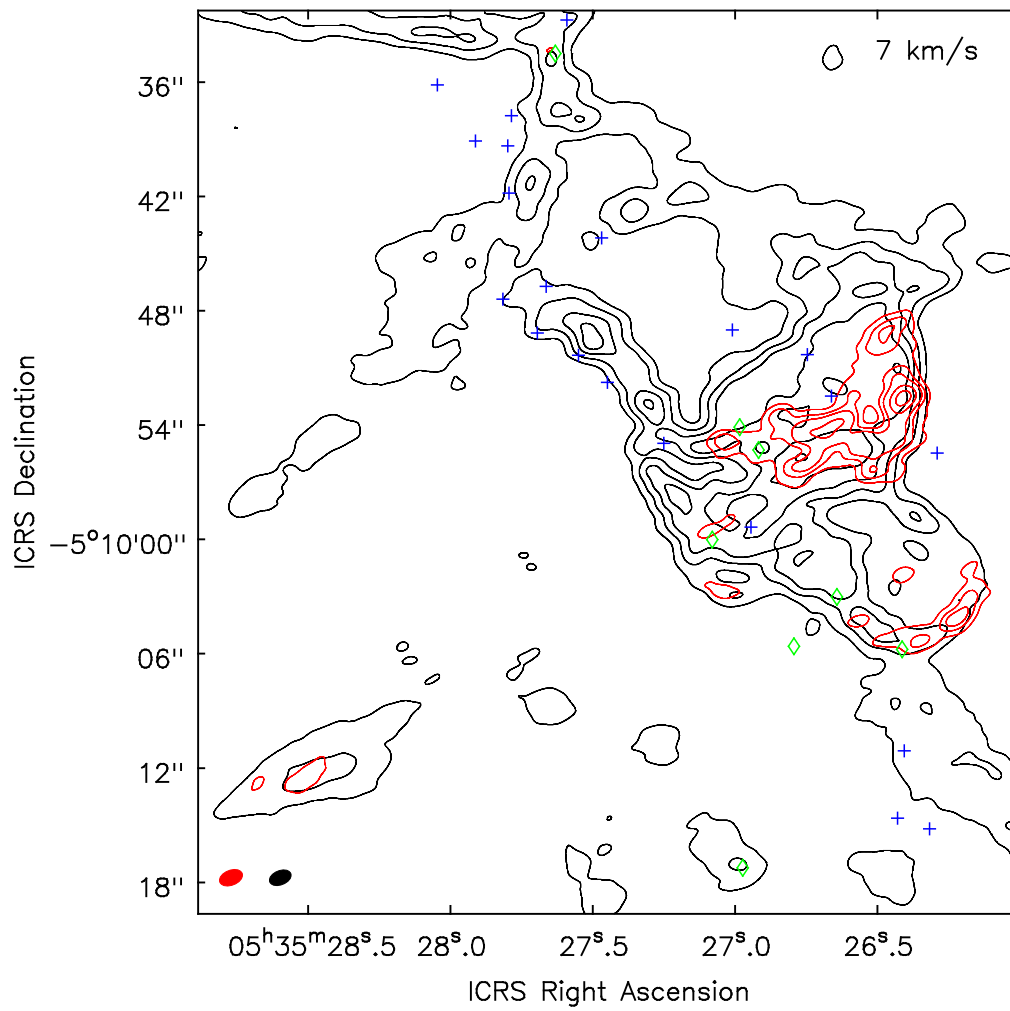
In order to present detailed spatial distributions for CO( $J = 2-1$ ) and SiO( $J = 5-4$ ) emissions, we show channel maps for both line emissions in this section. Figure 21 shows



**Figure 21.** Channel map at  $v_{\text{LSR}} = 0 \text{ km s}^{-1}$  for both the CO( $J = 2-1$ ) and SiO( $J = 5-4$ ) line emissions obtained from the ALMA 12 m array with the velocity resolution of  $5 \text{ km s}^{-1}$  denoted by the black and red contours, respectively. The black contour levels are  $[4, 20, 50, 100, 180, 250] \times 1\sigma$  ( $1\sigma = 5.3 \text{ mJy beam}^{-1}$ ). The red contour levels are  $[5, 30, 70] \times 1\sigma$  ( $1\sigma = 4.8 \text{ mJy beam}^{-1}$ ). The symbols show the positions of the FraSCO sources: the green diamonds and blue crosses represent outflow driving sources and sources without outflow, respectively. The black and red ellipses at the bottom-left corner show the synthesized beam size of the CO and SiO images, respectively. The complete figure set, including other channel maps (33 images), is available in the online journal.

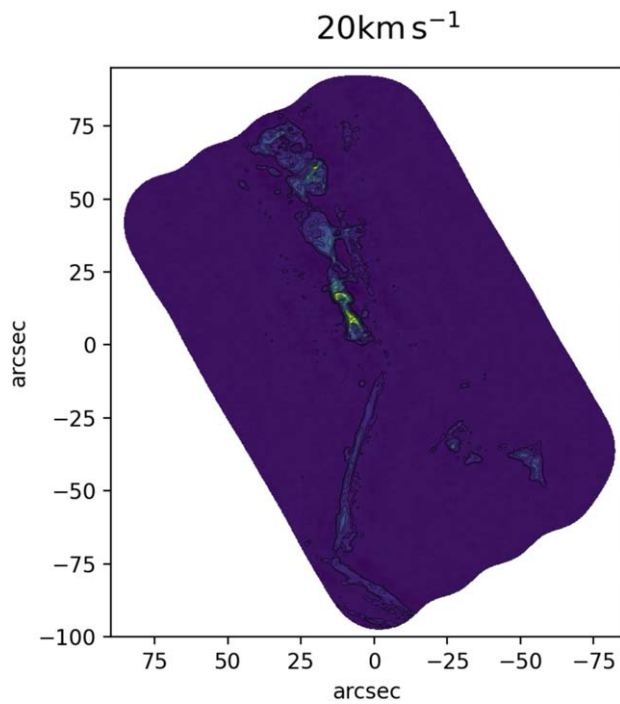
(The complete figure set (33 images) is available.)





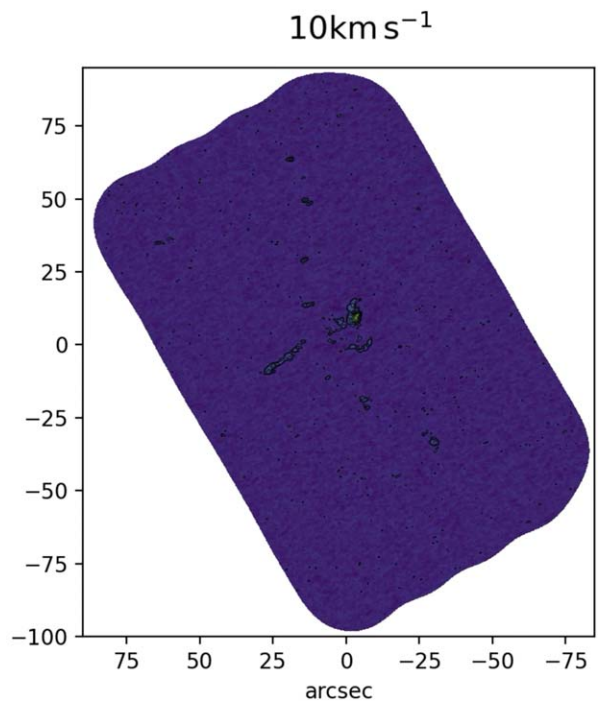
**Figure 22.** Channel map zoomed in on the FIR 4 region at  $v_{\text{LSR}} = 7 \text{ km s}^{-1}$  for the  $\text{CO}(J = 2-1)$  and  $\text{SiO}(J = 5-4)$  line emissions obtained from the ALMA 12 m array with the velocity resolution of  $1 \text{ km s}^{-1}$  denoted by the black and red contours, respectively. The black contour levels are  $[10, 50, 100, 150, 200, 250] \times 1\sigma$  ( $1\sigma = 10 \text{ mJy beam}^{-1}$ ). The red contour levels are  $[5, 10, 15, 25, 35, 45] \times 1\sigma$  ( $1\sigma = 9.0 \text{ mJy beam}^{-1}$ ). The symbols show the positions of the FraSCO sources: the green diamonds and blue crosses represent outflow driving sources and sources without outflow, respectively. The black and red ellipses at the bottom-left corner denote the synthesized beam size of the CO and SiO images, respectively. The complete figure set, including other channel maps (47 images), is available in the online journal.

(The complete figure set (47 images) is available.)



**Figure 23.** Channel map at  $v_{\text{LSR}} = 20 \text{ km s}^{-1}$  for the CO( $J = 2-1$ ) line emission obtained from the ALMA 12 m array with the velocity resolution of  $5 \text{ km s}^{-1}$  denoted by the color scale and black contours. The black contour levels are  $[5, 10, 30, 50, 100, 150, 200, 250] \times 1\sigma$  ( $1\sigma = 5.3 \text{ mJy beam}^{-1}$ ). An animation of this figure is available in the online journal. The animation of the channel map images runs from  $v_{\text{LSR}} = -100$  to  $+95 \text{ km s}^{-1}$  for the CO( $J = 2-1$ ) line emission.

(An animation of this figure is available.)


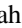





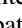
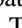


**Figure 24.** Channel map at  $v_{\text{LSR}} = 10 \text{ km s}^{-1}$  for the SiO( $J = 5-4$ ) line emission obtained from the ALMA 12 m array with the velocity resolution of  $1 \text{ km s}^{-1}$  denoted by the color scale and black contours. The black contour levels are  $[3, 5, 10, 15, 25, 35, 45] \times 1\sigma$  ( $1\sigma = 9.0 \text{ mJy beam}^{-1}$ ). An animation of this figure is available in the online journal. The animation of the channel map images runs from  $v_{\text{LSR}} = -30$  to  $+29 \text{ km s}^{-1}$  for the SiO( $J = 5-4$ ) line emission.

(An animation of this figure is available.)

an example channel map at  $v_{\text{LSR}} \sim 0 \text{ km s}^{-1}$  with the velocity resolution of  $5 \text{ km s}^{-1}$  for the CO and SiO line emissions. The complete figure set, Figure Set 1, including other channel maps (47 images), is available in the online journal. Figure 22 shows an example channel map at  $v_{\text{LSR}} = 7 \text{ km s}^{-1}$  zooming in on the FIR 4 region with the velocity resolution of  $1 \text{ km s}^{-1}$  for the CO and SiO line emissions. The complete figure set, Figure Set 2, including other channel maps (24 images), is available in the online journal. Figure 23 shows a channel map with the velocity resolution of  $5 \text{ km s}^{-1}$  for the CO line emission as a part of an animation. Figure 24 also shows a channel map with the velocity resolution of  $1 \text{ km s}^{-1}$  for the SiO line emission as a part of an animation. The animations of these figures are available in the online journal.

### ORCID iDs

Asako Sato  <https://orcid.org/0000-0001-5817-6250>  
 Satoko Takahashi  <https://orcid.org/0000-0002-7287-4343>  
 Shun Ishii  <https://orcid.org/0000-0001-8337-4961>  
 Paul T. P. Ho  <https://orcid.org/0000-0002-3412-4306>  
 Masahiro N. Machida  <https://orcid.org/0000-0002-0963-0872>  
 John Carpenter  <https://orcid.org/0000-0003-2251-0602>  
 Luis A. Zapata  <https://orcid.org/0000-0003-2343-7937>  
 Paula Stella Teixeira  <https://orcid.org/0000-0002-3665-5784>  
 Sümeyye Suri  <https://orcid.org/0000-0003-0412-8522>

### References

- Allen, L., Megeath, S. T., Gutermuth, R., et al. 2007, in *Protostars and Planets V*, ed. B. Reipurth, D. Jewitt, & K. Keil (Tucson, AZ: Univ. Arizona Press), 361
- André, P., Di Francesco, J., Ward-Thompson, D., et al. 2014, in *Protostars and Planets VI*, ed. H. Beuther et al. (Tucson, AZ: Univ. Arizona Press), 27
- Anglada, G., Villuendas, E., Estalella, R., et al. 1998, *AJ*, 116, 2953
- Arce, H. G., Shepherd, D., Gueth, F., et al. 2007, in *Protostars and Planets V*, ed. B. Reipurth, D. Jewitt, & K. Keil (Tucson, AZ: Univ. Arizona Press), 245
- Aso, Y., Tatematsu, K., Sekimoto, Y., et al. 2000, *ApJS*, 131, 465
- Bachiller, R. 1996, *ARA&A*, 34, 111
- Bally, J., Stark, A. A., Wilson, R. W., & Langer, W. D. 1987, *ApJL*, 312, L45
- Bonnell, I. A., Bate, M. R., Clarke, C. J., & Pringle, J. E. 2001, *MNRAS*, 323, 785
- Bontemps, S., André, P., Terebey, S., & Cabrit, S. 1996, *A&A*, 311, 858
- Buckle, J. V., Davis, C. J., Francesco, J. D., et al. 2012, *MNRAS*, 422, 521
- Cao, Y., Qiu, K., Zhang, Q., & Li, G. 2022, *ApJ*, 927, 106
- CASA Team, Bean, Ben, Bhatnagar, Sanjay, et al. 2022, *PASP*, 134, 114501
- Caselli, P., Hartquist, T. W., & Havnes, O. 1997, *A&A*, 322, 296
- Cheng, Y., Tan, J. C., Liu, M., et al. 2018, *ApJ*, 853, 160
- Chini, R., Reipurth, B., Ward-Thompson, D., et al. 1997, *ApJL*, 474, L135
- Clarke, S. D., Williams, G. M., & Walch, S. 2020, *MNRAS*, 497, 4390
- Crimier, N., Ceccarelli, C., Lefloch, B., & Faure, A. 2009, *A&A*, 506, 1229
- Davis, C. J., Gell, R., Khanzadyan, T., Smith, M. D., & Jenness, T. 2010, *A&A*, 511, A24
- Evans, L., Fontani, F., Vastel, C., et al. 2022, *A&A*, 657, A136
- Evans, N. J. I 1999, *ARA&A*, 37, 311
- Favre, C., Ceccarelli, C., López-Sepulcre, A., et al. 2018, *ApJ*, 859, 136
- Fedderson, J. R., Arce, H. G., Kong, S., et al. 2020, *ApJ*, 896, 11
- Fontani, F., Ceccarelli, C., Favre, C., et al. 2017, *A&A*, 605, A57
- Furlan, E., Fischer, W. J., Ali, B., et al. 2016, *ApJS*, 224, 5
- González-García, B., Manoj, P., Watson, D. M., et al. 2016, *A&A*, 596, A26

- Goodman, A. A., Rosolowsky, E. W., Borkin, M. A., et al. 2009, *Natur*, **457**, 63
- Großschedl, J. E., Alves, J., Meingast, S., et al. 2018, *A&A*, **619**, A106
- Gueth, F., Guilloteau, S., & Bachiller, R. 1998, *A&A*, **333**, 287
- Habel, Nolan M., Thomas Megeath, S., Jon Booker, Joseph, et al. 2021, *ApJ*, **911**, 153
- Hacar, A., Tafalla, M., Forbrich, J., et al. 2018, *A&A*, **610**, A77
- Hacar, A., Tafalla, M., Kauffmann, J., & Kovács, A. 2013, *A&A*, **554**, A55
- Hansen, C. E., Klein, R. I., McKee, C. F., & Fisher, R. T. 2012, *ApJ*, **747**, 22
- Hayashi, C. 1981, *PThPS*, **70**, 35
- Hill, T., Motte, F., Didelon, P., et al. 2011, *A&A*, **533**, A94
- Hirano, N., Ho, P. T. P., Liu, S., et al. 2010, *ApJ*, **717**, 58
- Ikeda, N., Sunada, K., & Kitamura, Y. 2007, *ApJ*, **665**, 1194
- Ishii, S., Nakamura, F., Shimajiri, Y., et al. 2019, *PASJ*, **71**, S9
- Jeans, J. H. 1902, *RSPTA*, **199**, 1
- Johnstone, D., & Bally, J. 1999, *ApJL*, **510**, L49
- Kainulainen, J., Stutz, A. M., Stanke, T., et al. 2017, *A&A*, **600**, A141
- Kang, M., Choi, M., Wyrowski, F., et al. 2021, *ApJS*, **255**, 2
- Kirk, H., Friesen, R. K., Pineda, J. E., et al. 2017, *ApJ*, **846**, 144
- Kirk, H., Myers, P. C., Bourke, T. L., et al. 2013, *ApJ*, **766**, 115
- Kong, S., Arce, H. G., Feddersen, J. R., et al. 2018, *ApJS*, **236**, 25
- Krumholz, M. R., Klein, R. I., & McKee, C. F. 2012, *ApJ*, **754**, 71
- Lada, C. J., & Lada, E. A. 2003, *ARA&A*, **41**, 57
- Lada, C. J., Muench, A. A., Rathborne, J., Alves, J. F., & Lombardi, M. 2008, *ApJ*, **672**, 410
- Li, D., Kauffmann, J., Zhang, Q., & Chen, W. 2013, *ApJL*, **768**, L5
- Lis, D. C., Serabyn, E., Keene, J., et al. 1998, *ApJ*, **509**, 299
- Liu, M., Tan, J. C., Marvil, J., et al. 2021, *ApJ*, **921**, 96
- López-Sepulcre, A., Taquet, V., Sánchez-Monge, Á., et al. 2013, *A&A*, **556**, A62
- Machida, M. N., Inutsuka, S.-i., & Matsumoto, T. 2007, *ApJ*, **670**, 1198
- Machida, M. N., Inutsuka, S.-i., & Matsumoto, T. 2008, *ApJ*, **676**, 1088
- Maddalena, R. J., & Thaddeus, P. 1985, *ApJ*, **294**, 231
- Mason, B., Dicker, S., Sadavoy, S., et al. 2020, *ApJ*, **893**, 13
- Matsushita, Y., Takahashi, S., Ishii, S., et al. 2021, *ApJ*, **916**, 23
- Matsushita, Y., Takahashi, S., Machida, M. N., & Tomisaka, K. 2019, *ApJ*, **871**, 221
- McKee, C. F., & Tan, J. C. 2003, *ApJ*, **585**, 850
- McLaughlin, D. E., & Pudritz, R. E. 1996, *ApJ*, **469**, 194
- Megeath, S. T., Gutermuth, R., Muzerolle, J., et al. 2012, *AJ*, **144**, 192
- Mikami, H., Umemoto, T., Yamamoto, S., & Saito, S. 1992, *ApJL*, **392**, L87
- Motte, F., Zavagno, A., Bontemps, S., et al. 2010, *A&A*, **518**, L77
- Myers, P. C. 2009, *ApJ*, **700**, 1609
- Nagahama, T., Mizuno, A., Ogawa, H., & Fukui, Y. 1998, *AJ*, **116**, 336
- Nakamura, F., & Li, Z. 2011, *ApJ*, **740**, 36
- Nakamura, F., Oyamada, S., Okumura, S., et al. 2019, *PASJ*, **71**, S10
- Nielbock, M., Chini, R., & Müller, S. A. H. 2003, *A&A*, **408**, 245
- Nutter, D., & Ward-Thompson, D. 2007, *MNRAS*, **374**, 1413
- O'Dell, C. R., Muench, A., Smith, N., & Zapata, L. 2008, in *Handbook of Star Forming Regions, Volume I: The Northern Sky*, ASP Monograph Publications, Vol. 4., ed. B. Reipurth (San Francisco, CA: ASP), **544**
- Offner, S. S. R., & Chaban, J. 2017, *ApJ*, **847**, 104
- Ohashi, S., Sanhueza, P., Chen, H. V., et al. 2016, *ApJ*, **833**, 209
- Osorio, M., Díaz-Rodríguez, A. K., Anglada, G., et al. 2017, *ApJ*, **840**, 36
- Ossenkopf, V., & Henning, T. 1994, *A&A*, **291**, 943
- Palla, F., & Stahler, S. W. 1993, *ApJ*, **418**, 414
- Pattle, K., Ward-Thompson, D., Kirk, J. M., et al. 2015, *MNRAS*, **450**, 1094
- Pecaut, M. J., & Mamajek, E. E. 2013, *ApJS*, **208**, 9
- Plunkett, A. L., Arce, H. G., Mardones, D., et al. 2015, *Natur*, **527**, 70
- Reipurth, B., Rodríguez, L. F., & Chini, R. 1999, *AJ*, **118**, 983
- Ren, Z., Zhu, L., Shi, H., et al. 2021, *MNRAS*, **505**, 5183
- Rosolowsky, E. W., Pineda, J. E., Kauffmann, J., & Goodman, A. A. 2008, *ApJ*, **679**, 1338
- Sadavoy, S. I., Stutz, A. M., Schnee, S., et al. 2016, *A&A*, **588**, A30
- Sakamoto, S., Hayashi, M., Hasegawa, T., Handa, T., & Oka, T. 1994, *ApJ*, **425**, 641
- Sanhueza, P., Contreras, Y., Wu, B., et al. 2019, *ApJ*, **886**, 102
- Schneider, N., Csengeri, T., Bontemps, S., et al. 2010, *A&A*, **520**, A49
- Schneider, S., & Elmegreen, B. G. 1979, *ApJS*, **41**, 87
- Shimajiri, Y., Takahashi, S., Takakuwa, S., Saito, M., & Kawabe, R. 2008, *ApJ*, **683**, 255
- Smith, R. J., Glover, S. C. O., Bonnell, I. A., Clark, P. C., & Klessen, R. S. 2011, *MNRAS*, **411**, 1354
- Snell, R. L., Loren, R. B., & Plambeck, R. L. 1980, *ApJL*, **239**, L17
- Stanke, T., McCaughrean, M. J., & Zinnecker, H. 2002, *A&A*, **392**, 239
- Stutz, A. M., Tobin, J. J., Stanke, T., et al. 2013, *ApJ*, **767**, 36
- Takahashi, S., Ho, P. T. P., Teixeira, P. S., Zapata, L. A., & Su, Y. 2013, *ApJ*, **763**, 57
- Takahashi, S., Saito, M., Ohashi, N., et al. 2008, *ApJ*, **688**, 344
- Tanabe, Y., Nakamura, F., Tsukagoshi, T., et al. 2019, *PASJ*, **71**, S8
- Tanaka, T., Nakamura, F., Awazu, Y., et al. 2013, *ApJ*, **778**, 34
- Tatematsu, K., Ohashi, S., Sanhueza, P., et al. 2016, *PASJ*, **68**, 24
- Tatematsu, K., Umemoto, T., Kameya, O., et al. 1993, *ApJ*, **404**, 643
- Teixeira, P. S., Takahashi, S., Zapata, L. A., & Ho, P. T. P. 2016, *A&A*, **587**, A47
- Tobin, J. J., Megeath, S. T., van't Hoff, M. v., et al. 2019, *ApJ*, **886**, 6
- Tobin, J. J., Sheehan, P. D., Reynolds, N., et al. 2020, *ApJ*, **905**, 162
- Treviño-Morales, S. P., Fuente, A., Sánchez-Monge, Á., et al. 2019, *A&A*, **629**, A81
- van Terwisga, S. E., Hacar, A., & van Dishoeck, E. F. 2019, *A&A*, **628**, A85
- Wang, P., Li, Z., Abel, T., & Nakamura, F. 2010, *ApJ*, **709**, 27
- Williams, J. P., Plambeck, R. L., & Heyer, M. H. 2003, *ApJ*, **591**, 1025
- Wilson, B. A., Dame, T. M., Mashed, M. R. W., & Thaddeus, P. 2005, *A&A*, **430**, 523
- Yu, K. C., Bally, J., & Devine, D. 1997, *ApJL*, **485**, L45
- Yuan, J., Li, J., Wu, Y., et al. 2018, *ApJ*, **852**, 12
- Zapata, L. A., Ho, P. T. P., Rodríguez, L. F., et al. 2006, *ApJ*, **653**, 398
- Zhang, C., Ren, Z., Wu, J., et al. 2020, *MNRAS*, **497**, 793
- Zhang, Q., Hunter, T. R., Sridharan, T. K., & Ho, P. T. P. 2002, *ApJ*, **566**, 982
- Zhang, Y., Arce, H. G., Mardones, D., et al. 2019, *ApJ*, **883**, 1
- Ziurys, L. M., Snell, R. L., & Dickman, R. L. 1989, *ApJ*, **341**, 857